Chapter 11

INSTRUMENTATION*

11.1 Background of the measurement technique development

Accelerator-driven systems (ADS) using lead (Pb) or eutectic lead-bismuth (PbBi) alloys require measurement technologies especially adapted to them. Besides their relatively high density, corrosivity, opaqueness, weak specific electric and thermal conductivity the sensors being in contact with the liquid are facing elevated temperatures in the range from 200°C to 550°C or even more. Although in the past decades a lot of progress has been achieved in developing liquid metal adapted measurement devices in the context of sodium operated fast breeder reactors only part of the knowledge can be transferred to lead or lead alloy cooled systems because of its specific properties.

While using measurement devices one must clearly distinguish between operational and maintenance purposes and scientific ones. A list of topics for the different requirement profiles are given in Table 11.1.1.

Table 11.1.1. Requirement profiles of measurement technologies for reactor and scientific purposes

Maintenance and operation	Scientific use
Reliable component and reactor operation	High spatial and temporal resolution
Safe system monitoring	Negligible impact on desired measurement effect
Sufficiently fast response time to abnormal conditions (shutdown)	Applicability in the specific environment (temperature, pressure magnetic fields, etc.)
Long life time	Repeatability and accuracy
Simple replacement	Calibration effort
Absolute value (no calibration required)	
Reasonable price and accuracy	

Fluid mechanical measurement devices are in principle divided into two classes of systems. One is the measurement of global quantities, which are mostly scalars like the flow rate, the pressure in the system or the mean temperatures. This class of devices is dedicated to reactor applications and the use in liquid metal loop operation. The other class is formed by measurement of local quantities like the velocity and void distribution, the heat flux, the surface structure and shape, which is necessary to capture effects occurring in generic scientific problems. The detection of these particular effects in benchmark problems allows the development of new physical models or the validation computational fluid dynamic (CFD) simulations. Naturally, the border between the two classes is not sharply defined. For instance by miniaturisation of pressure measurement devices Pitot or Prandtl tube can be developed able to detect smallest velocities.

* *Chapter lead: Robert Stieglitz (FZK, Germany). The author would like to thank colleagues from the Karlsruhe Lead Laboratory (KALLA), the NUKLEAR programme at the Karlsruhe research centre, and many other unnamed persons for supplying information on this compression.*

Of course, this handbook can not cover the whole branch of measurement devices currently available or being under development. In this context we limit ourselves on the presentation of pressure and flow rate measurement devices, discuss some temperature measurement technologies and typical mistakes often made as well methodologies to measure local velocity and void fraction distributions, surface structures and liquid level detection techniques. For the individual devices the physical operation principles are explained, and often an example for the application in heavy liquid metals is described as well as an appropriate literature source is cited. As far as known to the authors the advantages and disadvantages are mentioned and discussed.

This chapter discusses instruments commonly used to measure process variables, with emphasis on instrument problems and on the types of instruments, primarily the sensors, peculiar to liquid metal applications. Some techniques established in the broader field of process-variable measurement and in other areas of instrumentation may be applicable, but because of the limited usage or apparent suitability in liquid metals, they are not discussed here. Since the instrumentation technology for lead and its alloys is still in its infancies often examples for the application of specific techniques in other heavy liquid metals described which offer a potential transferability to lead and its systems. Among the quite broad amount instrumentation literature textbooks there are only a few related to liquid metal such as [Drowden, 1972] or [Foust, 1978]. In the context of the liquid metal handbook all data are expressed in metric units using the MKS system.

11.2 Flow meters

Many physical principles can be used to determine the flow rate of fluids in pipes [Goldstein, 1983], but the physical and chemical properties of lead bismuth exclude some of them right from the start. The opaqueness, which all liquid metals have in common, disables all optical methods, not only for a quantitative but also for a qualitative access to the flow. A review of liquid metal measurement techniques applied in the casting industry gives the overview article by [Argyropoulos, 2001]. In the following sections, the physical principles of the investigated methods are described.

11.2.1 Electromagnetic flow meters

11.2.1.1 DC electromagnetic flow meters

Permanent magnet flow meters (PMF) are mostly used if the installation volume is rather small or where low flow rates have to be resolved. According to the Faraday law an electrically conducting fluid flowing perpendicular to a magnetic field induces an electric field. The strength of this electric field is proportional to the flow velocity and can be measured with diametrically opposed electrodes on the pipe walls perpendicular to flow direction and magnetic field. A compilation of the theoretical concepts concerning electromagnetic flow measurements is given by the book of [Shercliff, 1962]. From the Maxwell equations the Poisson equation for an electromagnetic flow meter can be derived:

$$\nabla^2 \phi = \nabla \cdot (u \times B) \tag{11.1}$$

with the electric potential ϕ and the vector quantities velocity u and magnetic field B. The partial differential Eq. (11.1) cannot be solved in general, but with simplified boundary conditions and with the aid of the Green function a transformation can be made and a solution can be given for a finite region of a flow meter with point electrodes. For the voltage at the electrodes, derived from the electric potential difference $\Delta\phi$, one obtains with a weighting vector W, which indicates the contribution of the flow in a single volumetric element to the effective measurable voltage:

$$\Delta\phi = \int_{x,y,z} W(u \times B) dxdydz \tag{11.2}$$

For an axially symmetric flow profile and an infinite, homogenous magnetic field follows the simple dependency:

$$\Delta\phi = c \cdot u_m Bd \tag{11.3}$$

showing the proportionality between the measured electrode voltage $\Delta\phi$ and the mean flow velocity u_m depending on the mean magnetic field strength B and the pipe diameter d. The weighting vector introduced in Eq. (11.2) was evaluated by [Shercliff, 1962, 1987] for an infinite long, homogeneous magnetic flow-meter field (2-D problem).

Potential error sources of the PMF sensor and the correct installation

With the weighting distribution shown in Figure 11.2.1 the influence of an asymmetric flow profile on the measurement accuracy of an electromagnetic flow meter can be estimated. Due to higher gradients in the weighting field, the use of point electrodes should introduce higher uncertainties in magnetic flow meter systems than line electrodes. In reality this can be observed, but the deviations are always small compared to the signal amplitude, normally lower than 1% [Bonfig, 2002]. A different situation occurs, when impurities accumulate in the near vicinity of the electrodes. In this case a massive change of the signal voltage arises and destroys the linearity of the flow meter system. Hence, Eq. (11.3) no longer holds and the flow meter becomes useless.

Figure 11.2.1. Evaluation of the weighting vector function based on [Shercliff, 1962] for (a) point electrodes and (b) line electrodes

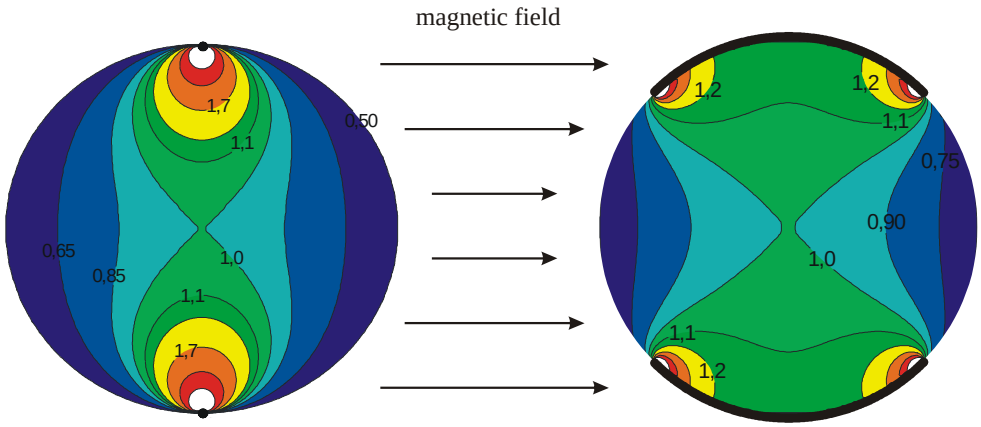

(a) point electrodes (b) line electrodes

Furthermore, the pipe walls at the electrodes and the fluid are forming a galvanic element, which produces an additional voltage depending on temperature, flow, pressure, the chemical properties of the fluid and the surface conditions of the steel walls. Consequently this voltage is different at both electrodes and contributes as a theoretically not calculable perturbation to the signal and has to be compensated by means of a calibration.

One problem is the variability of the boundary conditions while operation, which makes this calibration necessary in regular intervals. In particular, the non-definite wetting behaviour of liquid lead-bismuth to the electrically conducting structure material can lead to incorrect readings even during

one measurement day. The fluid may be wetted through the wall in the adhesive sense, so that the pressure drop in the piping shows a wetting of the surface. However, a contact resistance between the wall and the fluid may still exist. Due to this contact resistance part of the current induced in the fluid by the permanent magnetic field *B* short-circuits in the fluid and the other one in the duct walls. This effect is important since the specific electric conductivity of liquid metals σ_{LM} like lead or the eutectic alloy $Pb^{45}Bi^{55}$ is of the same order as that of the most structure materials like steel σ_{wall}, while for the use in sodium or sodium potassium most of the current is confined to the liquid, because there $\sigma_{LM}/\sigma_{wall} >> 1$.

A last issue to the use of PMF and its set-up in piping systems should be mentioned. Since large permanent magnets covering the whole ducts cross-section, in which the flow rate is measured are expensive mostly misreadings appear especially at low flow rates. If the flow is laminar in the duct and the magnetic field is penetrating only a part of the cross-section, the non-homogeneous magnetic field modifies the laminar flow profile establishing in the duct. This leads to induction of smaller electric potentials transverse to the mean magnetic field und thus to an underestimation of the flow rate. This non-linearity at low flow velocities has to be considered by means of a Reynolds number analysis and can be taken into account by inserting Venturi nozzles upstream the PMF.

If the applied magnetic field is disturbed by another steady magnetic field the magnetic field lines are bended, see Figure 11.2.2(b). As a result the flow rate measured is not correct any more. However, if a magnetic shield in form of a ferromagnetic plate (with a high magnetic permeability $\mu_r >> 1$) is placed between the flow meter and the scattering field the field lines of the scattering field are focused in the plate and hence the measurement field remains unchanged, see Figure 11.2.2(c). The thickness of the plate can be calculated using the magnetic potential equation. In general a few millimetres are enough to compensate a field of nearly one Tesla. The shown method of magnetic shielding works only for DC magnetic fields. In case of AC fields the flow meter has to be fully capsuled with ferro-magnetic materials.

Figure 11.2.2. (a) Measurement principle of a DC electromagnetic flow meter. (b) Influence of a scattering magnetic field on the magnetic field of a permanent electromagnetic flow meter. (c) Protection of the electromagnetic flow meter from a DC magnetic scattering field using a ferro-magnetic shielding.

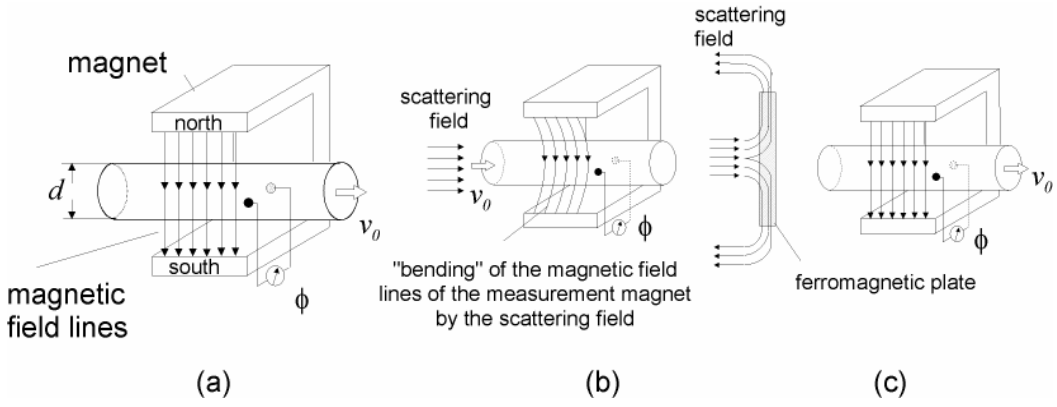

Figure 11.2.3 shows a typical calibration curve of the electromagnetic flow meter in the THESYS technology loop of the KALLA laboratory [Knebel, *et al*., 2003]. There is a perfect linear relationship between induced potential and power supply to the pump. Due to the temperature dependence of the magnetic field, such a calibration has to be done for each operating temperature of the magnet.

Figure 11.2.3. Calibration curve of the DC electromagnetic flow meter (measured DC voltage as a function of the pump supply current) in the technology loop THESYS. Here the induced potential PMF is shown as a function of the pump power.

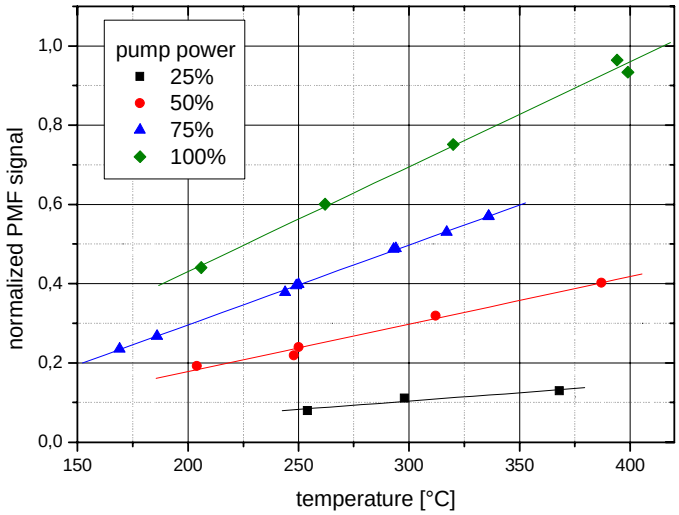

Operational characteristics

Figure 11.2.3 shows the normalised PMF signal plotted against temperature. Here, a clear linear dependency is observed for the four selected pump power stages. The slope of the four lines obviously varies linearly with the flow rate. Since a linear dependency between flow rate and PMF signal is expected, one can construct a linear equation with temperature depended slope:

$$V\left(U_{PMF}\right) = \frac{U_{PMF} - b}{m_T \cdot T + c} \tag{11.4}$$

In Eq. (11.4) V is the flow rate, U_{PMF} the PMF signal, T the temperature, m_T the temperature dependent slope (sensitivity) of the PMF and b and c temperature depending offsets, which will be determined from the calibration against the heat balance. From the change of the slope of the lines in figure m_T can be calculated and Eq. (11.4) gives the flow rate for a measured PMF signal.

On the left side of Figure 11.2.4 the results of the temperature correction is plotted in terms of the calculated flow rate against the pump power. From an error propagation analysis the uncertainty is calculated to 2% at a linear regression coefficient of 99.84%. The disadvantage of this method is the necessity of measurements at every point in the whole parameter range of flow rate and temperature to conduct the described calibration. This is a great effort and an isothermal operation is recommended, because this would require only two calibration measurements.

There is another argument against a protracted calibration process: the instable long-term behaviour of the investigated PMF systems in lead-bismuth. In the section of the PMF signal time series on the right side in Figure 11.2.4 an example for the observed discontinuities is shown. The jumps in the signal, which was taken at constant flow rate, can easily reach 20 times of the actual value. These annoyances are produced by galvanic reaction at the interface between pipe wall and liquid metal close to the electrodes and are worsened by accumulating impurities at these positions. Additionally, the corrosion of the pipe material (liquid metal corrosion and/or oxidation) changes the liquid-solid interface properties and causes a drift of the PMF signal. A favourable positioning and the use of line electrodes can work against these problems, but a recalibration in regular intervals is still necessary.

Figure 11.2.4. Flow rate calculated from temperature corrected PMF data according to Eq. (11.4) (left); outliers of the PMF signal in a section of the time series (right)

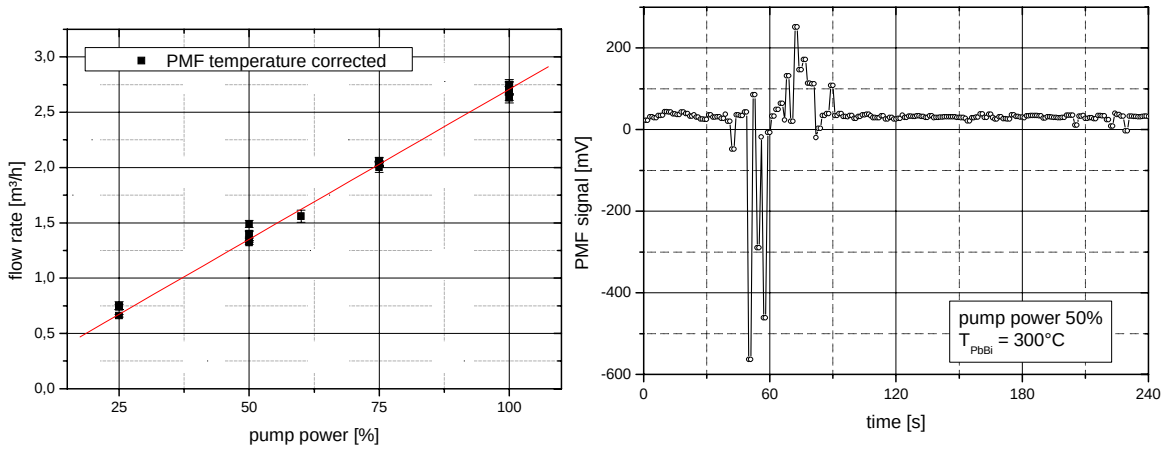

11.2.1.2 AC electromagnetic flow meter (EMFM)

A possibility using electromagnetic effects to measure the flow rate which suffers not from these problems is the electromagnetic frequency flow meter (EMFM). The general measurement principle of such an induction flow meter is that the motion of an electrically conducting fluid in an imposed field B produces an induced field B' which is proportional to the flow rate in the first order. This method involves an effect which is proportional to the fluid conductivity σ. Indeed, if the fluid velocity is known this method has been used to measure the conductivity of ionised gases [Lin, *et al.*, 1955]. The attraction of the EMFM is that its indication is directly electrical and no transducer is required which allows a large temporal resolution. Moreover, for the acquisition no direct contact of the sensor with the operation fluid is necessary, so that material compatibility issues play a role.

The earliest proposal for an EMFM has been made by [Lehde and Lang, 1948], which scheme is illustrated in Figure 11.2.5. The two coils A and C are energised in series-opposition so as to produce an AC magnetic field of the form illustrated in Figure 11.2.5 at the bottom. In the absence of a fluid motion the field is symmetrical and induces no signal in the sensing coil B according to the induction equation. As soon as flow occurs, the magnetic field lines are dragged downstream by $(u\nabla B)$ and a signal appears in coil B, which is proportional to the flow rate to the first order. But great care is necessary that there is no output signal in case of zero flow and in practice it is hardly feasible to produce a geometrically exact symmetric arrangement. Thus a precise fabrication is required otherwise the genuine signal, which is quite often small, will be lost among stray signals.

The flow direction can be detected by the sign of the RMS value of the sensing coil. The magnitude of the RMS value in the sensing coil is proportional to the magnetic Reynolds number of the fluid flow Re_m, where Re_m is calculated according to Eq. (11.5).

$$Re_m = \mu_0 \sigma(T) u_m d \tag{11.5}$$

where μ_0 is the magnetic permeability of vacuum, given as $4\pi\ 10^{-7}$ $As/(Vm)$, σ the specific electric conductivity of the fluid as a function of the temperature T, u_m the mean flow velocity within the duct and d its diameter. The magnetic Reynolds number weights the induced magnetic field to the initially by the AC current applied magnetic field. If the temperature remains constant the measured *RMS* value of $\Delta\phi$ is proportional to the mean fluid velocity u_m.

Figure 11.2.5. Operation principle of an electromagnetic frequency flow meter (EMFM) freely adapted from [Lehde and Lang, 1948]

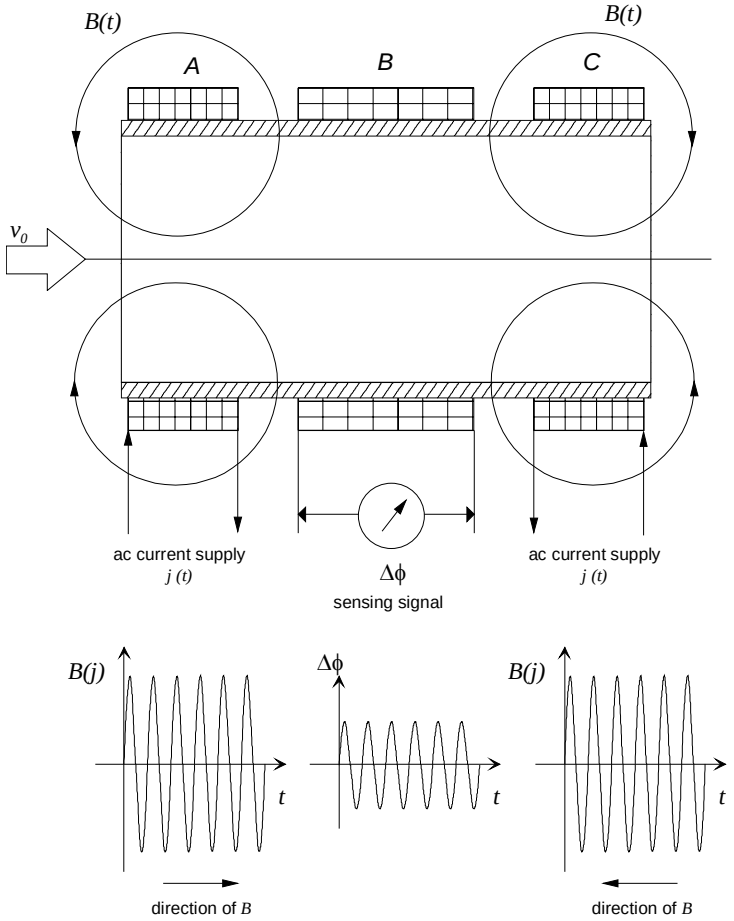

Potential error sources of the PMF sensor and the correct installation

However, this linear increase of the signal with the velocity and hence this operation principle only is valid if the magnetic Reynolds number Re_m is significantly smaller than unity. Only then the induced potential ($u_m \times B$) and the associated Lorentz-force ($j \times B$) can be approximated by the ($u_m \times B_{imposed}$) and ($j \times B_{imposed}$). But, if Re_m is of O(1) the non-linear contributions ($u_m \times B_{induced}$) and ($j \times B_{induced}$) become important. Other non-linear behaviour will occur if the imposed magnetic field $B(t)$ is strong enough to perturb the flow pattern. This effect is expressed by the Hartmann number Ha or (M), which weights the electromagnetic forces versus the viscous ones, and the Stewart number St, (often called interaction parameter). The latter one can be confessed as the ration of the electromagnetic forces versus the inertial forces within the fluid. Both quantities are calculated according to Eq. (11.6). They must be smaller than unity [Shercliff, 1987] throughout the operation range of the electromagnetic induction flow meter.

$$Ha = dB_{max}\sqrt{\frac{\sigma(T)}{\rho(T)\cdot\nu(T)}} \text{ and } St = \frac{d\sigma(T)B_{\max}^2}{\rho(T)u_m} \tag{11.6}$$

In Eq. (11.6) ρ is the fluid density, B_{max} the peak magnetic induction and ν the kinematic viscosity of the fluid.

Also for the sensing coil counteracting demands exits. One the one hand a lot of wire turns are required in order to detect smallest flow rate changes without using sophisticated AC amplifiers. But, on the other hand the more wire turns the coil has the more enforced the problem of pick-up effects is. The pick-up effect is meant the occurrence of stray AC signals superimposed on the flow dependent signal. The main source of pick-up are stray alternating fields from nearby placed equipment, such as electromagnetic pumps and AC powered equipment like ventilators, personal computers, etc. They can never be suppressed entirely and a large effort has to be directed into separating the wanted from the stray signals. As a rule, separation of the signals is achieved by exploiting the fact that the flow dependent signal and the pick-up are in quadrature, the first being proportional to the magnetic field strength, and the second to its time-derivative [Davidson, 2001]. This calibration necessitates elaborate electronic equipment.

Another complication is caused by phase shifts due to eddy currents in nearby solid and fluid conductors, because of the generation of harmonics through the non-linearity of the material or because of capacitive pick-up. Another source of trouble can be resonance or beats when the flow contains slight periodic fluctuations due, for instance, the use of electromagnetic or mechanical pumps running at or near synchronous speed. A technically feasible solution to minimise pick-up effects is a complete enclosure of the EMFM device by means of a ferromagnetic foil, being thick enough to run not into saturation of external DC and AC magnetic fields. This foil has to be grounded through the liquid flow far away of any eddy currents.

Finally, also some limitations concerning the AC current feed $j(t)$ have to be considered, which are also of contradictory nature. A minimisation of pick-up effects is achieved if a low frequency of $j(t)$ is used but if it is necessary to study the instantaneous of transient or pulsating flows the frequency must be at least three times higher than the highest frequency of interest occurring in the flow. Also frequencies have to be omitted which are a factor of the environmental power supply in order to avoid the generation of sub- and super-harmonics in the sensing signal. Of course, also a definite upper limit of the acceptable frequency exists. If the fluid is a good conductor the frequency must not be so high as to cause a skin-effect, while if the fluid is a poor conductor the frequency ω, which is $\omega = 2\,\pi\,f$, must not be so high that dielectric relaxation is not virtually instantaneous. The condition for there to be no skin-effect is:

$$\omega d^2 \mu \sigma(T) << 1 \tag{11.7}$$

and for immediate dielectric relaxation, which means a negligible displacement current, is given by:

$$\frac{\omega \varepsilon \varepsilon_0}{\sigma(T)} << 1 \tag{11.8}$$

where ε is the permittivity of the fluid and ε_0 the electric field constant given by $\varepsilon_0 = 8.85419\ 10^{-12}$ $As/(Vm)$. In case of liquid metals the permittivity ε is closely over unity, i.e. 1.01 [Siemens, 1969].

A photograph of an EMFM flow meter taken during the fabrication (a) and its installation in the THESYS loop of KALLA (b) is shown in Figure 11.2.6. For the calculation of the magnetic peak induction Eq. (11.9) is used:

$$B_{\max} = \frac{I_{\max} \cdot R}{n(Lf)\pi d_{m;Coils,A}} \tag{11.9}$$

where R is the ohmic resistance of the coils, L the coil width, n the number of current turns and $d_{m,Coils,A}$ the mean diameter of the feeding coils. As long as the Stewart number and the magnetic Reynolds number are significantly lower than unity a linear behaviour of the flow meter with respect to the temperature can be expected. The linear dependence of the signal induced in a typical EMFM flow meter for heavy liquid metals as a function of the pumping power for a constant temperature of 300°C and different feeding currents and frequencies is shown in Figure 11.2.7.

An exact theoretical analysis of the EMFM is usually difficult and an empirical calibration for each device is inevitable.

Figure 11.2.6. (a) EMFM fabrication at the KALLA laboratory.
(b) Installation of the EMFM in the technology loop THESYS of KALLA.

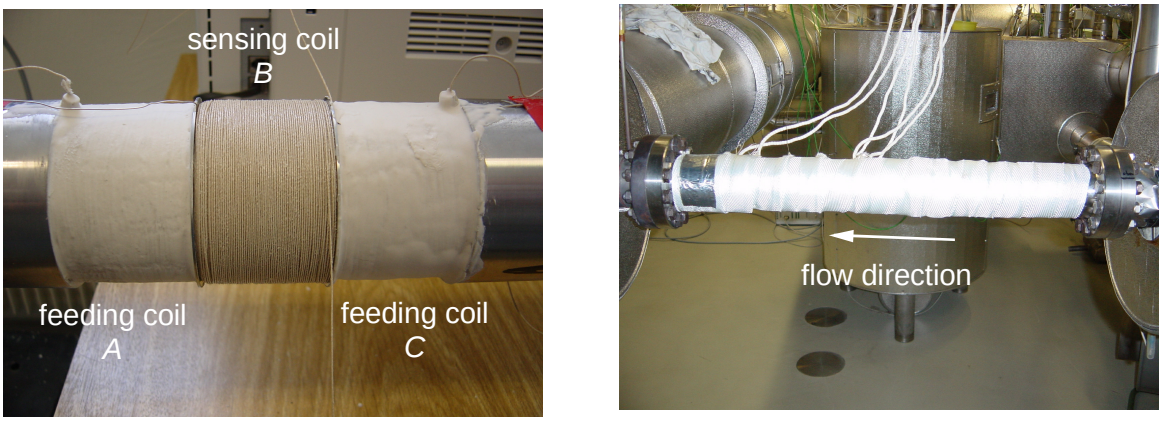

(a) (b)

Figure 11.2.7. Measured EMFM signal as a function of the pumping power for different feeding currents and feeding frequencies of the pump at a constant temperature of T = 300°C in the THESYS loop of KALLA: Characteristics (left) and calculated flow rate (right).

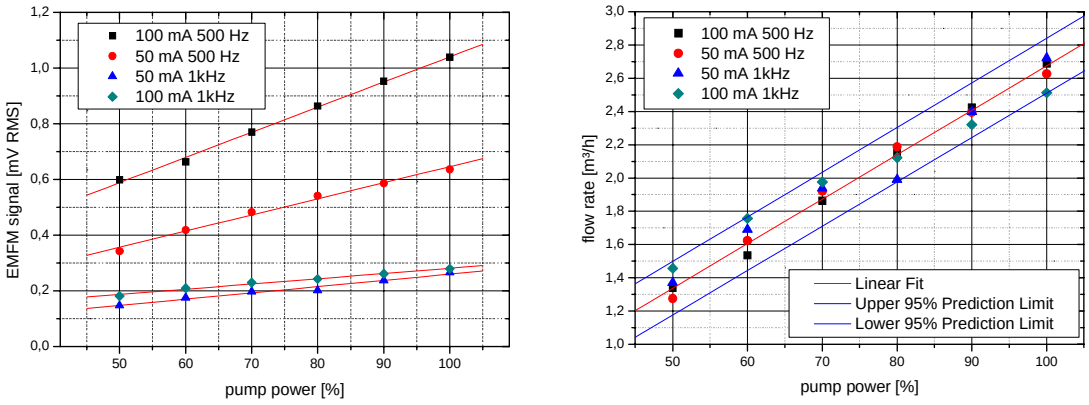

Operational characteristics

For a frequency of 500 Hz an increase of the EMFM signal with higher feeding current is obvious, but there is hardly an effect at a frequency of 1 kHz. This is a clear indicator for the occurrence of the skin effect. The magnetic field can penetrate just a thin boundary layer where the fluid moves so slowly that a change of the induced field strength causes only a marginal change of the output signal.

Consequently the performance of the EMFM flow meter increases with lower frequency and the best is found for 100 mA feeding current at 500 Hz. Higher feeding currents are not feasible because the strong magnetic field would cause MHD effects which change the flow pattern.

To verify the linearity of the characteristic, the flow rate was calculated using the result of a heat balance at 100% pump power. The results are plotted against the pump power shown in the right diagram on Figure 11.2.7. All values are found to lie inside the 95% prediction limit of their linear regression regardless of the parameter used for the feeding current. If a reliable calibration can be made, the EMFM is a very stable and robust flow rate measurement device for lead-bismuth loops.

11.2.2 Momentum-based flow meters

11.2.2.1 Turbine flow meter

In a turbine flow meter the measuring element is an axial rotor, turned by the force generated by the flowing fluid pushing onto the turbine blades. In the most applications this rotation will be picked up by a magnetic sensing coil placed onto the housing in the immediate vicinity of the interiorly passing blades. The measured rotation frequency is direct proportional to the volumetric flow rate. In reality bearing friction and dependencies on the flow profile, the viscosity of the fluid and eddy production in the turbine cause a disturbance of the linear characteristics. These influences are compensated by means of integrated flow straighteners and factory calibrations with a model fluid of the same viscosity as the future working fluid. Turbine flow meters like that shown in Figure 11.2.8 are commercially available for different pipe diameters [Natec Schultheiß, 1999]. They are used for flow rate measurements of gases and turbulent flowing, low viscosity fluids and feature high measurement accuracy.

Figure 11.2.8. Construction sketch of a turbine flow meter [Natec Schultheiß, 1999]

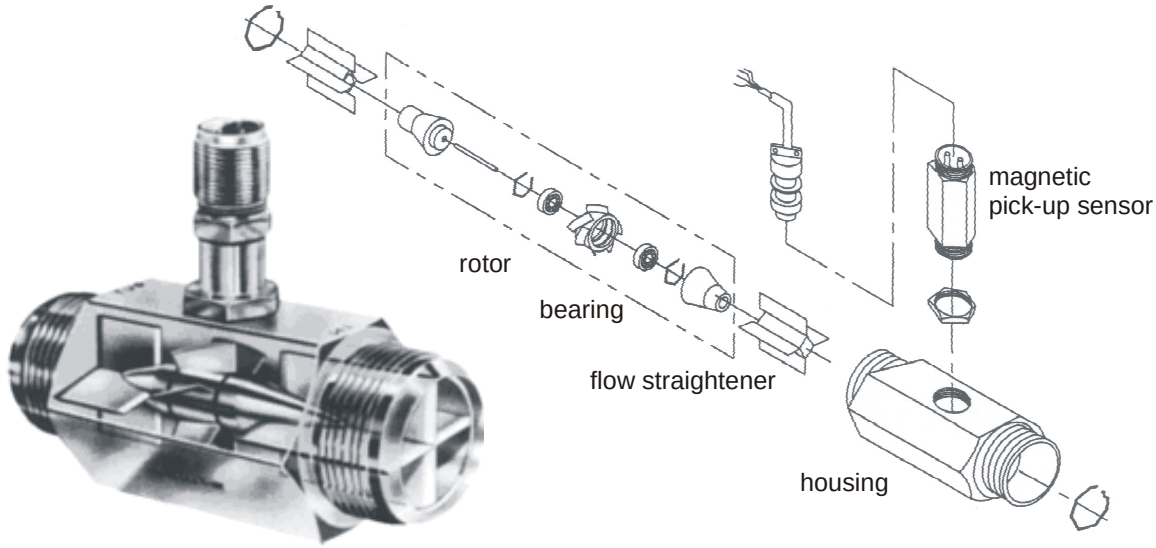

For the application in liquid metals the question for compatible materials arises. Rotor and bearing have to withstand the corrosive environment and high temperature of the fluid. Because of their relatively wide conduit, turbines are rather unsusceptible to floating particles, but in heavy liquid metals impurities buoy upwards and can accumulate in the top region of the rotor housing. Hence, the narrow gap between rotor and housing can plug up and destroy the turbine.

An advantage of the turbine flow meter is the possibility to use it as a measurement standard, because its mechanical measurement principle depends only on a few very well known parameters and calibrations can be done with model fluids. Thus the turbine was selected for qualification in lead-bismuth flows.

Operational characteristics

For the tests of a turbine flow meter a device from the company Natec Schultheiß was purchased. The selected model FT-1600-YBBLED-6108 is a measurement turbine for liquids with a magnetic inductive pick-up system. Housing and rotor consist of stainless steel, journal, axis and bearing of carbide. As specified, fluid temperatures up to 600°C are allowed with this material combination, but the magnetic inductive pick-up has to be cooled [Natec Schultheiß, 1999]. The turbine was calibrated in a company laboratory with an oil mixture, which acts as a model for lead-bismuth at low temperature by adjusting its viscosity. Figure 11.2.9 shows a photograph of the used turbine flow meter and a view into its duct with the rotor.

Figure 11.2.9. Photographs of the Natec Schultheiß turbine flow meter installed in the THESYS loop of KALLA

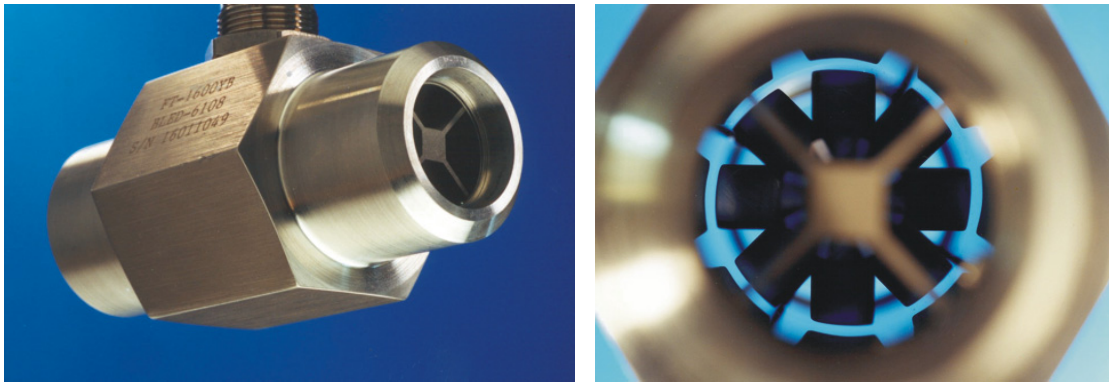

To evaluate the performance of the turbine flow meter, a heat balance calibration was conducted like for the electromagnetic flow meters. Measurements were made at lead-bismuth temperatures from 200 to 250°C.

Figure 11.2.10 shows the flow rate as a function of pump power measured by means of the turbine flow meter in comparison with the values derived from the heat balance. A systematic error between the two independent measurement methods was found, but the uncertainties in the heat balance are higher due to the difficult evaluation of heat losses. Therefore, the results of the turbine flow meter are preferred and the linear regression coefficient amounts to 98.7%. For the further considerations in the analysis of the heat balance the heat losses were corrected by 2.1% to achieve consistency between the measurements of turbine and heat balance.

Figure 11.2.11 shows slices out of the time series from turbine and heat balance at a lead-bismuth temperature of 375°C and 100% pump power. In the left chart the deviation between the signals is lower than 1% and the limits of variation is ±0.02 m^3/h which is in the range of the expected flow rate fluctuation in the THESYS loop.

After two weeks of correct continuous operation repeated collapse of the turbine flow meter signal was observed as shown in Figure 11.2.11 in the right graph. The assumption that a problem with the bearing of the rotor is responsible for the signal losses was confirmed a few days later by a post-failure

Figure 11.2.10. Flow rate measured by turbine and calculated from a heat balance as a function of pump power at lead-bismuth temperatures between 200 and 250°C in the THESYS loop of KALLA

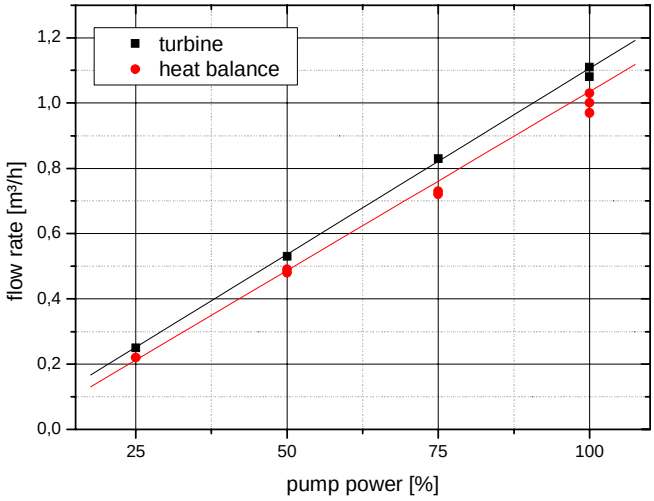

Figure 11.2.11. Time series of flow rate acquired by turbine and heat balance before (a) and after (b) turbines bearing damage at 100% pump power at THESYS, KALLA

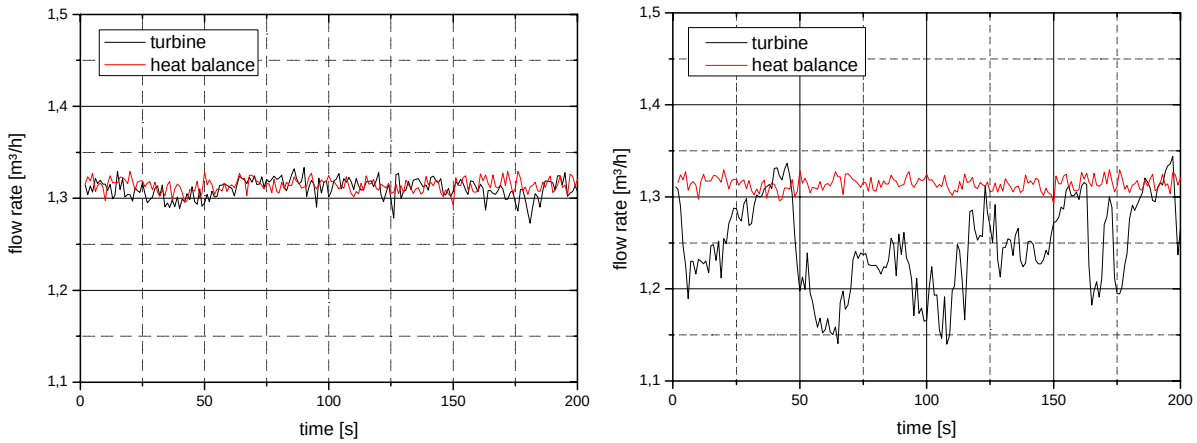

analysis of the turbine: corrosion has destroyed the journal and bearing material at the heavily loaded spots, which were at the top of the bearing, because the rotor swam up in the heavy liquid metal. The turbine flow meter provides reliable data with a high accuracy, repeatability and linearity, but materials have to be found to assure a long term stability of the mechanical components in the liquid metal flow. Then a turbine flow meter could be used as a calibration device for PMF or EMFM systems.

11.2.2.2 Gyrostatic flow meters

The gyrostatic flow meter measures directly the mass flow in a tube. The measurement principle used is the coriolis force. If a liquid flows through a U-tube oscillating on axis A (see Figure 11.2.12), in both branches of the U-tube coriolis forces of opposite direction appear. They lead to an oscillation around axis B. The magnitude of the angle χ around axis B is directly proportional to the mass flow through the U-tube.

Figure 11.2.12. Measurement principle of a gyrostatic mass flow meter

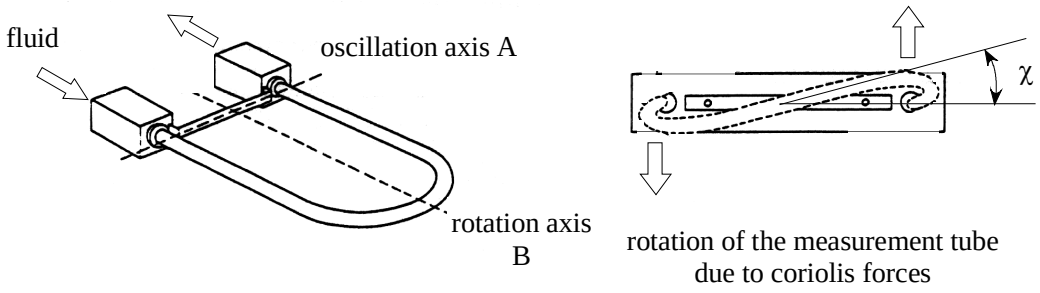

This measurement method is independent of the kinematic viscosity, the temperature, the flow profile and the gas content in the fluid. The used mass flow meter can dependent on the model be adjusted step-less in its measurement range via a remote control from the operation room. Moreover, the instruments offer the possibility to a self-calibration. For the calibration the fluid in the measurement tube has to be at rest. This can be done via two valves interconnected in the line at inlet and outlet of the mass flow meter. The accuracy of the mass flow meter is ±1% or 1/100 of the chosen scale.

The temperature operation range of the instrument is limited from -240°C to 204°C at a maximum pressure of 40 bars. But successful runs with sodium and sodium potassium alloys have shown its applicability to liquid metal systems, see e.g. [Barleon, *et al*., 1996] or [Stieglitz and Müller, 1996]. This temperature restriction is one of the most critical parts for the use in liquid metal systems. Also the component should not be installed close to magnetic fields due to the electronics in the instrument in order to avoid disturbances in the electronics.

11.2.3 Pressure- and counter-based flow meters

11.2.3.1 Von Kármán vortex street flow meter

If a fluid flow passes a cylindrically shaped body a Kármán vortex street is formed downstream which is characterised by a periodic vortex arrangement of counter rotating vortices as depicted in Figure 11.2.13. The frequency of the periodically detaching vortices is directly proportional to the fluid velocity u_m within a certain velocity threshold. The frequency of the vortices f in liquid metal flow can be detected, e.g. by a simple pressure transducer or any other mechanical device. The two dimensionless physical numbers describing this simple problem are the Strouhal number *Str* and the hydraulic Reynolds number *Re* built with the diameter d of the cylinder.

$$Str = \frac{f\ d}{v_0} \quad \text{and} \quad Re = \frac{u_m\ d}{\nu} \tag{11.10}$$

The Kármán vortex street is a regular hydrodynamic instability existing in a Reynolds number regime between $60 \le Re \le 5\ 10^3$. Beyond this Reynolds number range a full turbulent mixing appears and the regular structure of the vortices too. Nevertheless, taking use of the vortex pattern formation and the simple count of fluctuations (the absolute magnitude of the signal does not matter) the v. Kármán vortex street flow meter represents a simple tool to measure extremely small velocities. For Reynolds numbers $Re \ge 60$ the Strouhal number of a flow around a cylinder is constant at a value of $Str = 0.2$. Considering a lead bismuth temperature of $T = 300$°C and a cylindrical rod with a diameter of $d = 6$ mm the smallest resolvable velocity is 1.7 mm/s. The frequency to be counted by a pressure gauge is then $f = 0.06$ Hz.

Figure 11.2.13. Principle of the formation of a Kármán vortex street behind a cylindrical obstacle

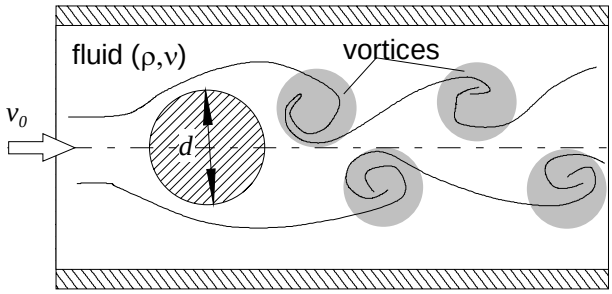

Of course, using this measurement technology some constraints regarding the inlet conditions exist. The flow facing the cylindrical obstacle has to be fully developed in the sense that no lateral pressure gradients appear and the axial derivatives in flow direction are zero. This leads for turbulent flows immediately to developing length of at least 30 hydraulic diameters of the pipe. A technical feasible solution to overcome this long developing length, which is in case of a 60 mm tube about 1.8 m, is the installation of a flow straightener, which equalises the flow. Depending on the installation environment an arrangement of parallel small tubes may be not sufficient, for instance directly after a 90° bend.

However, due to the small kinematic viscosity of lead bismuth a Reynolds number of $Re = 5\ 10^3$ is very fast exceeded. In the intermittent Reynolds number regime $5\ 10^3 \leq Re \leq 2\ 10^4$ the Strouhal number is not constant and thus not directly related to the mean velocity in the duct. In this specific regime the v. Kármán technique can be used only with additional calibration procedures, e.g. against a PMF or an EMFM. For $Re \geq 2\ 10^3$ the Strouhal number again shows an almost constant proportionality with the frequency. But it has to be stated that at high Reynolds numbers a non-linear correction has to be applied, which depends on the obstacle inserted in the duct. A calibration of the flow meter in the loop is hence inevitable.

11.2.3.2 Obstacle flow meters, nozzle and orifice flow meters

A combination of the v. Kármán flow meter with a pressure difference measurement method, as depicted in Figure 11.2.14, turned out to be a technically feasible solution. The pressure difference measurement method takes advantage of the fact that the pressure loss Δp of the flow around a circular obstacle expressed in terms of a c_W value is at Reynolds numbers of $Re \geq 5\ 10^3$ independent of the Reynolds number. The mean velocity u_m in the duct and hence the flow rate can be calculated using Eq. (2.11):

$$u_m = \sqrt{\frac{2\,\Delta p}{\rho\, c_W}} \tag{11.11}$$

The c_W values may be taken from [Beitz and Küttner, 1986] or other standard handbooks. In case of a 60 mm tube and a cylindrical rod with a diameter of 6mm the c_W value is $c_W = 0.82$. The independence of the c_W values of the Reynolds number holds up to $Re \sim 5\ 10^5$. In order to measure small velocities and to calibrate both techniques against each other pressure transducers resolving smallest pressure differences are required.

Figure 11.2.14. Measurement principle of a combined Kármán and pressure difference flow meter

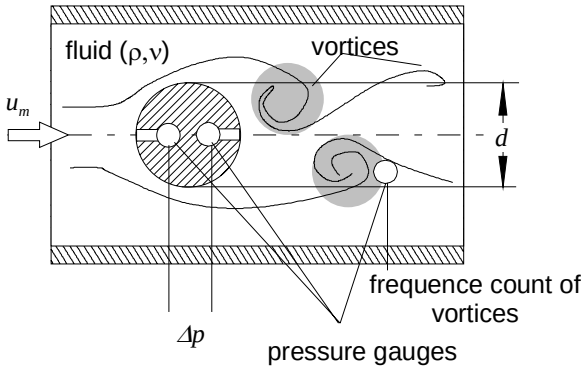

Operational characteristics

Here, in the THESYS loop we used pressure transducers capable resolving an absolute pressure of 12.5 Pascal. Thus, the minimal velocity to be resolved by the pressure difference method is a mean velocity of $u_m = 0.05$ m/s. To summarise, in case of the THESYS loop the operational range of the Kármán vortex street flow meter is from $1.7 \cdot 10^{-3} \le u_m \le 0.146$ (m/s) and the corresponding range of the pressure difference method is from $5\ 10^{-2} \le u_m \le 14.6$ (m/s), which is far beyond the technical capabilities of the THESYS loop. In Figure 11.2.15 the technical set-up of the combined flow meter type being installed in THESYS is illustrated.

Figure 11.2.15. Combined pressure difference and Kármán vortex flow meter as it is used in THESYS and THEADES. (b) Flow straightener being installed upstream the flow meter. (c) Flange for insertion of cylinder and pressure taps.

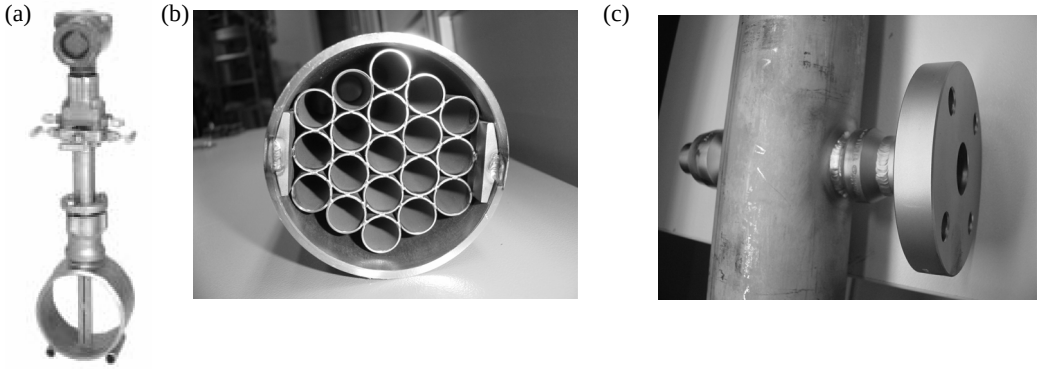

Orifices, nozzles or Venturi nozzles as illustrated in Figure 11.2.16(a) are commonly used flow meters and a broad overview is given in the [DIN tables, 1982]. The pressure loss coefficients ξ_2 related to the smallest cross-section d_2 are shown in Figure 11.2.16(b) as a function of different diameter ratios d_2/d_1. The data have been collected from [Herning, 1966] and [White, 1986]. Using the continuity condition the pressure drop coefficient ξ_1 is obtained from Eq. (11.12).

$$\xi_1 = \left(\frac{d_1}{d_2} \right)^2 \cdot \xi_2 \tag{11.12}$$

Knowing ξ_1 the mean velocity u_m and hence the flow rate can be calculated using Eq. (11.13):

$$u_m = \sqrt{\frac{2\Delta p}{\rho \xi_1}} \tag{11.13}$$

where the pressure difference Δp is measured between the positions indicated in Figure 11.2.16(a).

Figure 11.2.16. (a) Orifice designs used for flow rate measurements. (b) Pressure drop coefficient ξ_2 as a function of the diameter ratio d_2/d_1 for the different orifice geometries from figure (a)

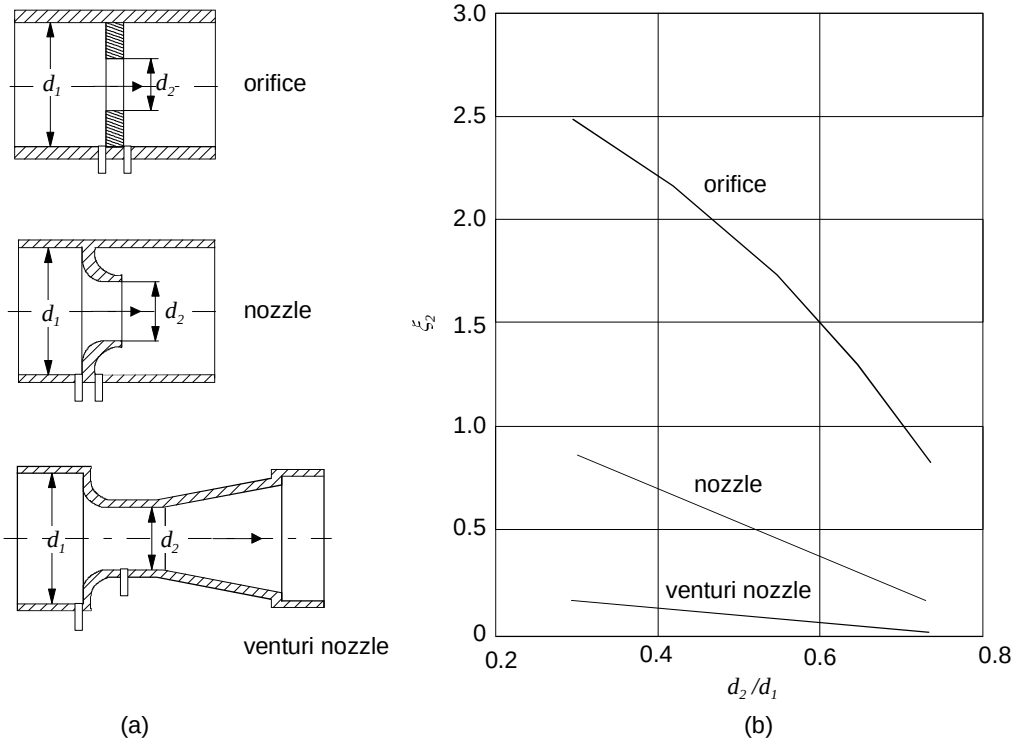

Pitot and Prandtl tubes also often used to measure flow rates rely also on the measurement of pressures. By means of positioning the tube as depicted in Figures 11.2.17(a), (b) in the flow the total pressure p_0 can be measured by:

$$p_0 = p_1 + \rho_{meas}\, g\, h, \tag{11.14}$$

where p_0 is the absolute outer pressure and ρ_{meas} the density of the measurement fluid. Using Pitot tubes an absolute pressure transducer is connected at the end of the line so that p_1 is given for $u = 0$. The dynamic pressure p_{dyn} can be calculated from the difference of the total pressure p_0 and the static pressure p_{stat} using a Prandtl tube.

By measuring $p_{dyn} = p_0 - p_{stat} = \rho_{meas} gh$ the local velocity $u(z)$ can be calculated using Eq. (11.15):

$$u(z) = \sqrt{\frac{2\, p_{dyn}}{\rho}} \tag{11.15}$$

While using Pitot-tubes as flow rate measurement devices, at least two-sensors have to be located within the tube according to ISO3966-1977, see Figure 11.2.17(d). Since the velocity profile varies as a function of dimensionless radius r/D the Pitot tubes have to be placed in such positions where this deviation is minimal. In Figure 11.2.17(c) the dimensionless velocity is depicted as a function of the radius [VDI, 2001]. It shows that at $r/D = 0.381$ in a Reynolds number range $Re = 4 \cdot 10^3$-$3.2 \cdot 10^6$ the deviation is less than 3%. Another error source while using Pitot tube flow meters is that they require a developing length of at least 25 tube diameters after a 90° bend. For developing lengths of more than 35 diameters the systematic error is minimised to less than ±0.5%.

Figure 11.2.17. Local flow velocity measurements using Pitot (a) and Prandtl tubes (b). (c) Local axial velocity normalised by the mean velocity as a function of the dimensionless radius *r*/*D* at different Reynolds numbers *Re*. (d) Schematic set-up of the Pitot flow meter.

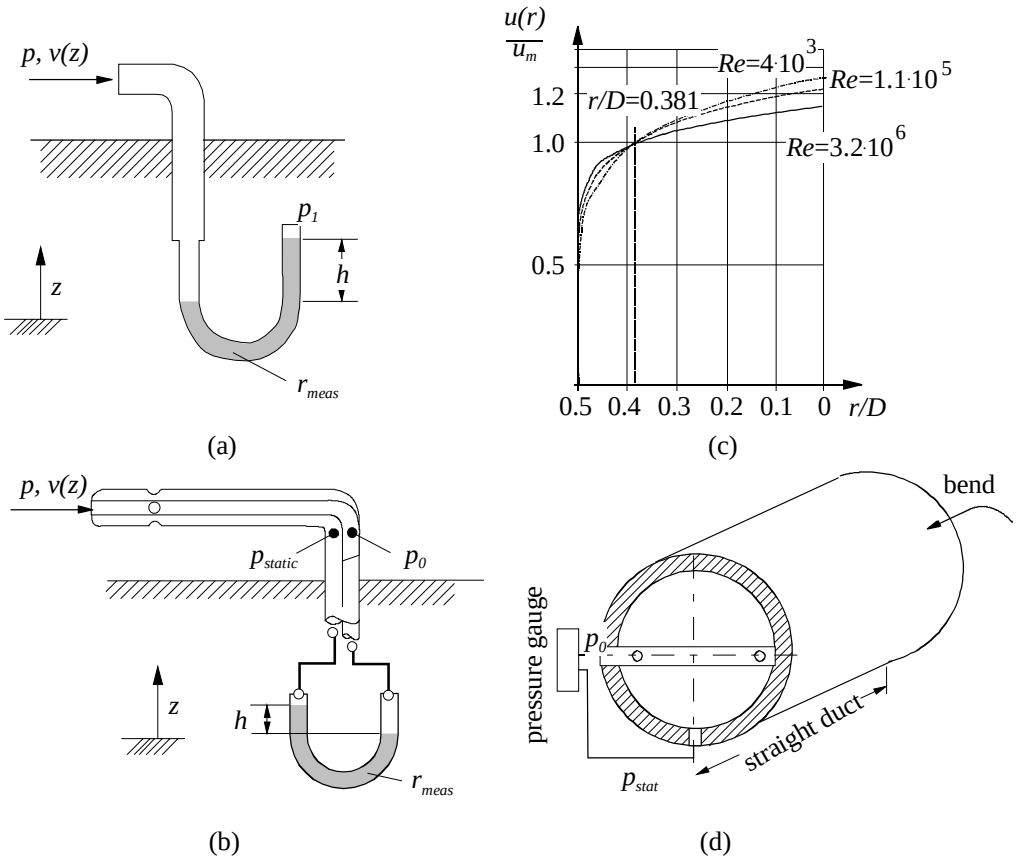

11.2.4 Ultrasound transit time method (UTT)

The velocity of propagation of sound waves in moving fluids changes with the flow velocity of the transmitting medium. An ultrasound wave is sent through a fluid under an angle α to the flow direction from a sender A to a receiver B as shown in Figure 11.2.18 [Gaetke, 1991] and [Millner, 1987].

If the fluid is not moving the signal travels with the sound speed c from A to B from what the transit time is calculated to $t_0 = L/c$. But if the fluid flows with the mean velocity u_m the signal is accelerated by the portion of the projection of this velocity to the measurement line. Accordingly the

signal is decelerated by the same amount on its way from B to A. The transit times of the signals can then be calculated by:

$$t_{AB} = \frac{L}{c + u_m \cos\alpha} \quad \text{and} \quad t_{BA} = \frac{L}{c - u_m \cos\alpha} \tag{11.16}$$

Transformation yields to an expression for the mean flow velocity:

$$u_m = \frac{L}{2\cos\alpha}\left(\frac{1}{t_{AB}} - \frac{1}{t_{BA}}\right) \tag{11.17}$$

In practice the determination of the transit time difference from the phase shift between the two signals $\Delta t = t_{AB} - t_{BA}$ is common and with the postulate $(u_m/c)^2 << 1$ one obtains:

$$u_m = \frac{c^2}{2L\cos\alpha}\Delta t \tag{11.18}$$

Compared to Eq. (11.17) in expression (11.18) the mean velocity depends on the sound speed. This disadvantage is accepted because the determination of the usually very short transit times appearing in Eq. (11.16) is technically difficult and less accurate than the identification of its difference. Due to the fact that beside the sound speed only geometric measures occur in the equation, the ultrasound transit time method can be used for calibration of other measurement methods if the sound speed in the fluid is known and a fully developed flow profile is present.

Figure 11.2.18. Principle of ultrasound transit time measurement freely adapted from [Gaetke, 1991]

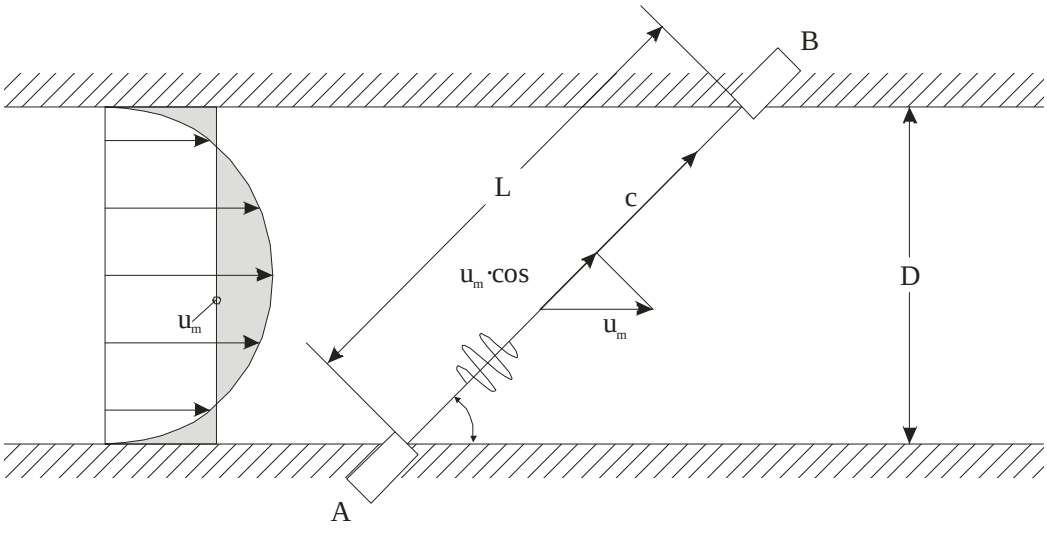

To generate ultrasound mainly piezoelectric materials are used (quartz, lead zirconate, barium titanate) whose Curie-temperature, above which they get instable and irreversible destroyed, limits the applicable temperature range to a maximum of about 150°C. For measurements in high temperature fluids like liquid metals wave guides are required. [Liu, *et al*., 1998] have developed bundled wave guides at the company Panametrics for ultrasound transit time measurements in fluids and gases for

temperatures up to 450°C. They describe wetted and clamp-on systems and show results of their application for flow rate measurements at temperatures between 200 and 300°C. The fact that ultrasound is transported as a longitudinal pressure fluctuation also in opaque media turns it into a promising method for measurements in liquid metals.

In order to transport a significant energy through the structure into the fluid the material thickness of the emitter has to be adapted to the fluid. Here, the impedance Z which is the product of the sound speed c and the density ρ has to be taken into account. The permittance D of an acoustic wave through a solid-fluid interface can be expressed as a function of the thickness of the material d, the wavelength λ of the sound wave and the impedance of the fluid and the liquid Z_i according to Eq. (11.19):

$$D = \frac{1}{\sqrt{1 + \frac{1}{4}\left(m - \frac{1}{m}\right)^2 \sin^2 \frac{2\pi d}{\lambda}}} \quad \text{and} \quad m = \frac{Z_1}{Z_2} \tag{11.19}$$

The permittance of a steel plate for a longitudinal wave at a frequency of 4MHz towards water and lead-bismuth as a function of the thickness is shown in Figure 11.2.19. This permittance is only achieved if the interface is perfectly physically wetted in the adhesive sense and no mode transitions of the wave at the interface appear.

Figure 11.2.19. Permittance D of steel at a frequency of 4 MHz as a function of the plate thickness d for the interface steel-water and steel-PbBi

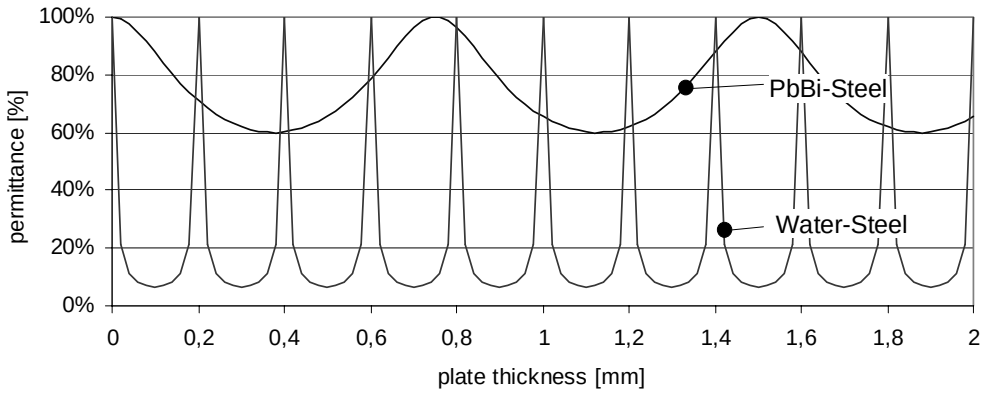

Other sources of uncertainties using the ultrasound are the absorption and the sound scattering. Finally, the anisotropy of the sound speed has to be taken into account. In case of measuring flows containing a temperature gradient, the sound speed varies with the square root of the temperature and thus the temperature has to be known and adequate countermeasures to be foreseen.

The mode transition problem at the interface leading to a significant decrease of the signal magnitude is solved by a specific sensor design. The mode transitions can in principle occur due to:

a) longitudinal to transverse wave transitions;

b) surface waves like Rayleigh-waves;

c) creep waves;

d) ring sound.

Operational characteristics

Crucial for the coupling of ultrasound is an adhesive wetting of the wave guides ends to transmit the oscillation energy into and out of the fluid. Hence, to guarantee the wetting a 2 µm thick sacrificial nickel layer can be applied on the wave-guides in a galvanic bath. Due to the high solubility of nickel in lead-bismuth the wetting can be preserved for the duration of the application, which results in 60% of the senders signal amplitude at the receiver.

Figure 11.2.20 shows the flow rate over pump power measured by means of the USTT and the PMF methods at two temperature levels. The PMF was calibrated at 70% pump power like described above and shows a good agreement with the USTT values at the other settings. The flow rates measured at a temperature of 376.5°C are about 5% higher than the ones at a temperature of 208.4°C, which is caused by a slightly better performance of the EM-pump at higher temperatures due to a lower contact resistance between the liquid metal and the pump channel.

Figure 11.2.20. Flow rate measured by USTT and PMF at temperatures of 208.4°C and 376.5°C as a function of the pump power

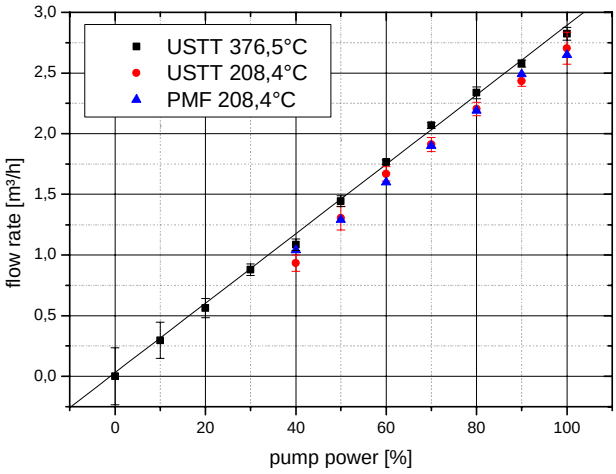

The nickel coating of the wave guides results in a stable coupling and therefore a small uncertainty of lower than 1% for flow rates of more than 0.5 m^3/h. The linear regression coefficient is calculated from the measurements at 376.5°C to 99.8%. Systematic errors occur in consequence of the test sections thermal elongation, which changes the length of the sound path appearing in Eq. (11.18). This error can be calculated to ~3% so that the complete uncertainty sums up to ~4%. For the Panametrics XMT868 a measuring range of ±12.2 m/s at an uncertainty of ±2-5% of the reading is given and coincides with the ascertained value. In principle bigger pipe diameters and higher flow rates reducing the errors and improving signal to noise ratio for the USTT method, because the transit time differences increase. In addition multiple ultrasound paths circumferentially arranged around the pipe can also increase the accuracy.

11.3 Pressure sensors

11.3.1 Types of pressure gauges and operation experience

Generally two types of pressure measurement devices are available in more or less direct contact with lead-bismuth. These types of sensors are also capable to measure local velocity distributions if

they are used in the context of a Pitot or Prandtl tube. Additionally, they can be used as flow meters of different principles in case an elevated pressure drop in the piping can be accepted by the individual user.

The first are the capacitive transducers illustrated in Figure 11.3.1, which measure the pressure difference (Δp) between two discrete points in a piping system. The pressure signal is absolutely obtained by an electric capacity change between to plates, here filled with silicon oil. As the transducer medium is only capable to withstand temperatures less than 250°C the connection between the liquid PbBi and the transducer itself is realised by an incompressible coupling medium. Here, often the eutectic sodium-potassium alloy $Na^{78}K^{22}$ is used with a melting point of -11°C. The use of a coupling medium limits the temporal resolution. The frequency response time of the transducer is typically limited to 5 Hz, which does not allow to measure fast fluctuations like velocity or flow rate oscillations. Figure 11.3.1(a) depicts a technical sketch of the difference pressure measurement sensor used in the Karlsruhe Lead Laboratory (KALLA). Nevertheless, the major advantage of the capacitive methods is their excellent stability and accuracy. They offer a high resolution (±12.5 Pascal), an absolute pressure signal, which is attractive for reactor applications, and additionally the zero point can be easily determined. But, they require a complex set-up of heating elements in the transmission line up to the coupling clutch, a precise fill and drain strategy to avoid bubbles and they are actually expensive.

Figure 11.3.1. (a) Schematical set-up of a capacitive pressure difference transducer using a coupling medium. (b) Photograph of an absolute pressure transducer using a fast Wheatstone bridge. (c) Test stand to measure liquid levels and pressure differences erected at ENEA/Brasimone.

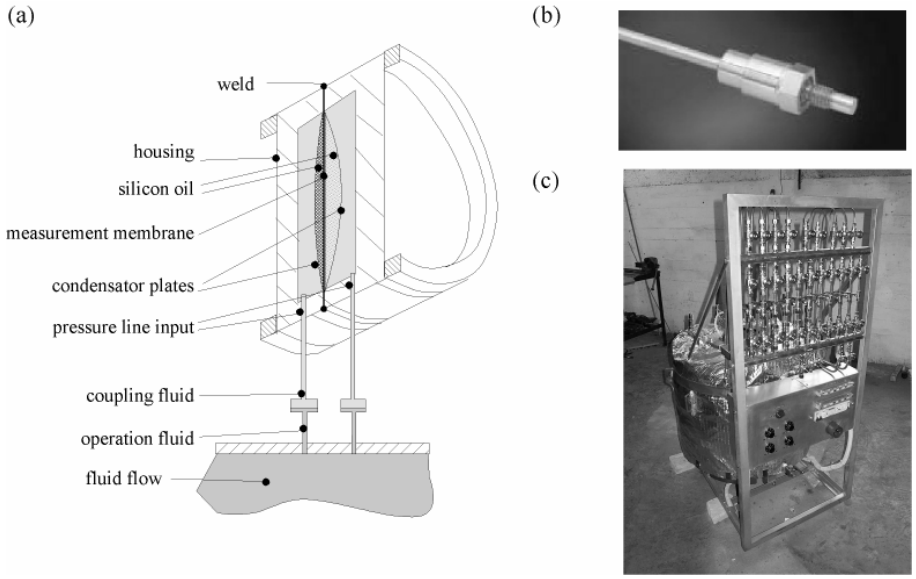

Another method to measure absolute pressures p is to use pressure gauges based on a fast Wheatstone bridge. These kinds of sensors are compact and can be directly screwed in any tap of the liquid containing piping. Due to their small dimension they have a negligible inertia and hence allow to detect fast oscillations of order of several hundred Hz. A photograph of such a sensor is shown in Figure 11.3.1(b). Due to the fabrication principle the maximal span is given and a calibration before each experimental run must be performed. Then, the pressure resolution is similar to that of the capacitive units. Nevertheless, this techniques which can sustain up to 480°C liquid metal temperature, is the preferred option for use in the Pitot and Prandtl tubes later described and used for recording local velocities.

A third option to measure pressures, differential pressures, liquid levels or flow rates is the bubbling technique, successfully performed in the lead bismuth loop CIRCE of ENEA. Here, bubbles of inert gas are injected via Venturi tubes into the liquid. While measuring the gas pressure in the bubble tubes, levels and pressures can be recorded at several locations simultaneously using only one sensor, which is not in direct contact with the liquid and thus temperature limitations for the use of such a kind does not exist. The technical realisation of a test stand proofing this principle at ENEA is illustrated in Figure 11.3.1(c). Besides simple set-up of the pressure cells operating at room temperature and the simultaneous recording at several positions the low price is rather attractive. Nevertheless, all results depend on the nozzle shape, the detailed positioning in the system and moreover an extensive calibration. Further, the temporal resolution is rather limited and a temperature correction must be performed because the surface tension of the liquid depends on it.

11.3.2 Pressure correction in fully developed turbulent pipe flow

Especially, in very fine resolution measurements, say, e.g. in benchmark experiments it may appear that misreadings of the wall static pressure occur, which are related due to the finite size of the pressure tapping. This effect was observed over a wide range of Reynolds numbers by numerous authors long ago as shown in the papers by [Allen & Hooper, 1932], [Ray, 1956], [Thom & Appelt, 1957], [Rayle, 1959], [Livesey, *et al*., 1962] but also by [Franklin & Wallace, 1970] and [Ducruet & Dyment, 1984]. A summary of the complete literature dealing with this problem is given by [Chue, 1975].

All results indicate that the correction term as a fraction of the wall stress continues to increase as the hole Reynolds number $d^+ = (u_\tau d)/\nu$ increases. For small holes relative to the pipe diameter the results follow a single curve, but for larger holes the data diverge from this universal behaviour at a point that depends on the ratio of the holes diameter to the pipe diameter. This effect becomes pronounced especially for large Reynolds numbers, which appear easily in heavy liquid metals because of their low kinematic viscosity ν. A flow structure within a pressure tapping yielding the pressure error is schematically shown in Figure 11.3.2.

Figure 11.3.2. a) Flow structure within the static pressure tapping. b) Variation of the non-dimensional pressure error Π as a function of the holes Reynolds number d^+ for different *d*/*D* after McKeon & Smits (2002).

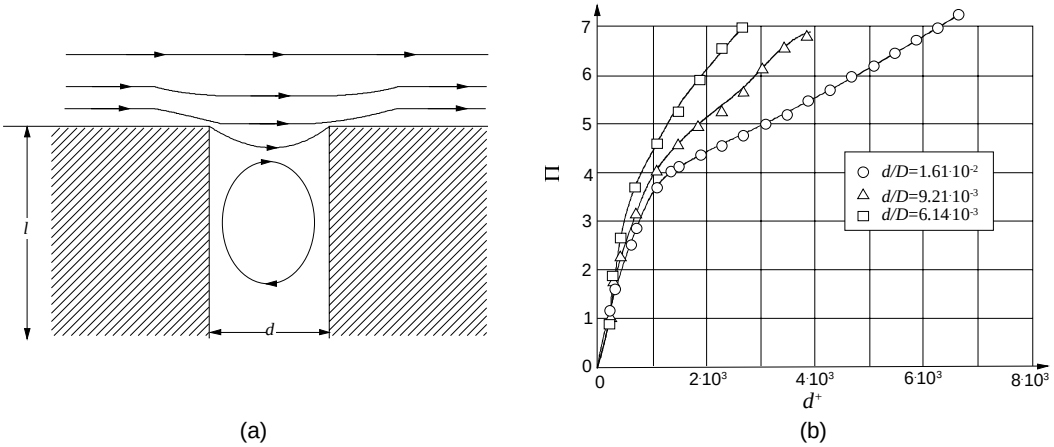

A dimensionless analysis performed by [McKeon and Smits, 2002] shows that the pressure error Δp depends on the hoe diameter d, the hole depth l, the diameter of the connection to the transducer d_c, the wall shear stress τ_w, the fluid density ρ and the kinematic viscosity ν. Within this context the

characteristic length scale of the facility, where the experiment is conducted, namely the pipe diameter D is important especially considering large holes. Then the non-dimensional error Π can be expressed by a dimensionless parameter group in the form:

$$\Pi = \frac{\Delta p}{\tau_W} = f\left(\frac{d\, u_\tau}{\nu}, \frac{d}{D}, \frac{l}{d}, \frac{d_c}{d} \right) \quad \text{with } u_\tau = \sqrt{\frac{\tau_w}{\rho}} \tag{11.20}$$

where u_τ is the friction velocity. Assume first that d/D, l/d and d_c/d are constant then the pressure error Π depends only on d^+. With decreasing hole Reynolds number d^+ (namely $d \to 0$) Δp tends to zero. Far from the wall dynamic and turbulent effects dominate the flow behaviour and thus for large d the ratio d/D becomes important. Shaw (1960) investigated the hole Reynolds number d^+ effect in a 50 mm diameter tube for flow Reynolds number up to $Re = 1.7 \cdot 10^5$. He found that the non-dimensional error Π increases with increasing d^+ but reaches an asymptotic limit of 3 for $d^+ = 750$. But he dismissed the effect d/D, because as d increases not only the hole Reynolds number increases but also d/D. Shaw suggested that the hole must become large enough to change the flow field itself and postulated this occurrence to appear at $d/D \sim 0.1$. For $d/D > 0.1$ the global flow patter in the pipe and which is even more important the flow over the tapping is changed leading to a miscellaneous pressure reading. In this case a correction due to the secondary flows appearing the pressure tap has to be performed. Further literature treating this topic may be taken from [Pozrikidis, 1994], [McKeon & Smits, 2002] or [Ligrani, *et al*., 2001].

The depth to diameter plays also a role in the pressure error, since it dictates the eddy system set-up within the cavity. Even the Allen & Hooper investigations 1932 show, that the error increases with l/d, but if l/d exceeds the value 2 [Chue, 1975] showed by an compilation of all previous experiments an asymptotic value is reached, which represents the "deep" limit for all Reynolds numbers. Consequently, a wide cavity behind the tapping reduces the error, while a contraction in diameter from the tapping to the pressure gauge can increase the error, see e.g. [Livesey, *et al*., 1962].

As a practical guide, it is suggested that if a Pitot tube and static tapping are used to make pressure measurements within a pipe flow, the static tapping should have a large and constant l/d, at least $l/d > 2$ to ensure that the flow structure within the cavity is fully developed and not changing with the Reynolds number. Second, a small ratio of tapping to pipe diameter has to be set-up, to prevent the tapping fundamentally altering the external flow.

11.4 Local velocity measurements

The viability of technical units like beam windows or fuel bundles requires often sophisticated information on the local velocity distribution and local heat fluxes in the geometry, which often can not be simulated numerically. The opaqueness of liquid metals excludes the use of optical methods which are commonly used in thermal-hydraulics. The intention to develop new measurement techniques to determine the local velocities in liquid metals arises from the following requirements:

a) Although there is a growing interest in measuring the local velocities in opaque fluids at high temperatures most of the currently developed techniques are only existent on laboratory scale and show no reasonable accuracy over a sufficiently long time period.

b) The measuring conditions in liquid metal facilities are often characterised by external magnetic fields or strong electric noise caused by heating elements, pumps or high power supplies.

c) Disturbances of the flow caused by the presence of the sensor should be prevented as much as possible.

d) The measurement range should cover low (mm/s) as well as high values of the velocity in terms of several meters per second.

This chapter presents a few measurement principles applied in the past decades successfully to liquid metal flows. Moreover, the operation principle, the necessary calibration methods and correction factors are described or the appropriate literature sources are cited.

For the intrusive methods like e.g. reaction probes, fibre mechanical probes, permanent magnetic probes or Pitot tubes corrections are necessary accounting for the impact of the probe on the velocity field to be measured experimentally. This effect is discussed extensively in the chapter of the Pitot tube, but it can be generally applied to all other intrusive methods.

11.4.1 Ultrasound Doppler velocimetry

A non-intrusive method to measure instantaneously whole velocity profiles is offered by the ultrasound Doppler velocimetry (UDV). The UDV technique is based on sending ultrasound pulses through the liquid instead of a continuous wave. The echoes from particles immersed in the fluid (which requires a flow seeding) are sampled. The related velocity information is obtained from the shift in position of scatters between ultrasound pulses and not from the Doppler frequency shift of the echoes. Hence, the velocity information is yielded from a correlation function. One of the major advantages of UDV is that it is a non-intrusive method, with which the velocity is scanned not only at one exclusive position like in a laser Doppler anemometer. It rather samples velocity information instantaneously at several positions along the ultrasound wave path. The operation principle is shortly explained and sketched in Figure 11.4.1.

The location of the measurement volume is given by relation (11.21)a, in which c is the sound speed and t_d the actual travelling time of the pulse. The spatial shift of the position ΔP between two pulses applying a pulse repetition time t_{prf} is given by Eq. (11.21)b.

$$P = \frac{c\,t_d}{2} \quad and \quad \Delta P = \left(P_2 - P_1\right) = u(z) t_{prf} \cos\theta = \frac{c\left(t_2 - t_1\right)}{2} \qquad (11.21)\ \text{a,b}$$

The time difference (t_2-t_1) is recorded by means of the phase shift of the echoed signals and can be expressed by relation (11.22)a, where f_e is the echo velocity. Finally, the velocity u(z) at a discrete co-ordinate z can be evaluated by Eq. (11.22)b.

$$\Delta d = 2\pi\, f_e \left(t_2 - t_1\right) \quad and \quad u(z) = \frac{c\,\Delta d}{2\, f_e \cos\theta\, t_{prf}} = \frac{c\, f_d}{2\, f_e \cos\theta} \qquad (11.22)\ \text{a,b}$$

with f_d representing the Doppler shift. Of course, an upper limit of the maximum measurable velocity and the maximum measurement depth exists. This constraint is expressed by the relations (11.23).

$$u_{\max} = \frac{c}{4 t_{prf}\, f_e \cos\theta} \quad ; y_{\max} = \frac{c\, t_{prf}}{2} \qquad (11.23)\ \text{a,b}$$

The UDV technique allows the instantaneous acquisition of whole velocity profiles. This is performed by a reconstruction of the velocity information in the following way. First, the length of the acquired echoes reflected from the particles within in fluid is divided into intervals of the temporal length $\Delta\tau_i$. The run time τ_i is associated with a measurement position in the duct y_i via the relation:

$$y_i = \frac{c\tau_i}{2} \tag{11.24}$$

Then the velocity within a discrete interval u_i can be calculated. This procedure determines the local resolution and the size of the measurement volume, which is given by the relations (11.25).

$$\Delta y_i = \frac{c\Delta\tau_i}{2} \quad \text{and} \quad \Delta y_e = \frac{c\Delta\tau_e}{2} \tag{11.25}$$

The whole process of the acquisition of a velocity profile is sketched in Figure 11.4.1.

Figure 11.4.1. Operation principle of the ultrasound Doppler velocimetry (UDV) to acquire local velocities in heavy liquid metal flows from Lefhalm (2004)

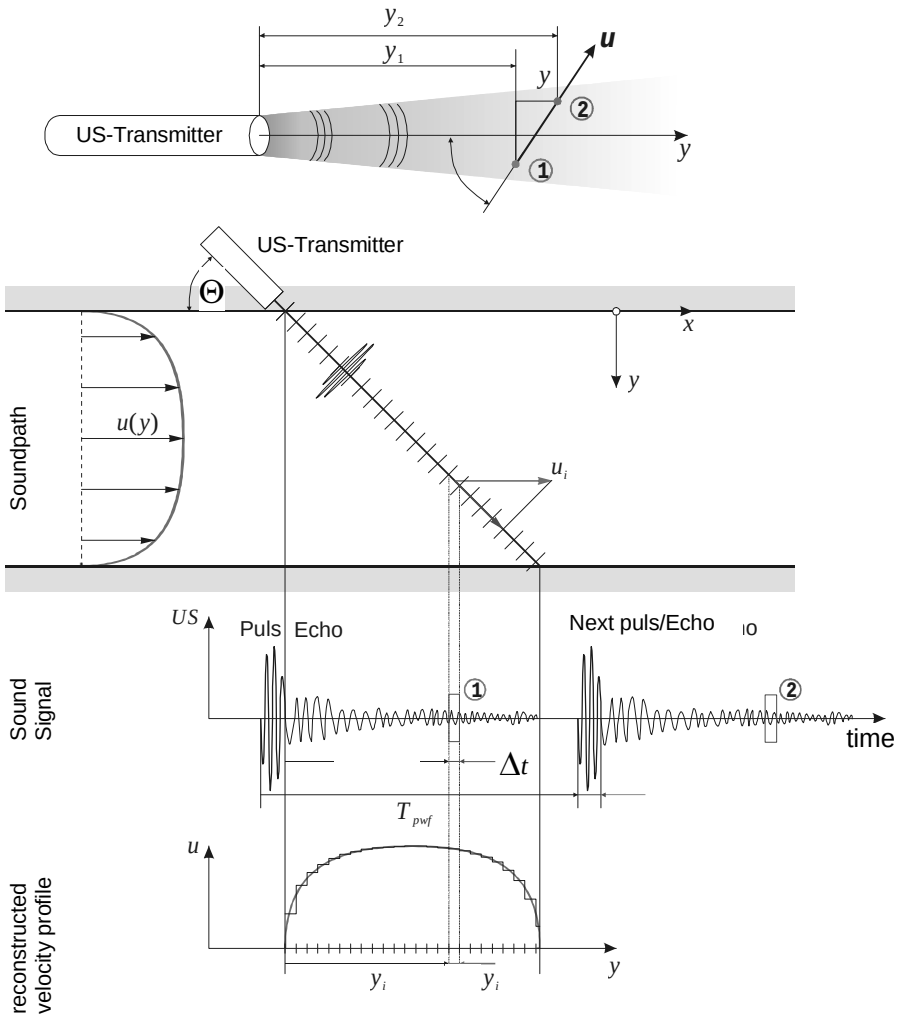

Another feature of the UDV technique is that it allows to measure even deep into the boundary layer close to the duct wall and thus is able to measure velocities only a few microns away from the wall. For this purpose wall correction functions have to be applied, which account for the fact that a part of the measurement volume is located within the wall. In order to get the correct velocity contribution from the fluid domain only echoes from the fluid region are sensed. In a next step the mass centre of the fluid/wall interval is calculated. The deviation of the mass centre of the fluid/wall interval from the distance centre yields a displacement of acquisition point. A detailed description of this procedure may be taken from [Wunderlich, *et al.*, 2000], [Nowak, 2002] or [Lefhalm, 2004].

The measurements of the velocity profiles within the turbulent boundary layer of an annular duct performed by [Lefhalm, 2004], which are shown in Figure 11.4.2(a) illustrate that by means of correction functions the velocity can be acquired. The measured velocities coincide with the literature data of [Reichhardt, 1951] almost perfectly. The deviations found are less than 5%. Moreover, it was possible to measure into the viscous sublayer up to values of $y^+ \approx 3$. In his experimental configuration this corresponded to a wall distance of 46 µm. Also the measurement of the turbulent fluctuations within the boundary layer are possible using the wall correction procedure. Only for $y^+ < 10$ the RMS resolution rapidly dropped.

Figure 11.4.2. a) Measured turbulent velocity profiles in the boundary layer in an annular duct of ∅ = 60 mm at *Re* = 8.1.104 and comparison with [Reichardt, 1951]. b) Comparison of the velocity fluctuations (RMS) with [Durst, *et al.*, 1996].

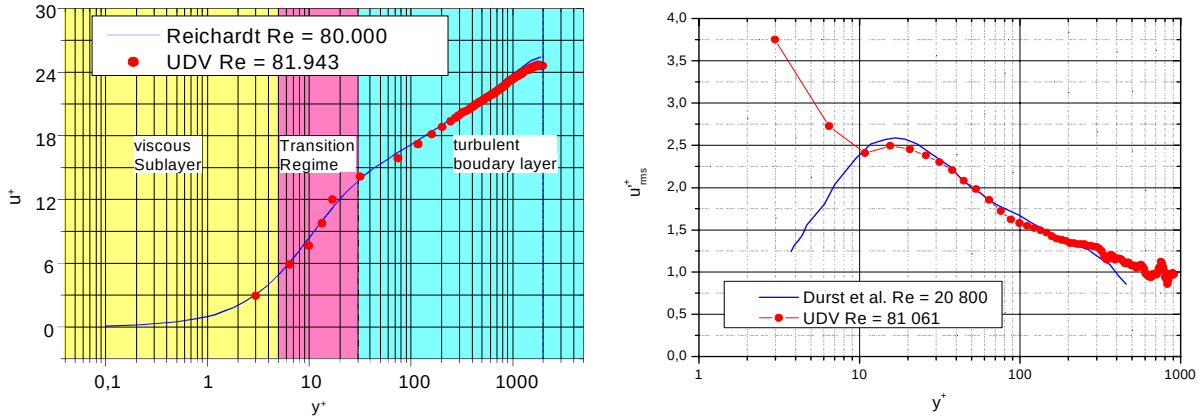

From the procedure explained above it is clear that numerous effects contribute to the acquisition of a proper signal and in fact about 100 parameters are necessary to define the measurement process. The enormous sound speed of heavy liquid metals like PbBi requires extremely fast acquisition and data processing systems to obtain reliable velocity information. Besides these quite sophisticated demands on the data transmission recording and processing units [which are depicted in Figure 11.4.3(d)] several constraints regarding the environmental conditions have to be fulfilled. One of the most crucial problems is the elevated temperature of more than 200°C in typical liquid metal applications, which can not be sustained by commercially available Bariumtitanat sensors ($BaTiO_3$). Thus, wave guides have been developed to decouple the temperature from the sensor. Such an integrated probe consisting of a wave guide and a sensor is shown in photograph 11.4.5(b). It was initially developed by the Forschungszentrum Rossendorf and is in principle applicable to liquid metal temperatures up to 620°C, see [Eckert, *et al.*, 2003]. Secondly, an acoustic coupling of the sensor and the fluid has to be ensured, which in principle means that the probe has to be physically wetted. This is partially achieved by applying a sacrificial nickel layer on the probe surface before inserting it through the fluid. Within the lead-bismuth this nickel layer is dissolved and ensures for a certain time the wetting of the surface. However, after a few days of operation the wetting of the sensor surface gets lost.

Figure 11.4.3. a) Measurement principle of the ultrasound Doppler velocimetry (UDV). (b) Integrated probes consisting of a sensor and a wave guide. (c) Application of a UDV sensor in PbBi in KALLA. (d) Corresponding data acquisition and processing unit for the UDV probe. (e) Measured mean velocity in PbBi as a function of the pipe depth at several power levels of the pump.

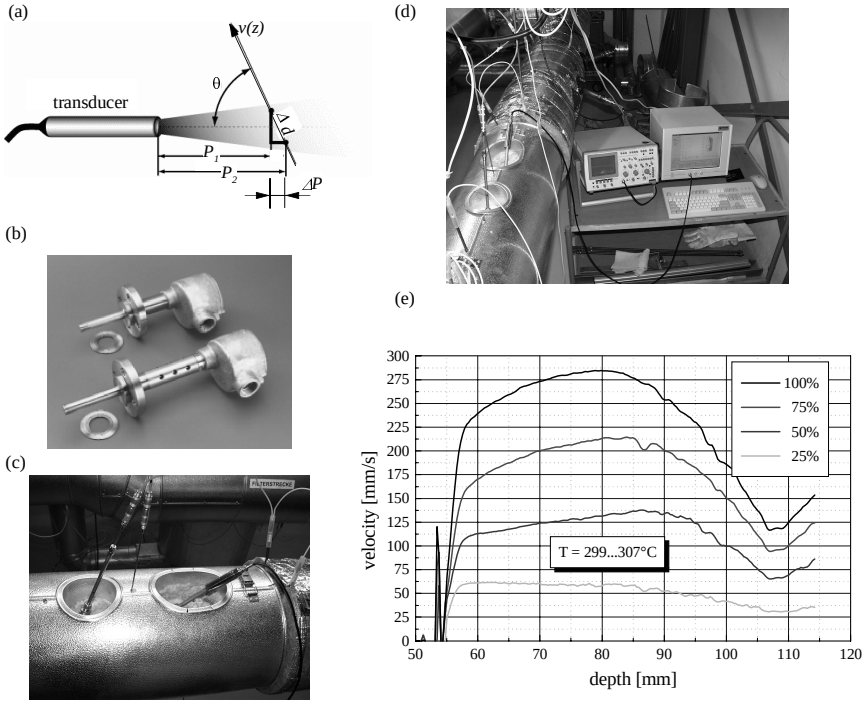

The study of the wetting behaviour of lead bismuth on steel surfaces is a task which as to be solved not only for this application. Another problem is the long term stability of the probe and the flow seeding. By means of conditioning the oxygen content within fluid a certain long term stability of the probe was achieved and a sampling of velocity profiles was successfully performed without any additional artificial flow seeding. Artificial flow seedings with particles of a density like the lead-bismuth are hardly available and stable within the operational conditions typically used.

Nevertheless, it is a question to be clarified in the current programme whether lead bismuth clusters or other impurities are responsible for the generation of the echoes. If temperature gradients are present in the flow being studied, travelling time corrections have to be applied, because the sound speed depends on the square root of the temperature. Thus, either the temperature field of the studied flow has to be known or temperature correlations have to be used. Besides the numerous difficulties using UDV within the THESYS loop KALLA velocity measurements have been successfully performed in a turbulent PbBi pipe flow at temperatures up to 400°C. In Figure 11.4.3(e) the measured mean velocities are shown as a function of the pipe depth for different pump power levels (here given in %). Within this campaign velocity fluctuations of frequencies up to 15 Hz were recorded. If appropriate wall correction functions are used even the velocity distribution in wall near boundary layers can be detected as shown in [Lefhalm, 2004].

11.4.2 Permanent magnetic probes (PMP)

Another method to measure fluid velocity within an electrically conducting fluid is given by permanent magnetic probes. The permanent magnetic probe (PMP) contains a miniaturised permanent

magnet located perpendicular to the main flow. The magnet is encapsulated within a steel tube. The PMP probe allows to measure simultaneously the velocity and the temperature similar like the combined Pitot tube presented in § 11.4.1. The turbulent heat fluxes can be determined from the cross-correlation of both signals – temperature and velocity fluctuations.

Figure 11.4.4. (a) Photograph of a miniaturised PMP probe with thermocouples from Kapulla (2000). b) Side and top view of the arrangement of the thermocouples within a PMP probe.

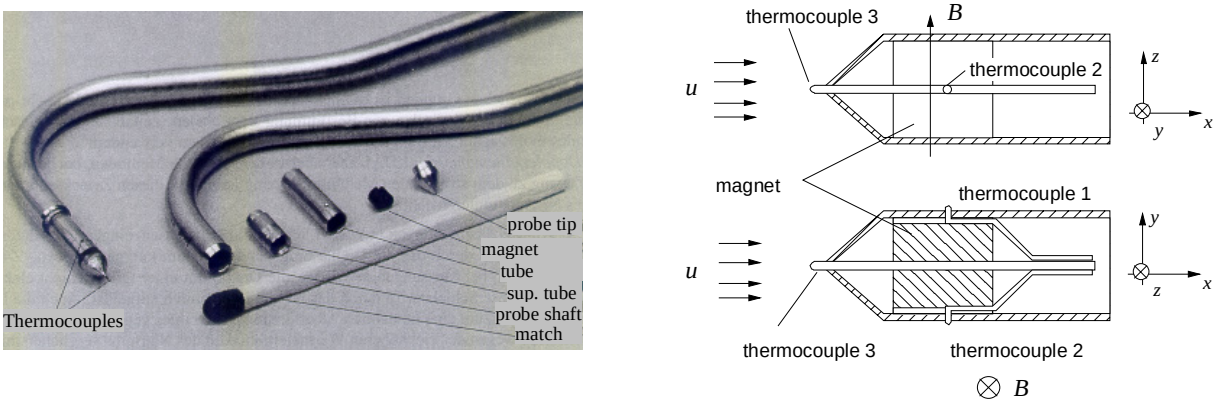

(a) (b)

The PMP probe signal is obtained as low ohmic electric potential $\Delta\phi$ arising from the interaction of the flow field u with the magnetic field B. The simplified Ohms law for moving electric conductors and temporal steady magnetic fields reads to:

$$j = \sigma\left(E_e + E_{th} + u \times B\right) \tag{11.26}$$

where j is the current density, σ the specific electric conductivity of the fluid, E_e the electrostatic field, E_{th} the thermo-electric field, u the integrated velocity of the probe dimension and B the magnetic induction. Generally, there are two main disturbances affecting the induced electric potential. If one takes into account the Maxwell equations [Eqs. (11.27)a-c] and the simplified Ohms law [Eq. (11.26)] one obtains Eq. (11.28).

$$\nabla \times B = \mu\, j; \quad \nabla \times E = 0; \quad E = -\nabla\phi; \quad \nabla \cdot B = 0 \tag{11.27}$$

where μ is the magnetic permeability given by $4\pi \cdot 10^{-7}$ As/Vm.

$$E_{th} = -S\,\nabla T - Q\left(\nabla T \times B\right) \tag{11.28}$$

in which S is the thermoelectric coefficient in V/°K and Q the Nernst-Ettinghausen coefficient in V/(°K·Tesla). Thus, in order to calibrate the probe isothermal measurements are required in a flow with a defined velocity field. A detailed description of this procedure may be taken from [Ricou & Wives, 1982], [Weissenfluh, 1986] and [Kapulla, 2000]. The calibration yields the specific Seebeck coefficient of the individual probe. Additional care has to be taken if external magnetic fields are present in the domain of interest as, e.g. near to electromagnetic pumps or close to DC electromagnetic flow meters. Then an even more complicated effort has to be spent in order to determine the coefficients of the probe. The methodology necessary in this case is exhaustively elaborated in the work of [Ricou & Vives, 1982] and more precise in [Müller, *et al*., 2005].

In the absence of external magnetic fields the PMP probe allows to detect liquid metal velocities in the range from 0-10m/s with an extreme high sensitivity of about 1 mm/s as the experimental works of [Horanyi & Krebs, 1988], [Knebel & Krebs, 1994], [Ricou & Vives, 1982] and [Weissenfluh & Sigg, 1988] document. The sensitivity and the velocity range is not restricted and scopes several decades, which is not possible with other techniques. Generally this technique is applicable up to temperatures of 720°C as the paper by [Ricou & Vives, 1982] shows with measurements in mercury, aluminium, tin, zinc and some alkali metals. The upper limit of the temperature is given by the Curie temperature of the magnet, which is e.g. for nickel-based permanent magnets about 860°C, see e.g. [Eringen, 1980]. Due to responses that are steady, instantaneous and proportional to the velocity of the liquid metal flow high temporal resolutions can be resolved, which is necessary for the study of turbulent flows.

Although it is an intrusive method modern fabrication technologies allows to miniaturise the PMP probe down to diameters less than 2 to 3 millimetres and thus to minimise the impact of the probe an the flow.

One of the most crucial problems of the PMP is the wetting behaviour in the sense of an electrochemical wetting without any contact resistance between the fluid and the probe. Regarding the alkali metals this is not a problem. However, lead and its alloys show a poor electrochemical wetting behaviour of steel surfaces. Similarly as for the UDV probe the PMP has been plated with nickel or silver as a sacrificial layer, which is dissolved immediately by the lead bismuth in order to ensure a proper wetting of the sensor. Nevertheless, after two weeks exposure of the probe to lead bismuth in the composition $Pb^{45}Bi^{55}$ at 400°C the wetting got lost even in an oxygen controlled atmosphere. Also within a reducing atmosphere by means of hydrogen input into the loop the wetting of the probe could not be recovered again, see [Knebel, *et al*., 2003]. This wetting problem is an issue which is not fully understood currently and requires a detailed investigation in order to develop HLM adapted sensors.

11.4.3 Reaction probes (RP)

Especially in steel and aluminium casting or in molten salts where the liquid is highly corrosive reaction probes are used, which are based on the measuring of the force exerted on a submerged body by the flowing liquid. The submerged bodies used in different studies could be discs, plates or spheres. The operation principle of a reaction probe sensor is akin that of a Pitot tube, in that the device responds to the stagnation pressure developed when the fluid impacts the disc. The flow velocity u can be easily calculated using Bernoulli's equation:

$$u = \sqrt{\frac{2F}{A}} \tag{11.29}$$

where F is the force on the disc and A its area. A sketch of such a reaction probe is shown in Figure 11.4.6(a). Here the flow faces the disc and the connected wire compresses a spring. By measuring the compression using a triangulation method the mean velocity can be calculated. The fluctuations are captured by a strain gauge. Even in this simple set-up the measurements of [Szekely, *et al*., 1977] showed quite sensible and reproducible results. Especially the temporal resolution of the probe was quite fine. Also the disc probe requires a specific calibration procedure and it can be only used in a limited velocity range, due to the secondary flow, which is induced by the disc. Moreover, this simple sensor is only capable to detect one velocity component. But, due to the decoupling of the sensor element from the liquid with its elevated temperatures conventional and reliable technology can be used.

Figure 11.4.6. (a) Disc reaction probe used by [Szekeli, *et al*., 1977].
(b) Drag force reaction probe by [Moore and Hunt, 1982].

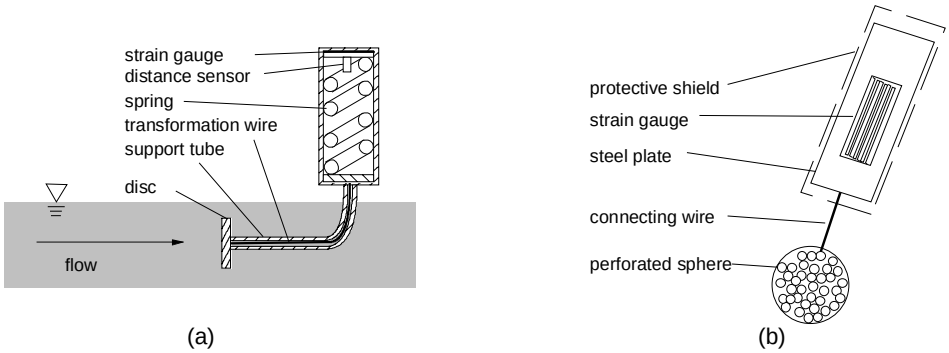

A more sophisticated design of a reaction probe was developed by [Moore & Hunt, 1982], in which the drag forced acting on a sphere is utilised to deduce the velocity. This probe type is depicted in Figure 11.4.6(b). They used a perforated sphere in order to eliminate the vortex shedding effectively and to increase the drag. In their set-up the sphere was made of tanatlum with a diameter of 5 mm. Strain gauges are bonded to either sides of the steel strip which is connected via a 1 mm wire to the sphere.

The signals from the drag reaction probe can measure the drag experienced by the shell and the connecting wire. The mean drag force D integrated over the sphere facing the flow is related to the velocity by:

$$D = \frac{1}{2}\rho A' C_D u^2 \tag{11.30}$$

where ρ is the specific density, A' the cross-sectional area normal to the flow and C_D the drag coefficient, which depends in most cases on the Reynolds number. According to [Schlichting, 1979] the drag coefficient of a sphere, however, is in the Reynolds number range from $2 \cdot 10^3 < Re < 2 \cdot 10^5$ almost constant. In the study performed by Moore & Hunt (1982) this was accomplished by the proper selection of the dimensions of the tantalum sphere. After a calibration in a annular duct flow the probe showed an excellent performance regarding the mean velocity fields, see [El-Kadah & Szekeli, 1984]. Because of the high temporal resolution of the strain gauges a large bandwidth of oscillations of the turbulent flow could be captured so that fast Fourier transforms up to 2-3 kHz could be performed. A comparison of the duct flow data with numerical studies computed by [Evans & Lympany, 1983] demonstrated that the precision achieved with this type of reaction probe was the best compared to similar probe type and matched the model better than 5%.

The initial probe designed by Moore& Hunt was modified by [Moros, *et al*., 1985] in such a way as to measure simultaneously the vertical and one of the horizontal velocity components. A sketch of the [Moros, *et al*., 1985] reaction probe type is shown in Figure 11.4.7.

As all reaction probe types are intrusive methods, their numerous shortcomings include:

a) *Mechanical oscillations*. The oscillation of the suspended probe has to be kept with in an acceptable range so as to resolve the desired velocity value. The sensor must be mechanically decoupled from the piping to avoid miscellaneous readings. The design of the drag element and the connection wire predefines the damping of the sensors and thus its temporal resolution.

b) *The dimension of the drag body*. The dimension of drag body and wire must be chosen in such a way to keep the drag coefficient in the velocity range of interest most insensitive to the

Reynolds number. Otherwise a time consuming calibration over the whole velocity range to be expected in the individual geometrical experimental set-up must be performed in a reference experiment to measure $C_D(Re)$.

c) *Impact of the probe on the flow*. Since the body of the reaction probe induces secondary flows it impacts and modifies the flow to be measured. The pressure waves may have an upstream effect and the secondary flows induced by the drag body may change the flow in such a way that the effect to be measured can be hidden behind the artificial flow modifications. Thus, the flow field in the experimental set-up to be investigated should be identified before the use of reaction probes. +

Aside these shortcomings the reaction probes offer even the opportunity to measure in liquid steel baths with temperatures more than 1500°C, which is currently not accessible with other technologies.

Figure 11.4.7. Modified two component drag reaction probe designed by [Moros, *et al*., 1985]

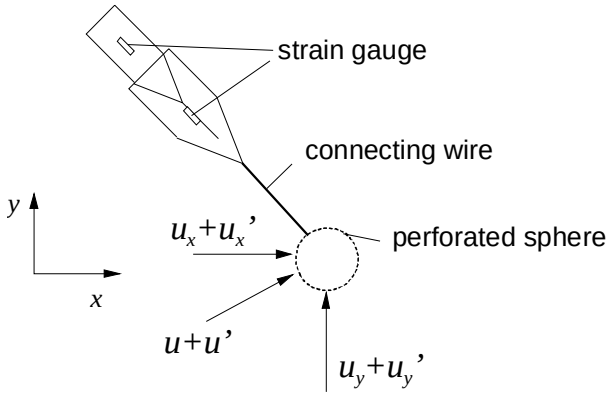

11.4.4 Hot wire anemomentry (HWA)

Quite a lot of problems arise using hot film anemometers in liquid metal flows. The main question is the chemical compatibility of the liquid metal and the hot wire, in which surface tension and heat transfer aspects has to be considered. If alkali or earth alkali metals are used for the loop the compatibility of the wire with the liquid may become a killing issue, due to the low electrochemical potent of these liquids. Up to now only silicium oxide plated wires of hot wire anemometers shows no degradation in connection with NaK at temperatures up to 100°C, see [Reed, *et al*., 1986, 1987, 1989]. [Murthy & Szekely, 1983] went with Woods metal up 120°C, but nearly all other hot film measurements were restricted to mercury, gallium or other low melting liquid metals or alloys like in the papers by [Malcolm, 1969], [Hill & Sleicher, 1971], [Platnieks, 1971], [Sleicher & Lim, 1975]. Only one example of an application reaching a temperature of 250°C in $Na^{44}K^{56}$ was found which was performed by [Hochreiter & Sesonske, 1969] and one for sodium up to 300°C by [Platnieks & Ulmann, 1984].

Surface effects which occur due to impurities in the liquid metal lead to reaction and change the characteristics of the probe. Only by an appropriate cleaning of the probe such an effect can be avoided. Another issue related to MHD has to be considered using hot wire probes. The hot wire probe measures in principle the heat transfer from the wire. The heat transfer in a MHD flow however is different to that of an ordinary hydrodynamic flow. The measurements of [Lykoudis & Dunn, 1973] show that the Nusselt number *Nu* strongly depends on the Hartmann number *M* or *Ha* [see Eq. (2.6)] and the hydraulic Reynolds number (see Figure 11.4.8). Thus, a calibration measurement of the hot wire anemometer for each measured magnetic field strength has to be performed.

Figure 11.4.8. Dependence of the Nusselt number *Nu* on the Reynolds number *Re* and the Hartmann number *M* (or *Ha*) in a hot wire calibration measurement performed by [Lykoudis & Dunn, 1973]

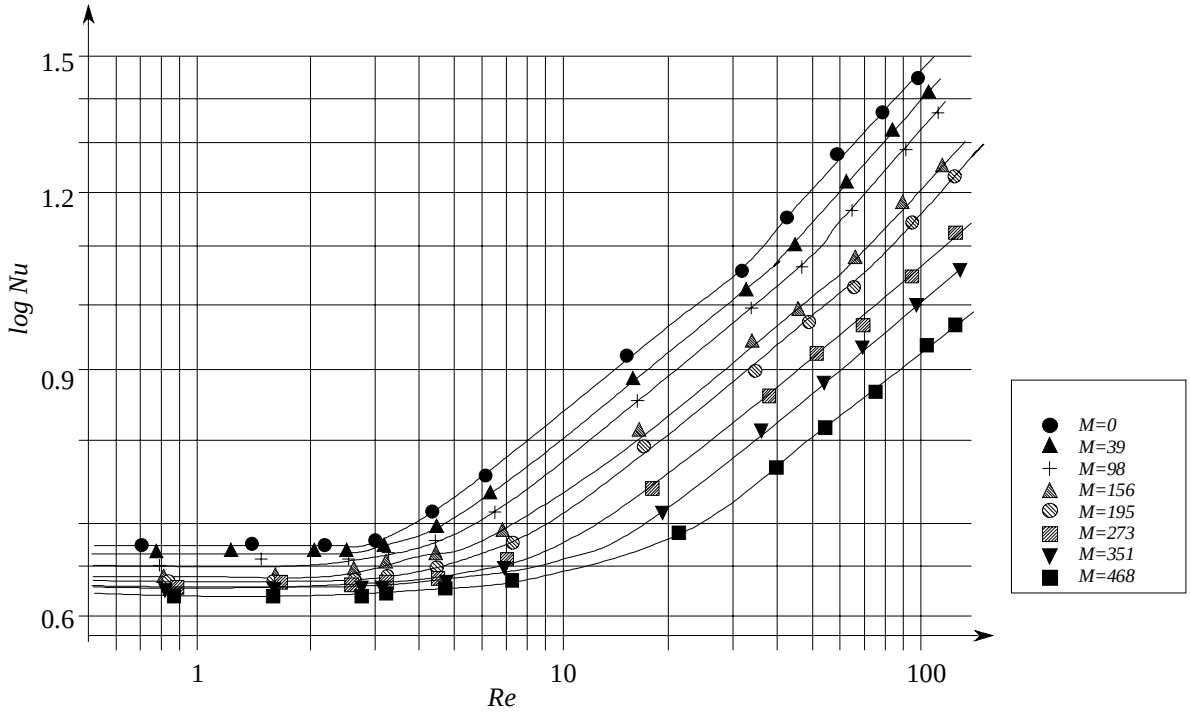

In contrary to the potential probe the hot wire anemometer is not capable to detect the direction of the flow, because it measures the integral heat transfer at the wire, see e.g. [Hill & Sleicher, 1971]. So using this probe type correlation measurements, which are necessary to determine vortex structures in turbulent flows can not be performed. Another disadvantage of the hot film probes originates from the low Prandtl numbers of the liquid metal leading to a drastic reduction of the resolution of the probe, because the conductive heat transfer in liquid metals is favoured compared to the convective one. Hot wire probes type exhibit an interesting feature serving a crucial advantage compared to reaction probes and PMP sensors. They are rather small, the wires are only some microns thin which affects the flow hardly but the probe is on the other side not very robust. A schematic drawing of a HWA probe is shown in Figure 11.4.9.

Figure 11.4.9. Schematical drawing of hot wire anemometer

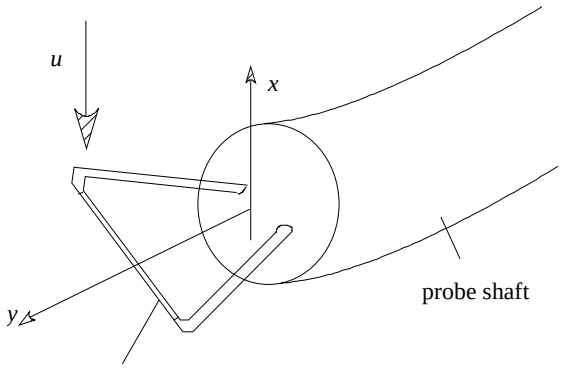

The high thermal conductivity of liquid metals plus the necessity of keeping a nearly constant temperature makes the use of HWA probes difficult. Another problem is a drift that may occur in the signal because of the disposition of oxide in metals that are easily oxidised by air. In [Szekeli, *et al*., 1988] it is reported that despite protective blankets of inert gas it is common to encounter drift in the signal due to fouling of the probe by oxide in both mercury and Woods metal.

Another issue related to HWA probes is that the sensitivity of the probe is inhibited at low Peclet numbers. Here, even at quite low flow frequency oscillations the low Prandtl number of the liquid metals yield to a reduction of the signal, see [Malcolm & Verma, 1981]. The Peclet number is defined by the product of the Reynolds number with the Prandtl number in the way:

$$Pe = Re \cdot Pr \quad \text{with} \quad Pr = \frac{\nu \rho c_p}{\lambda} \tag{11.31}$$

where ν is the kinematic viscosity in [m^2/s], ρ the specific density in [kg/m^3], c_p the heat capacity in [J/(kg K)] and λ the heat conductivity in [W/(m K)]. For the observed decreasing sensitivity at low Peclet numbers two effects are responsible:

a) The amplitude of fluctuation is attenuated and the degree of attenuation depends upon a non-dimensional quantity $\kappa\, f/u^2$ in the range of Peclet numbers up to 10, where κ is the thermal diffusivity given by $\kappa = \lambda/(\rho\, c_p)$, f the frequency of the fluctuations and u the mean flow velocity. The amplitude is attenuated by 10% and 90% at $\kappa\, f/u^2$ values of 0.02 and 4.0 respectively.

b) There is a phase lag in the HWA signal with respect to the true velocity of the fluctuation which is somewhat the same as that in potential flow at low frequencies, but it is considerably higher than that in potential flow at higher frequencies. The measured lag does not level off asymptotically at high frequencies.

11.4.5 Transition time methods

11.4.5.1 Temperature pulse method

The temperature pulse method is based on the measurement of the decay time of temperature pulses in a medium. The fluid velocity can be calculated from the propagation time of the temperature pulse. The temperature waves are produced by a miniaturised heater, which is surrounded in defined positions by thermocouples. The propagation of a temperature pulse in a fluid at rest is shown in Figure 11.4.10(a). A drawing of the measurement instrument is shown in Figure 11.4.10(b). A problem may arise with this measurement method in fluids with extremely low Prandtl numbers like in liquid metals, because there a temperature pulse diffuses rather fast. Therefore, high temperature pulses have to be brought in the liquid metal in order to enable a resolvable measurement of temperature changes in small distances from the miniaturised heater. A determination of the velocity vector is only possible if a grid of thermocouples is placed next to the heater. Such a grid affects the flow non-negligibly, however. A second aspect which should be also considered is the choice of the thermocouples for this method, see therefore Section 11.6. [Casal & Arnold, 1988] demonstrated the viability of this measurement method in water and also in liquid metals. Nevertheless, the resolution of this method in liquid metals is rather poor around ±25% and the technical effort high.

Figure 11.4.10. (a) Temperature propagation of a temperature pulse as a function of the time *t*. (b) Schematic drawing of a temperature pulse measurement instrument to detect velocity vectors in sodium-potassium $Na^{22}K^{78}$ by [Casal & Arnold, 1988].

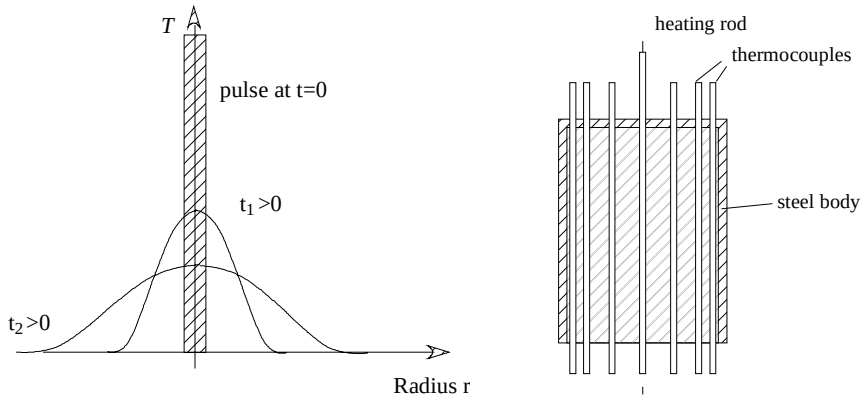

11.4.5.2 Tracer studies

Tracer studies were initially developed for velocity and diffusivity measurements in molten salts. In using this technique a small amount of tracers is introduced at a defined time *t* at a discrete point of the flow field, while downstream the liquid is sampled periodically. A simple representation of this technique is sketched in Figure 11.4.11(a). If the integrity of the tracer is ensured for the duration of the experiment and assuming isotropic conditions the tracer concentration *C* in a radial co-ordinate system is given by Eq. (11.32).

$$\frac{\partial C}{\partial t} = \frac{D_t}{r^2}\frac{\partial}{\partial r}\left(r^2\frac{\partial C}{\partial r}\right) \tag{11.32}$$

where D_t is the molecular diffusivity in case laminar flows or the effective diffusivity considering turbulent flows. In principle the tracer studies are a coupled initial and boundary problem so that for assuming the following conditions:

$$C = 0 \quad \text{at} \quad r \to \infty; \quad C \text{ finite for } t > 0, \text{ at } t = 0 \quad C = \delta(t = 0) \tag{11.33}$$

The solution of Eq. (11.32) under the conditions (11.34) is given by:

$$C = \frac{A}{2\sqrt{\pi D_t t^3}}\exp\left(-\frac{r^2}{4D_t t}\right) \tag{11.34}$$

where *A* is a constant. However, for a moving co-ordinate system the location r_{Sensor} of the sampling sensor is given by $r_{Sensor} = d - u \cdot t$, where *u* is the probe flow velocity so that Eq. (11.34) mutates to:

$$C = \frac{A}{2\sqrt{\pi D_t t^3}}\exp\left(-\frac{(d - u\cdot t)^2}{4D_t t}\right) \tag{11.35}$$

By fitting the measured concentration curve [Figure 11.4.11(b)] to Eq. (11.35) the quantities *u* and D_t can be determined. There are problems arising from the above interpretation with the path pursued

Figure 11.4.11. (a) Schematic representation of the tracer technique. (b) Tracer concentration at a downstream sampling point as a function of time.

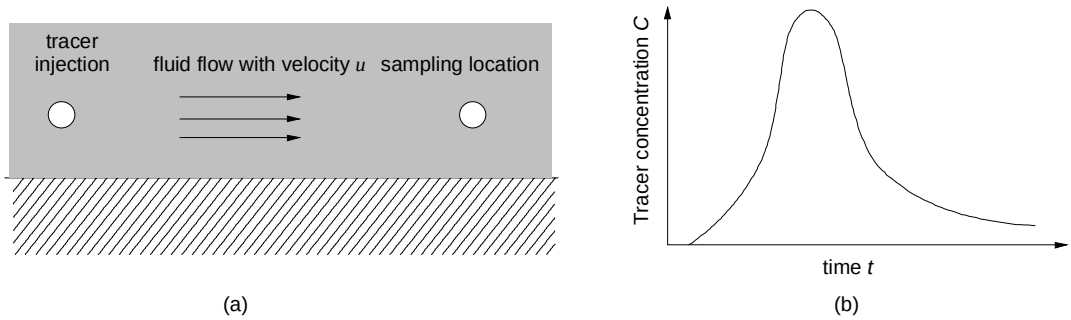

by the fluid between the point where the tracer was introduced and the sampling point, the tracer decay, while the velocities measured in this way are average values over a relatively large region. Velocity and diffusivity measurements are reported by [Grjotheim, *et al*., 1970, 1971] and [Berge, *et al*., 1973] for aluminium reduction cells. Tracers may not only be oxides of the fluid investigated but also radionuclides can be used, as suggested by [Szekely, 1964] and [Szekely & Chang, 1977a,b].

The tracer methods allow to measure even in steel and iron bath but its accuracy is rather poor and a lot of pre-knowledge of the velocity in the domain of interest is required. In all cases measurements and theoretical predictions agreed within a factor of ±50%.

11.4.5.3 Dissolution studies

Measurements of metal velocities from the mass lost of iron rods introduced in liquid aluminium were initially developed by [Johnson, 1978] and subsequently improved [Taberaux & Hester, 1984]. The latter derived calibration curves correlating mass loss with liquid metal velocity by measuring the iron rod mass lost in a stirred tank using a load cell. Here the following correlations are used:

$$Sh = A + B \cdot Re^n Sc^m \tag{11.36}$$

where *Sh* is the Sherwood number, *Re* the Reynolds number, *Sc* the Schmidt number and *A*, *B*, *n* and *m* are constants. The characteristic numbers are defined as:

$$Sh = \frac{\beta \cdot d}{D_t}, Re = \frac{u \cdot d}{\nu} \text{ and } Sc = \frac{\nu}{D_t} \tag{11.37}$$

β is the mass transfer coefficient and is not a material property. It depends on the concentration, velocity and temperature field and has the dimension of the velocity. The analogue of the Sherwood number in heat transfer problems is the Nusselt number. Thus, the Sherwood number is often called the Nusselt number of the mass transfer.

Due to the dependence of the mass transfer coefficient β on flow, concentration and temperature field a sophisticated calibration procedure is required which is described in detail by [Bradley, *et al*., 1984]. Besides aluminium this methods has been also applied to steel melts by [El Kaddah, *et al*., 1984]. By determining the extend of dissolution for specific time intervals, the local mass transfer coefficients are calculated and compared to the predicted ones using both laminar [Eq. (11.38)a] and turbulent correlations [Eq. (11.38)b], which were found experimentally by [Grevet, *et al*., 1982] and [Szekely, *et al*., 1984].

$$Sh = 0.683 \cdot Re^{0.466} \cdot Sc^{\frac{1}{3}} \quad ; Sh = 0.338 \cdot \left(Re \cdot Tu\right)^{0.8} \cdot Sc^{\frac{1}{3}} \qquad (11.38)\ \text{a,b}$$

Herein, *Tu* is the turbulence intensity. *Tu* and *Re* were an input to the above named correlations from a numerical simulation. A clear analysis of the relations (4.38)a,b rapidly exhibits that both of them has an error of about ±25%, see e.g. [Jischa, 1982].

11.4.6 Neutron radiography

The attenuation of neutron rays for heavy liquid metals is small. Therefore, the flow in these liquid metals can be seen by neutron rays. An initial method to visualise the flow a liquid metal by tracer and dye injection using the neutron radiography has been made by [Takenada, *et al*., 1994]. They used an accelerator-based real-time neutron radiography. In these first studies a fluorinated hydrocarbon which is transparent for neutrons was used. For the use in heavy liquid metals, however particles owing a similar density are required. [Takenada, *et al*., 1996] report that for the use in eutectic lead-bismuth gold cadmium ($AuCd_3$) intermetallic alloy particles were successfully applied, since they wet well by this liquid and its density is close to that of the metal. The flow can be visualised by watching the movement of the individual particles by real-time radiography and a digital image post-processing procedure.

The image post-processing method used is the same as for the particle image velocimetry (PIV), in which the acquired images of the moving tracers are obtained by subtracting the time averaged image from the original one. With two consecutive images of the moving tracer, pattern matching is carried out at each point to obtain the flow vector by calculating the spatial correlations. Since the tracers are much larger than one image element, i.e. that of noises in the experiment, the image of the tracers can be easily obtained by using a spatial filter in the image processing program. Because the noise is random and has no correlations, the noise does not affect the spatial correlation of the tracer signals. The spatial correlation function $\Psi(u,v)$ between the data of two consecutive images $f_1(x,y)$ and $f_2(x,y)$ is defined as:

$$\Psi(u,v) = \iint f_1\left(x-u, y-v\right) \cdot f_2\left(x,y\right) \quad dx\,dy \qquad (11.39)$$

With this method Takenada, *et al*. achieved temporal resolution of 30 Hz. The most probable movement of the tracers pattern is indicated by (u,v) at the peak of the function and the flow vector can be determined. Since the noises are random, the spatial correlation method is applicable to the images where the tracer and the noise can not be divided by any spatial filters. Reasonable vector fields with an uncertainty of less than 10% could be obtained in lead-bismuth eutectics, the thickness of which is 25 mm, i.e. the attenuation rate is about $1/e$, by the spatial correlation method even if the tracer sizes were the same order as those of the image noises. Since the attenuation coefficients of sodium and sodium-potassium are much smaller than that of lead-bismuth, flow in thick liquid metal layers of alkali metals can be visualised.

11.4.7 Fibre mechanics systems (FMS)

The measuring apparatus of FMS is based like the reaction probe on simple mechanics in the way that a mechanical sensor, which is in direct contact with the hot liquid, is mounted rigidly on an optical system used to acquire the measuring data. The thin tip of the probe shaped by a special glass manufacturing technique in form of a cone acts as sensitive part. A small glass rod, the so-called pointer having a length of order 10-50 mm, depending on the desired sensitivity of the probe is positioned

inside this glass tube and connected with the sensor tip ideally only at the front point. Technically it is bonded mostly over a length of 1 mm. The initial position of the free end of the pointer is approximately located in the centre of the glass tube. In presence of a fluid motion around the tip the sensor reacts in form of an elastic deformation as shown in Figure 11.4.12(a). Consequently, at the opposite end a resulting spatial shift of the pointer can be observed by optical means in the opposite direction to the displacement of the sensor tip. The deflection of the tip is a function of the fluid velocity at the tip. The evaluation of the direction and the amplitude of the pointer displacement allow to determine the two velocity components perpendicular to the sensor. Therefore, an endoscope combined with a lens system connected to a CCD array is used to observe the pointer image. By digitalisation and analysing of the images using a frame grabber the informations are stored.

Figure 11.4.12. (a) Measurement principle of a mechano-optical probe. (b) Stereo-microscopic photograph of a mechano-optical probe with an attached sphere by [Eckert, *et al*., 2003]. (c) Mechanic model of the displacement of the probe tip by the flow to evaluate the flow velocity.

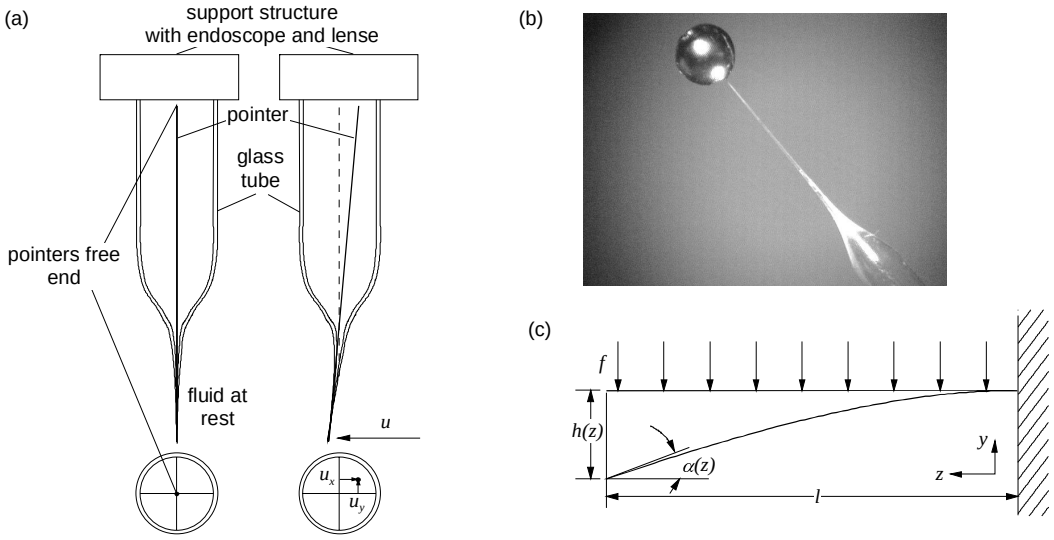

Initially such systems were invented by [Zhilin, *et al*., 1987, 1989] and [Boyarevich, *et al*., 1990]. But, a higher resolution and a successful miniaturisation and implementation to higher melting point liquids were reached by [Eckert, *et al*., 2000]. They managed to fabricate probe tips with diameters around 50 μm and embedded pointers with a length of 30-40 mm. The bonding of tip and sensor was only 1 mm, which represents the integration length scale of the sensor in the flow.

A critical point is the choice of the sensor material. The material has to obey Hooks law and must be temperature and chemical resistant to the fluid of interest, e.g. boronsilicate glass is favourable for applications up to 350°C in sodium, gallium but also InGaSn, SnPb, SnBi or PbBi. It exhibits a constant elastic modulus E up to 400°C, see [Scholze, 1965] and is even stable against sodium (compare [Eckert, 1997]). Moreover, the fabrication technology and handling of this glass type is simple. For higher temperatures quartz-glass tips can be used, which operate up to temperature of 800°C, see [Eckert, *et al*., 2003].

In order to calculate the pointer displacement the sensor tip is considered as a mechanical element in the configuration shown in Figure 11.4.12(c). A flow around the tube causes a more or less constant force per unit length $f = \rho\, r\, u^{2} C_W$ leading to a deformation of the sensor, where r is the radius of the tube and l its length, r the specific fluid density, u the velocity and C_W the drag coefficient. The displacement of the tube from the equilibrium position is described by the parameter $h(z)$.

Assuming that the tube is bent by a torque M_x in x-direction the displacement is expected parallel to the y-direction. The original x-z-sections are not deformed and remain transverse to the y-axis. If we consider only small displacements $h(z)$ and the wall thickness δ is small compared to r then the moment of inertia transverse to the tube I_x can be approximated by $I_x = \pi \cdot \delta \cdot r^3$. Thus, one obtains an ordinary differential equation for the force f in the form:

$$f = \frac{d^2 M_x(z)}{dz^2} = E \cdot I_x \cdot \frac{d^4 h(z)}{dz^4} \tag{11.40}$$

where the elastic modulus E and the moment of inertia in x-direction I_x are assumed to be constant. Imposing the boundary conditions $h = (dh/dz) = 0$ at $z = 0$ and $M_x = (dM_x/dz) = 0$ at $z = l$ one obtains:

$$h(z = l) = \frac{C_W \rho u^2 l^4}{8 E \pi r^2 \delta} \tag{11.41}$$

According to the drag curve for a flow around a cylinder, see [Brauer, 1971] the C_W value can be considered as constant in a wide range so that a parabolic dependence of the measured quantity $h(z)$ can be expected. A significant influence of the probe geometry in terms of r, l and δ becomes obvious, which allows a defined adjustment of the sensor with respect to the desired velocity range.

An enhancement of the sensitivity can be obtained by attaching a sphere to the sensor tip, see also Section 11.4.3. If the radius of the sphere r_s is significantly larger than the fibre shaft the bending is mainly governed by the sphere at the end of the fibre. Thus, the boundary conditions applied to Eq. (11.40) are $h = (dh/dz) = 0$ at $z = 0$ and $M_x = 0$, $(dM_x/dz) = -F_s$ at $z = l$, where F_s is the force acting on the sphere, which yields:

$$h(z = l) = \frac{C_D \rho r_s^2 u^2 l^3}{6 E \pi r^3 \delta} \quad \text{with} \quad F_s = \frac{\pi}{2} C_D \rho r_s^2 u^2 \tag{11.42}$$

Since the drag coefficient of a sphere C_D is even less sensitive to the Reynolds number than that of the tube, i.e. it is almost constant for $10^2 < Re < 3 \cdot 10^5$ an increase of the sensitivity of a factor three can be attained. Such a sensor type is shown in Figure 11.4.12(b).

To extract the actual velocity from the measurements each sensor tip has to be calibrated separately. Due to the dependence of the pointer displacement on the fluid density the calibration procedure has to be performed with the same liquid as the later on conducted experiment.

11.4.8 Pitot and Prandtl tubes

11.4.8.1 General features and application

The measurement principle of Pitot and Prandtl tubes was already explained in Section 11.2.3.2 in the context of the flow rate measurement. Thus only some remarks on the operational experience are made. Via miniaturisation of the sensors local velocities and if thermocouples are embedded heat fluxes can be measured. The resolution of this local measurement technique is given by the resolution of the used pressure gauges.

The THESYS loop of KALLA, which uses Kulite pressure transducers, could determine the local velocity with an accuracy of 5 mm/s. The Pitot tube used there is sketched in Figure 11.4.13(a) and is

capable to resolve a pressure of 12.5 Pascal. Higher resolutions may be obtained by more sensitive sensors. A typical turbulent velocity profile and the corresponding temperature profile which has been measured by means of a combined Pitot tube with two thermocouples in a circular tube at a temperature of 300°C with a Pitot tube is depicted in Figure 11.4.13(b).

Figure 11.4.13. (a) In KALLA developed Pitot tube with small thermocouples to measure local velocities *u*(*z*) and temperatures *T*(*z*) and their fluctuations. (b) Measured mean velocity and temperature in a turbulent lead bismuth pipe flow at 300°C with the Pitot tube depicted in (a).

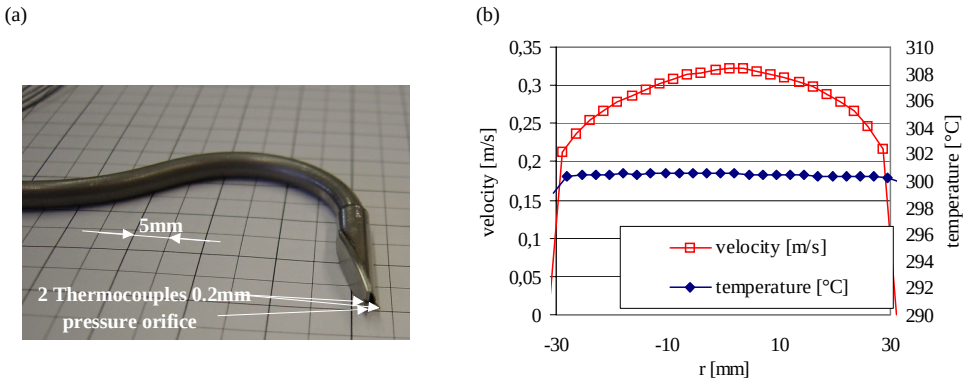

The smallest spatial dimension over which the velocity is integrated, is given by the size of the orifice of the Pitot tube. As the surface tension of heavy liquid metals like lead or lead-bismuth is quite large and of order O(10^2 mN/m) the pressure difference required to fill the tubes orifices significantly increases with the degree of miniaturisation. A reliably operating Pitot tube system is only obtained for a gas free tube. Thus, drain tubs to ensure a complete filling of the sensor are required. Due to the large Reynolds numbers appearing in HLM flows the boundary layers appearing there are relatively thin and thus only near to the region towards the main flow resolvable with Pitot tubes. An experimental example of the flow field measurement using a Pitot tube near a heated rod in an annular cavity is shown in Figure 11.4.14. In order to acquire the flow distribution within the boundary non-intrusive methods are required as the ultrasound Doppler velocimetry (UDV).

Figure 11.4.14. Measured mean velocity u_z [m/s] near a rod in an annular cavity as a function of the radius *r* [mm] at T_{in} = 300°C for different Reynolds numbers *Re* at *z*/*d* = 13.9 from [Lefhalm, *et al*., 2004]

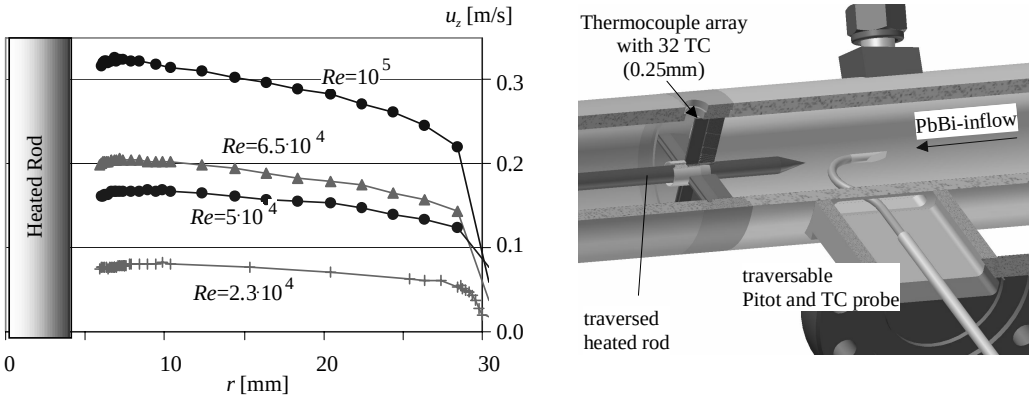

In order to obtain accurate mean velocity profiles using a Pitot tube many corrections need to be made to account for the effects of viscosity, turbulence, velocity gradients and the presence of a wall. Recent measurements by [Zagarola and Smits, 1998] in a turbulent pipe flow in a Reynolds number regime from $3.1 \cdot 10^3 < Re < 3 \cdot 5 \cdot 10^7$ have raised questions regarding the accuracy and applicability of the current correction methods, which are summarised in the work of [Perry, *et al*., 2001]. In pipe flows with Reynolds numbers around 10^5-10^6, which easily appear in heavy liquid metal applications, there is a difference of greater 5% in the slope of the logarithmic region between data with and without wall correction [McKeon, *et al*., 2003].

11.4.8.2 Viscous corrections for Pitot tubes

Viscous corrections are important if the Reynolds number based on the probe diameter, Re_d, falls below 10^3. This is one of the most important – and most often forgotten – corrections while using Pitot tubes. If the Reynolds number Re_d is larger than 10^2 the viscous correction is in the range of 0.5% [Zagarola, 1996]; for smaller values of Re_d, however, it can reach several %. Using the pipe flow results from [Barker, 1922], [Reichardt, 1951], [Hurd, *et al*., 1953], authors [MacMillan, 1954, 1956], [Chue, 1975] and [Zagarola, 1996] suggested that for $Re_d > 30$ the following relation should be applied:

$$C_P = 1 + \frac{10}{(\mathrm{Re}_d)^{3/2}} \tag{11.43}$$

where C_P is the measured pressure coefficient. Due to the numerous experimental data Eq. (11.43) can be considered as a true representation of the viscous effects on the Pitot tube data.

11.4.8.3 Turbulence correction for Pitot tubes

The effects of turbulence on the Pitot tube reading are two-fold. First, the velocity fluctuations increase the measured pressure. Second, when measurements are taken using a pressure tapping at the wall to measure the static pressure, the radial gradient in static pressure due to velocity fluctuations must be taken into account. The combined effect of these two phenomena is given by [Ozarapoglu, 1972] by:

$$\frac{u - u_m}{u_m} = -\frac{\overline{u^2} - (1 + K_t)\overline{v^2} + (1 + K_t)\overline{w^2}}{2u_m^2} \tag{11.44}$$

where u is the true mean velocity, u_m is the measured mean velocity and $\overline{u^2}$, $\overline{v^2}$ and $\overline{w^2}$ are the mean square velocity fluctuations in the streamwise, radial and circumferential directions. K_t is a coefficient that accounts for the directional sensitivity of the Pitot probe and is for circular taps around 0.3. While measuring close to the wall [Dickinson, 1975] suggested that for $y^+ > 50$ Eq. (11.44) could be simplified in the way:

$$\frac{u - u_m}{u_m} = -\frac{\overline{u^2}}{2u_m^2} \tag{11.45}$$

accepting errors of ±0.5%. Here, the dimensionless wall distance y^+ is defined as:

$$y^+ = \frac{\Delta y \cdot u_\tau}{\nu} \quad \text{where} \quad u_\tau = \sqrt{\frac{\tau_\omega}{\rho}} \tag{11.46}$$

u_τ is the friction velocity, Δy is the wall normal distance from the wall, τ_ω the wall shear stress and ρ und ν the specific fluid density and kinematic viscosity.

11.4.8.4 Velocity gradient correction for Pitot tubes

In a shear flow the presence of the probe deflects the streamlines so that the probe registers a velocity that is higher than the velocity at the geometric centre of the probe. In order to account for this interference effect, which usually dominates all other Pitot tube errors, a correction is made which can be expressed as an error in the measured velocity or as an apparent shift in the probe location. The origin of this error is schematically shown in Figure 11.4.15.

Figure 11.4.15. The effect of a Pitot tube on the streamline pattern; left in a shear flow and right in a uniform flow near a wall without adhesive wetting $u \neq 0$ but $v = 0$

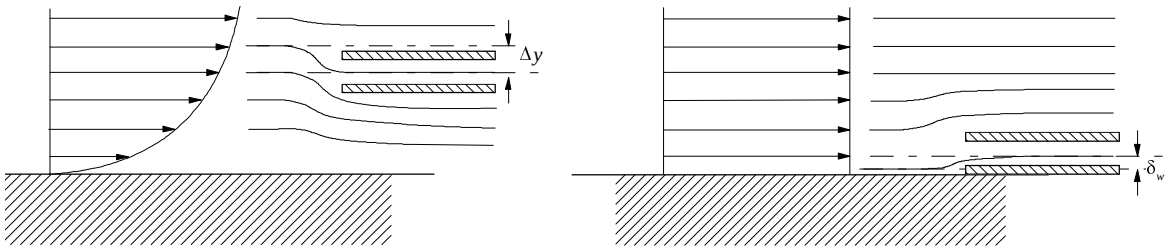

If the velocity gradient across the Pitot tube is small compared to its mean value and additionally if we assume that the mean velocity is a function of y only then one can deduce:

$$\frac{\Delta u}{u(y_c)} = \frac{u(y_c + \Delta y) - u(y_c)}{u(y_c)} = 2\alpha \frac{\Delta y}{d} - \beta \frac{(\Delta y)^2}{d^2} + ... \tag{11.47}$$

where y_c is the position of the centre of the Pitot tube, $u(y_c)$ is the true velocity at y_c, Δy is the correction in the position due to the streamline displacement and the velocity gradients are evaluated at the centre of the probe. d is the diameter of the probe. The coefficients α and β are defined by:

$$\alpha = \frac{d}{2u(y_c)} \left.\frac{du}{dy}\right|_{y=y_c} \quad , \quad \beta = -\frac{1}{2} \frac{d^2}{u(y_c)} \left.\frac{d^2u}{dy^2}\right|_{y=y_c} \tag{11.48}$$

Eq. (11.47) exhibits that the correction in the velocity and the apparent shift of probe position $\Delta y/d$ are directly connected. In fact, the velocity gradient correction is usually implemented by correcting the probe position rather than by correcting the velocity itself. This form is often called the displacement correction and several authors like [MacMillan, 1954], [Livesey, 1956], [Patel, 1965] [Tavoularis & Szymczak, 1989] have suggested that:

$$\frac{\Delta y}{d} = \varepsilon \tag{11.49}$$

where $0.08 < \varepsilon < 0.16$. Other correction correlations for individual applications can be found in the paper by [Chue, 1975] and [Patel, 1965] or [Zagarola & Smits, 1998].

In the presence of a wall, there is an additional mechanism for streamline displacement. Consider a Pitot tube resting on the wall in a uniform flow, as shown in Figure 11.4.15 right. Since it resembles a forward-facing step, it may be expected that the streamlines would be displaced away from the wall, that is towards the region of higher velocity (rather than towards the region of lower velocity as it is in free shear). Therefore, the true correction close to the wall must be some combination of these two effects. Already [MacMillan, 1956] observed this trend and suggested that a wall correction was necessary in addition to the displacement correction for $y/d < 2$. He proposed that this wall correction may be represented by:

$$\frac{\Delta u}{u} = 0.015 \exp\left[-3.5\left(\frac{y}{d} - 0.5\right)\right] \tag{11.50}$$

It should be noted in this context that the MacMillan corrections were not corrected for the effects of turbulence intensity and velocity gradient. In other words, implementing an additional turbulence correction when using the MacMillans method is not appropriate.

11.4.8.5 Displacement correction for Pitot tubes

The displacement correction is another type of velocity gradient correction, which is more accurate. Best results have been obtained by [McKeon, *et al*., 2003] using the following relation:

$$\frac{\Delta y}{d} = 0.15 \cdot \tanh\left(4 \cdot \sqrt{\alpha}\right) \tag{11.51}$$

where α is defined by Eq. (11.48). This form is based on the analysis by [Hall, 1956] and [Lighthill, 1957], who found that the displacement correction for a sphere in a velocity gradient could be expressed by a hyperbolic tangent function of the non-dimensional shear. The constants described by [McKeon, *et al*., 2003] matches experimental data based on the analytical derivation of [Hall, 1956] in such a way that both collapse identically. Note that this type of correction gives zero displacement for zero shear and asymptotes the [MacMillan, 1956] correction for large shear, i.e. $\alpha \rightarrow 1$.

11.4.8.6 Wall correction of Pitot tubes

The wall correction based on the Preston tube data of [Patel, 1965] was made under the condition where the probe is under maximum influence of the wall as well as shear. Where a Preston tube is simply a Pitot tube resting on the wall. If one assumes that the Preston tube reads the true pressure at:

$$y = 0.5 \cdot d\left(1 + \frac{\delta_w}{d}\right) \tag{11.52}$$

then a definition of the wall displacement correction δ_w is obtained. If the form of the velocity profile is known, $\Delta p_0 = \frac{1}{2}\rho \cdot u^2$ may be formulated and substituted in the expression of the logarithmic low for the boundary layer velocity distribution.

Especially for $8 < d^+ < 110$ viscous effects are undoubtedly important, and its known that α changes significantly, so that one can expect that δ_w will vary with d^+. [McKeon, *et al*., 2003] elaborated the following wall corrections applicable for $y/d < 2$:

$$\frac{\delta_w}{d} = \begin{cases} 0.150 \text{ for } d^+ < 8 \\ 0.120 \text{ for } 8 < d^+ < 110 \\ 0.085 \text{ for } 110 < d^+ < 1600 \end{cases} \tag{11.53}$$

11.4.8.7 Comments on displacement and corrections

To evaluate displacement and wall corrections it would be convenient if the true velocity profile was known. Unfortunately, the nature of the true profile is still a source of debate, specifically as to what role geometry and/or Reynolds number play, particularly in the buffer region. To clarify this aspect, experimentally non-intrusive methods like LDA in transparent fluids and UDV in opaque ones as well as direct numerical simulations, see e.g. [Eggels, *et al*., 1994] lead to a further insight.

11.5 Void fraction sensors

In the concept for an accelerator-driven system (ADS) the injection of gas is considered as a method to generate a natural convection inside the liquid metal loop. In order to control the flow rate of the liquid metal and the resulting pressure drop the structure of the two-phase flow in the riser has to be known. Besides the description of the integral state of a two-phase flow, which is described of by the void fraction the local conditions are of interest. Therefore, measurement equipment is required to measure locally the void fraction, the bubble size and the individual transport velocities.

Like for the local measurement methods the application of intrusive and non intrusive methods can be applied also in liquid metals. Intrusive methods are e.g. the local resistive probes, while a non-intrusive sensing can be achieved by means of X-ray (γ-ray) techniques, neutron radiography (NR) or the ultrasound Doppler velocimetry (UDV). Due to the opaqueness of the fluid optical or fibre optical methods can not be used. The high specific electric conductivity of liquid metals does not allow the use of impedance probes, because hardly any electric field of significant size can be built up within the fluid, see [Cho, *et al*., 2005]. In bad electrically conducting media sometimes the magnetic resonance imaging (MRI) is used, which requires considerable large permanent magnetic [Daidzic, *et al*., 2005]. However, the interaction of the magnetic field with the fluid motion yields Lorentz forces altering the flow pattern and void distribution within the duct in such a way, that the intended measuring quantity is hidden behind the magneto-hydrodynamic effects.

The consecutive chapter describes the techniques successfully applied to liquid metals so far its operations principles and its deficits. It starts from the global methods acquiring the void fraction within a defined cross-section and continues with the individual devices measuring the local effects. In contrast to the single-phase investigations the information about two-phase liquid metal flow instrumentation is rather sparse. Nevertheless, the author tries to present the currently available technologies and discusses its limitations.

11.5.1 Electromagnetic sensors

An exact description of the characteristics of two-phase flow is required for better performance and safety design of power plant and air-conditioning machinery. In general, it is not easy to measure simultaneously the liquid volume flow rate and the void fraction under the existence of a gas phase. The electromagnetic flow-meter has been used successfully and accurately to measure the mean liquid velocity in various industries for about 40 years.

The electromagnetic flow meter is a device for detecting the potential difference between electrodes that is induced when a conducting fluid flows through a magnetic field, see e.g. Section 11.2.1. The feasibility of using the electromagnetic flow meter for measuring the characteristics of two-phase flow has been continuously considered. The reasons for this are that it makes no pressure drop, it has fast response for the change of flow, and it can effectively use the sharp difference between conductivities of two phases. There are many potential applications for the electromagnetic flow-meter in two-phase flow, but uncertainty due to the effects of the non-conducting phase also exists. As for electromagnetic flow meters, generally two types of electromagnetic void fraction sensors can be used: the DC permanent magnetic sensors and the AC sensor types. Both are described below.

11.5.1.1 DC permanent magnet void fraction sensors (PMVS)

The permanent magnet void fraction sensors (PMVS) rely on the same principle as the DC permanent magnetic flow meter (PMF), presented in Section 11.2.1.1. Also the experimental set-up is the same, consisting of a permanent magnet imposing a steady magnetic field *B*, penetrating the geometry to be investigated. The electrodes are arranged both perpendicular to flow u with u_f and u_g and the magnetic field *B*, where u_f is the mean fluid velocity and u_g the mean velocity of the gas. Further on the subscripts "*f*" and "*g*" denote the fluid and the gas, respectively. Since liquid metals possess a high specific electrical conductivity being order of magnitude larger than that of its vapour or the one of other gases one can assume that to the leading order the signal output of a PMVS will be a linear function of the liquid velocity alone up to a high value of vapour volume fraction. This postulation, however, assumes that at least to the temporal mean a uniform current path is maintained normal to the liquid metal flow.

The flow of a two-phase stream may be expressed as:

$$m_f = \rho_f A(1-\alpha)u_f \tag{11.54}$$

where α represents the gas volume fraction, m_f the mass flux and A the ducts cross-section. The ratio u_f/u is obtained from Eq. (11.55)a and the total mass flow m is equal to sum of the gas and liquid flows as in Eq. (11.55)b.

$$\frac{u_f}{u} = \frac{m_f}{m}(1-\alpha) \quad , \quad m = m_f + m_g \tag{11.55 a,b}$$

Defining the quality x as $x=m_g/m$ one gets:

$$\frac{u_f}{u} = \frac{(1-x)}{(1-\alpha)} \tag{11.56}$$

Considering now only low qualities in the range $0 < x < 0.02$, Eq. (11.56) mutates to:

$$\alpha = 1 - \frac{u}{u_f} \tag{11.57}$$

in which u and u_f can be independently measured by permanent electromagnetic flow meters; one in the two-phase domain as $\Delta\phi$ and the second in the single phase flow $\Delta\phi_f$. Connecting both readings one gets directly the void fraction from:

$$\alpha = 1 - \frac{k_f \Delta\phi_0}{k \Delta\phi_{f0}} \tag{11.58}$$

where k_f and k are the calibration constants of the single and the two-phase electromagnetic flow meters. In alkali liquid metals this technique has been successfully proofed by [Heinemann, *et al*., 1962]. In their tests the compared the PMVS experimental data with γ-ray measurements and they obtained an accuracy of this method of ±5% up to void fractions of 66% and temperatures of 600°C. However, the claimed that a high temperature wetting procedure was necessary to ensure constant thermal-electric properties at the fluid wall interface, unless a reliable reading could not be achieved. Also for mercury as a representative of a high density liquid metal this technique has been successfully demonstrated by [Hori, *et al*., 1966]. In case of well electrically wetting fluids this technique has been improved by [Ochiai, *et al*., 1971].

Additional correction factors for a more accurate detection of the void fraction value were made by [Murakami, *et al*., 1990]. Correlation techniques to acquire high temporal resolutions were made by [Velt, *et al*., 1982]. However, the latter three works concentrated mainly on the use in alkali metals.

11.5.1.2 AC electromagnetic void fraction sensors (EMVS)

A method to overcome the problems of direct wetting of the surface is given by AC sensors, similarly as for the flow meters. In Figure 11.5.1 an EMVS invented and successfully tested by [Cha, *et al*., 2002] is shown.

Figure 11.5.1. (a) Schematic drawing of the EMVS used by [Cha, *et al*., 2003]. (b) Normalised output of electromagnetic flow meter considering the ratio of correction factor with void fraction α after [Cha, *et al*., 2003].

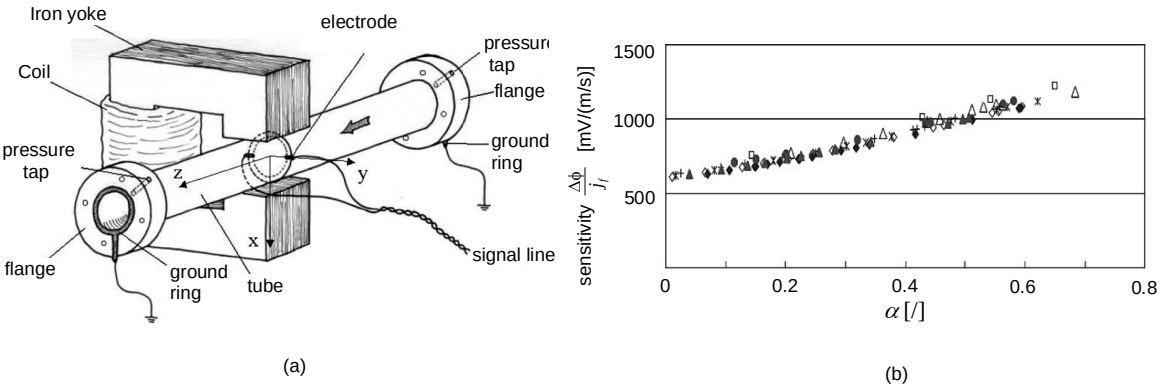

Within their device the electromagnet of the electromagnetic flow meter is sinussoidally excited and controlled by a frequency converter and an uninterruptible power system. The flow meter is composed of a signal detector and a signal processor. A pair of corrosion-resistive and non-magnetic electrodes is mounted along the inner wall of the test tube. Lead wires to draw out the signal are connected at both electrodes, and shielded for noise proofing, with the shield lines being grounded at one end. One of the greatest difficulties in electromagnetic flow meter design is that the amplitude of the voltage across the electrodes is of the order of a few millivolts, which is relatively small compared with extraneous voltages and noise. The main noise sources of electromagnetic flow meters, excited by AC power, are as follows:

- the transformer signal from the alternating magnetic field (including the effect of eddy current in the flow tube);
- noise from the capacitive and resistive coupling between signal and power circuits.

The following effects that distort the signal (flow signal) corresponding to flow rate should be noted:

- fluctuation of the magnetic field due to fluctuation of the power input;
- iron loss and hysteresis effects of the electromagnet;
- amplifier loading effect from the impedance of measuring devices.

To avoid the difficulties stated above, a somewhat complex signal processing unit was needed. The signal processor has an input stage with voltage followers, a filtering stage and an amplifying stage with large gain ($> 10^2$). To cancel out the differential noise (transformer signal), a counter differential noise is generated intentionally before the voltage followers with a kind of pickup coil and variable resistor. Low-frequency excitation using a frequency converter enables to reduce the noise by capacitive and resistive coupling between the signal and power circuits. Using these procedures, noise can be reduced considerably, and zero-flow tuning is possible. A reference resistor is used to ensure the reference voltage must have the same phase as the excitation current. From the reference voltage, information about the characteristics of the magnetic field can be inferred, and the comparison between flow signal and noise is possible.

Further, the EMVS requires a single-phase calibration procedure to determine the calibration constants. In fact, the void fraction can not be measured directly with one device in the liquid metal/ gas system. By using two EMVS an artificial void fraction can be calculated from the signals of the two electromagnetic flow meters under the assumption that the ratio of correction factors of both flow meters is unity, similar as for the DC flow meters. For the single-phase flow calibration of each of the devices, the correction factors can be determined. As a result from both calibrations one gets a linear dependence of the signal ratio versus the void fraction for low void fractions up to $\alpha = 0.3$. However, this signal ratio is not the actual real void fraction value since the ratio of correction factor is not unity: It is a function of fluid conductivity and hence is coupled to the void fraction. The effective conductivity σ_{eff}, however, can be calculated by the correlation experimentally determined by [Petrick & Lee, 1964] and thus the signal ratio can be corrected to obtain the real void fraction. The result obtained by [Cha, *et al*., 2003] for a sodium-nitrogen system showed an uncertainty of less than 2%. The result is shown in Figure 11.5.1(b).

$$\sigma_{eff} = \frac{(1-\alpha)^2}{1+\alpha}\sigma_f \quad \text{for} \quad 0 \le \alpha \le 0.7, \tag{11.59}$$

11.5.2 X-ray, γ-ray and neutron radiography (NR)

The attenuation of various radiations has been used quite successfully by different experimenters since the late fifties [Hooker & Popper, 1958] or [Petrick & Swanson, 1958]. Nearly all of them have been applied to light metals previously considered for the fast breeder research. The growing interest of the metal casting industry as well as the transmutation of minor actinides put the focus on heavy liquid metals, which require strong source due to the large absorption. In the past decade these sometimes continuously-operating high power sources became available [Baker & Bonazza, 1998], [Satyamurthy,

et al., 1998], [Mishima, *et al*., 1999] or [Saito, *et al*., 2005]. An additional support in using the below described techniques came due to the improved computer technologies and the progress in the image processing algorithms.

11.5.2.1 X-ray absorption

This subsection describes the technique developed for visualisation of the multi-phase mixture and the transient measurement of the two-dimensional distribution of chordal averaged void fraction applicable to liquid metal gas two-phase systems. X-rays have been used successfully in the visualisation of vapour explosion phenomena and the measurement of void fraction by several authors. One example of the use of a flash X-ray source is the visualisation of the fragmentation process in single droplet vapour explosions by [Ciccarelli & Frost, 1994]. A recent use of flash X-rays to measure void fraction was the study of hot particles plunging into water by [Theofanus, *et al*., 1994]. But the use of a continuous source of X-rays for the measurement of void fraction in molten metal systems with gas is still seldom. First successful attempts in the system tin gas were made by [Baker & Bonazza, 1998]. Since this is still the standard it is described more extensively.

The imaging through a layer of heavy liquid metal and an additional structural material e.g. steel requires a high energy beam and a high dose rate to get data that can be used in quantitative analysis. [Baker & Bonazza, 1998] used for a 100 mm tin layer ($\rho_{tin} \sim 7{\cdot}10^3$ kg/m^3) and 25 mm steel walls a continuous spectrum X-ray source with a peak energy of 9 MeV and an on-axis dose rate, one meter from the source, of 30 Gy/min to image the test section. The X-ray source pulses at approximately 275 Hz at this dose rate. The pulse frequency may be synchronised with the imaging system so that a constant number of one to nine pulses is collected for each frame. In most cases the X-ray and imaging systems are left unsynchronised to avoid a serious noise component introduced in the video signal.

The focal spot for the Baker-Bonazza (1998) X-ray source is less than 2 mm. The X-ray head is mounted on a scissor lift table that allows it to be moved vertically and aligned with the image collection system. Images are collected using an X-ray sensitive glass screen. The conversion screen is imaged through a mirror and a lens onto an inverting image intensifier which is coupled to one of two CCD cameras by means of a relay lens. Then the images are digitised and stored with a frame grabber. The signal path is shown in Figure 11.5.2(a).

Figure 11.5.2. (a) Arrangement of a void fraction measurement using the X-ray technique and the associated image recording. (b) X-ray image of gas injection at a rate of 9.2 cm/s into 11 kg of molten tin at 421°C. The top edge of the molten tin pool is clearly visible from [Baker &Bonazza. 1998].

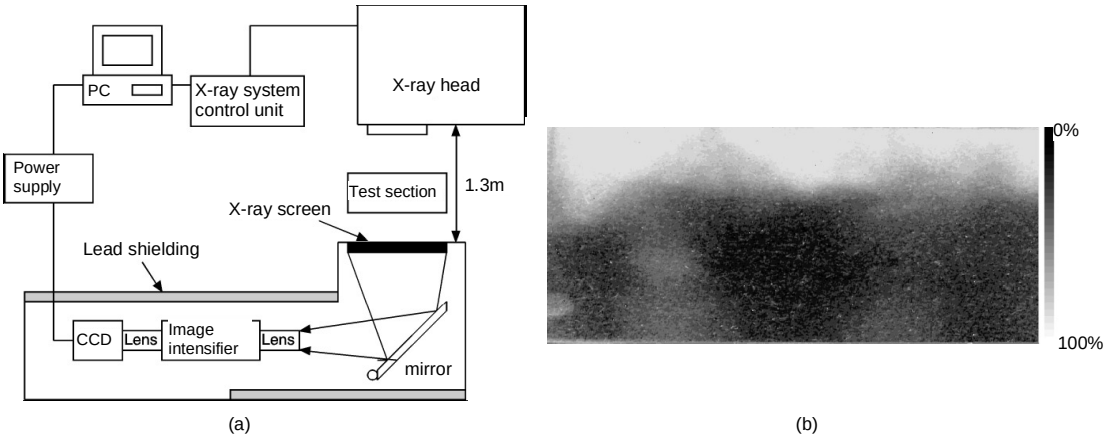

The first step to obtain a digital image is to eliminate the effect of the CCD camera's dark current. In a next step the images are normalised against any spatial non-uniformity of the X-ray source output. In the third step the images have to be normalised against any spatial non-uniformity originating from the structure of the test section. All these steps are achieved by means of subtracting a dark current constant D from each pixel value $P(x,y)$, and by dividing this difference by the difference between the corresponding pixel value of an image of the empty test section (obtained immediately prior to the pouring of molten liquid metal into the test section), $P_0(x,y)$, and the same dark current constant, D. The logarithm of this ratio is a grey level from here on indicated as $P_{liquid}(x,y)$.

$$P_{liquid}(x,y) = \ln\left[\frac{P(x,y) - D}{P_0(x,y) - D}\right] \tag{11.60}$$

Due to the exponential nature of the interaction of the X-rays with material, $P_{liquid}(x,y)$ is directly proportional to the thickness of the absorbing material in the test section as described below. Since the production of secondary radiation from the test section structure is small, this technique also accounts for the attenuation that occurs in the structure of the test section. The value of each pixel in the subtracted image is dependent on the material; the X-ray beam must traverse when travelling from the source to the X-ray sensitive, glass screen. At an average energy of approximately 3 MeV, water, water vapour, and nitrogen gas are undetectable and the intensity I of the pixel (gray level) is only dependent on the amount of liquid metal in the beam path and the magnitude of scatter present in the imaging plane. This relationship, where the liquid metal thickness, z_{liquid}, is the product of the liquid metal density and the portion of the chordal path length comprised of the liquid metal, is:

$$\frac{I}{I_{empty}} = B\exp\left[-\left(\frac{\mu}{\rho}\right)_{liquid} z_{liquid}\right] \tag{11.61}$$

where I is the X-ray fluence intensity in photons per square centimetre, B the built-up factor, μ the magnetic permeability $4\cdot\pi\cdot10^{-7}$ As/(Vm) and ρ the density of the fluid.

Since the pixel values are linearly proportional to the intensity of the light reaching the CCD sensor, the image can be thought of as a two dimensional mapping of the chordal average amount of liquid metal, along the beam path. If one assumes that the liquid vapour or the injected gas are void within the liquid metal, then the liquid metal chordal average can be related to the void fraction as:

$$\alpha(x,y) = 1 - \frac{z_{liquid}(x,y)}{z_0(x,y)} \tag{11.62}$$

in which $z_0(x,y)$ is the amount of liquid metal along the beam path for zero void at the individual test conditions. Running an arbitrary experiment at different temperatures the thermal expansions both of the liquid metal and the test sections has to be taken into account, since both quantities modify the density the X-ray beam faces.

The difficulty in the data reduction is in determining how to compensate for the scatter of X-rays. This is frequently neglected in studies with much thinner test sections and low energy X-rays. But our test section is several mean free paths thick, and therefore produces a significant amount of scatter when high energy X-rays are used. If the scattered X-rays are distributed homogeneously in the plane of the glass screen, the previously mentioned linear relationship between the chordal average amount of tin and the grey level is maintained and each individual image may be calibrated using two known

points to define the relationship between the grey level and liquid metal thickness. These two points allow the slope, *m*, and intercept, *b*, to be calculated and a calibration line may be defined as:

$$P_{liquid}(x,y) = b - m \cdot z_{liquid}(x,y) \tag{11.63}$$

In order to check for this linear relationship a solid liquid metal piece is inserted into the test section and a large amount of images has to be taken. By an averaging procedure one single image is obtained. This procedure substantially reduces the noise in the image and is the preferred method of quantitative imaging of static objects. The mean grey level for the pixels in the image of each step can then be measured. Repeating this procedure with liquid metal pieces of different thickness a linear relation between grey level and liquid metal thickness should be obtained. If the secondary radiation is not as assumed above, the void distribution in the test section would effect the calibration. A series of performance experiments conducted by [Baker & Bonazza, 1996] in which the void fraction distribution within a test box was artificially changed by means of Styrofoam balls demonstrated that there is little to no effect on the measurement of void fraction due to void distribution.

Once established that a linear relationship between grey level and liquid metal chordal average thickness exists, the calibration of each individual image in an experimental run can be accomplished with two points to define the calibration line. The grey level associated with 0% void is determined from the darkest pixel value. Typically this region is in the bottom corners of the test section or between the two injection ports for gas lifting. Depending on the height of the liquid metal within the test section, the grey level associated with 100% void is determined from either the region above the level of the liquid surface; or from the image of a hollow steel tube, sealed at both ends, of the same chordal length as the test section, placed at the upper right corner of the field of view. The linear relationship between these two points is used to relate the spectrum of grey levels to the chordal average amount of the liquid metal. An example of a two dimensional map of void fraction is shown in Figure 11.5.2(b) for an experiment that involved only gas injection into 11 kg of molten tin by [Bonazza & Baker, 1998]. There, twelve grey levels in the image represent equal bands of void fraction between 0% and 100%. For example, the darkest grey level represents a void fraction band of 0-8.3% void while the next grey level represents 8.4-16.6% void and so on. The integral (volume averaged) void fraction for the image can be obtained by calculating an average grey level weighted by the number of pixels in each band in the image, N_i, as follows:

$$\alpha = \frac{\sum_i N_i \alpha_i}{\sum_i N_i} \tag{11.64}$$

where α_i represents the average void fraction for the *i*-th band with N_i pixels. The conditions exhibited in Figure 11.5.2(b) represent an average void fraction of 25.9% for the entire volume.

Noise and unsharpness

Although image quality is frequently discussed on the basis of sharpness and contrast, these are poor measures for a quantitative analysis of the errors involved in void fraction measurement. As suggested by [Macovski, 1983], a better measure is the signal-to-noise ratio (SNR) defined as:

$$SNR = \frac{(I_2 - I_1)}{SD} \tag{11.65}$$

where I_1 is the background or 100% void signal, I_2 is the signal of interest, and *SD* is the standard deviation of I_2. The processes that must be considered to estimate the signal-to-noise ratio are photon

generation, photon interaction with the test section and metal, photon to light conversion in the glass screen, light collection through two lenses, the light photon conversion to electrons in the image intensifier and the CCD sensor, and the signal digitisation. If one assumes that the energy of the X-ray source is either constant or Poisson distributed, then the photons that are emitted from the source are Poisson distributed with parameter N, the number of photons emitted. The transmission of the beam through the test section is accounted for by modelling the beam absorption in the structural steel and liquid metal as a series of binomial processes. The beam that exits the test section is therefore still Poisson distributed, but with parameter M given by:

$$M = N \cdot \exp\left[-\left(\frac{\mu_{steel}}{\rho_{steel}}\right) z_{steel}\right] \exp\left[-\left(\frac{\mu_{metal}}{\rho_{metal}}\right) z_{metal}\right] \tag{11.66}$$

assuming the test section to be made of steel and the subscript "*metal*" indicating the liquid metal to be investigated. As for any Poisson distributed random variable with parameter M, the standard deviation is just the square root of M.

To account for the glass screen, intensifier and camera, several processes must be included. First, the screen must absorb or interact with an incoming photon. This process may also be modelled as a binomial process. Second, the production of light photons following X-ray absorption is modelled as a Poisson process. Then, the intensifier and CCD camera are modelled as additional Poisson distributed amplification stages that account for photon to electron and electron to photon conversions in the intensifier as well as the light collection efficiency of the camera. As derived by several authors, including [Macovski, 1983], this results in the following expression for SNR:

$$SNR = \left(\frac{I_1 - I_2}{I_1}\right) \cdot \frac{\sqrt{1 - \exp\left(\mu_g x_g\right) M}}{\sqrt{1 + \frac{1}{g_1} + \frac{1}{g_1 g_2} + \frac{1}{g_1 g_2 g_3}}} \tag{11.67}$$

where g_1, g_2, and g_3 are the gains of the glass screen, image intensifier and camera respectively.

The last step in the imaging chain is the digitisation that occurs in the CCD camera. This increases the noise in the image by the factor F_D, derived by [Swindell, *et al*., 1991]:

$$F_D = \left[1 + \frac{1}{12}\left(\frac{N_m \cdot SD}{2^8}\right)\right]^{\frac{1}{2}} \tag{11.68}$$

where N_m is the number of electrons required to produce a maximum video signal and SD is the standard deviation of the signal prior to digitisation. The final factor which must be accounted for is the effect of X-ray scatter on the SNR. Scatter produces an additive noise to that of the primary photons already accounted for. The scatter reduces the SNR by a factor F_s, which depends on the number of photons in the primary beam, N_p, the number of photons at the imaging plane due to scatter, N_s, and the ratio, q, of the glass screen X-ray to light conversion efficiencies for scatter and primary photons. F_s was shown by [Jaffray, *et al*., 1994] to be:

$$F_s = \frac{1}{\sqrt{1 + \left(q \cdot \frac{N_s}{N_p}\right)}} \tag{11.69}$$

Scattered photons are at a lower energy than the primary photons so they have a lower absorption probability but a higher light production per absorbed photon. Using the correction for the parameters discussed, one can estimate the maximum error in the void fraction determination.

To illustrate the effect of noise, one can determine the minimum size void that would be detectable in a liquid metal pool. A common method to determine the size of a void that is detectable by a human observer is to assume that contrast must be at least five times the noise in the system. The void detectability and image quality are also limited by the image unsharpness which can be attributed to three sources. First, the finite size of the X-ray source focal spot creates a geometric distortion or penumbra. Second, the inherent characteristics of the glass screen limit resolution as does the requirement that the size of an area imaged by a single pixel of the camera must be at least a half of the detectable void size. Overall, it is evident that noise considerations will limit void detectability to a much larger extent than the image unsharpness produced in the digital imaging system.

Errors due to mixture dynamics

In addition to the effects of system noise, scatter, and image unsharpness on the visualisation and measurement of void fraction, the effects of the multiphase system dynamics on the measurement accuracy must be analysed. The most significant source of error is the motion of the liquid metal and gases and the consequent void fraction fluctuations during the time required to obtain an image. The fluctuations in the amount of void along the beam path increase the transmission of X-rays through the mixture as shown by [Harms & Laratta, 1973] and [Oyedele & Akintola, 1991]. Examples of phenomena that could result in these fluctuations are bubble growth or movement in the test section as shown in Figure 11.5.3. This effect will result in the present measurements overestimating the actual void fraction. If one models the void fluctuations as variations about a mean, $\alpha + \Delta\alpha$, then the transmittance of X-rays is increased by a factor F_T, derived by:

$$F_T = 1 + \frac{\lambda^2 \langle \Delta\alpha \rangle^2}{2} \quad , \quad \Delta\alpha = \frac{1}{\lambda} \ln\left[\frac{1}{\tau} \int_{t=0}^{t=\tau} \exp(\lambda\alpha(t)) dt \right] - \frac{1}{\tau} \int_{t=0}^{t=\tau} \alpha(t) dt \qquad (11.70)\ \text{a,b}$$

where λ is the number of mean free paths along the beam direction through the test section. An expression for this dynamic error was subsequently derived by [Harms & Laratta, 1973] as Eq. (11.70)b. In this equation t is the time required to collect one image frame. A detailed knowledge of the void fluctuation with time is required to estimate the error. Since this information is mostly not available, reasonable estimates of the largest possible fluctuations must be made from the rise velocity of bubbles in the multiphase mixture.

Figure 11.5.3. Illustration of the void dynamics that increase X-ray transmission. Void growth or the increase in the number of voids along the beam path as illustrated in Case 1 will increase transmission. Void movement or change in distribution without a change in the total void along the beam path, as illustrated in Case 2 will not result in a transient change in X-ray transmission.

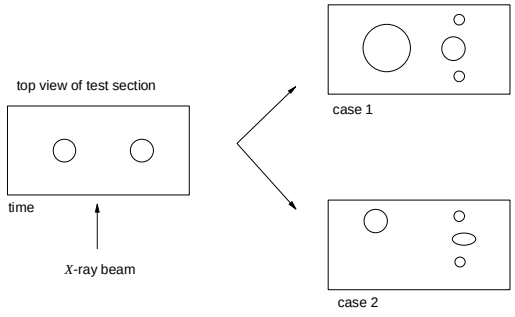

11.5.2.2 γ-ray absorption

Because of extreme complexity of two-phase flows, most of the well known empirical relations and models give area averaged void fractions. Since void fraction varies across the cross-section of the pipe, to determine averaged void fraction, void fraction profiles as a function of radial distance should be determined. This can be two-dimensionally through one cross-section determined by means of the γ-ray absorption technique.

Figure 11.5.4. Scheme for the cross-sectional measurement of the two-dimensional void fraction profile using γ-ray absorption from [Satyamurthy, *et al*., 1998]

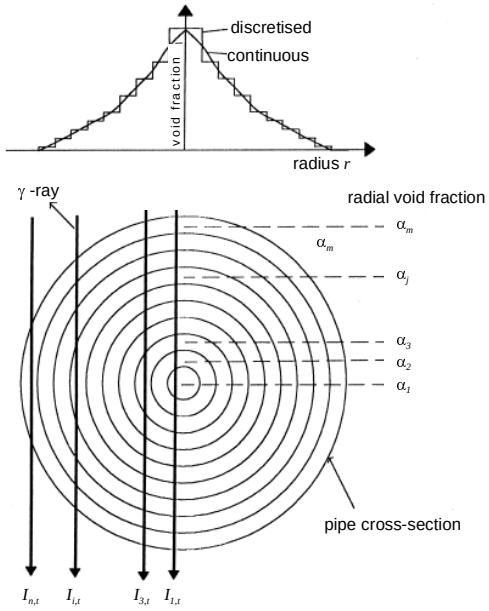

For this purpose the cross-section of the two-phase-flow in the pipe is assumed to have a number of circular zones owing a uniform void fraction in each zone. This is schematically depicted in Figure 11.5.4. Consider now "*m*" circular zones having the void fractions α_1, α_2, …, α_j,…, α_m to be determined and additionally let β_1, β_2,…, β_i,…., β_n be the measured void fractions at the various chord lengths, then one gets:

$$\beta_i = \sum_{j=1}^{m} \frac{d_{ij}}{c_i} \alpha_j \tag{11.71}$$

where c_i is the total path length for the gamma ray at the *i*-th chord length and d_{ij} is the length of the *j*-th zone intercepted by the gamma ray beam at the *i*-th chord length. β_{is} are obtained from measured gamma ray intensities at the *i*-th chord with gas alone ($I_{i,g}$), with liquid metal alone ($I_{i,l}$) and when two-phase flow is present ($I_{i,t}$) and are given by:

$$\beta_i = \frac{\ln\left[\dfrac{I_{i,t}}{I_{i,l}}\right]}{\ln\left[\dfrac{I_{i,g}}{I_{i,l}}\right]} \tag{11.72}$$

Let E be the error function defined as follows:

$$E^2 = \left(\sum_{i=1}^{n} \beta_i - \sum_{j=1}^{m} \frac{d_{ij}}{c_i} \alpha_j \right)^2 \tag{11.73}$$

The minimisation of E with respect to the m parameters of α_1, α_2, …, α_j,…, α_m gives a set of of m linear equations. Using the measured values of β_1, β_2,…, β_i,…., β_n the values of α are obtained.

In the experiment performed by [Satyamurthy, *et al*., 1998] in a mercury nitrogen mixture, the number of chords chosen was 38 with 2.0 mm spacing. Seven zones were assumed. From the void fraction profiles, the area averaged void fraction was determined. The beam diameter (3 mm) was chosen so that finite beam errors were negligible [Satyamurthy, *et al*., 1994] besides obtaining a large number of zones. Number of counts were taken in excess of 6000 for every measurement so that statistical fluctuations were negligible (<1.5%) [Munshi & Vaidya, 1993]. In addition, dynamic void fluctuation corrections were estimated to determine the error range in the analysis [Thiyagarajan, *et al*., 1991].

Corrections for the void-fraction measurements

In a two-phase flow, void fraction fluctuation increases the radiation transmittance. Because of this the measured void fraction from this transmitted radiation intensity will be greater than the time-averaged void fraction [Harms & Forrest, 1971]. The effect of these fluctuations with respect to the attenuation parameter λ (= $\mu \cdot l/M$) is studied in detail by [Thiyagarajan, *et al*., 1991]. If the fluctuation magnitude (maximum deviation from average) is known, then the exact error due to the fluctuation can be determined. Corrections for two types of fluctuations – large ones (±100% deviation from the average) and medium ones (±50% deviation from the average) – have been worked out for a given attenuation parameter. Due to the non-availability of data on the degree of fluctuation in the experiment, the required correction for dynamic fluctuation is applied by the following procedure. The fluctuation correction for maximum possible fluctuation magnitude (±100% deviation from average) is applied to the measured data β', and the corrected value β'' is obtained. The exact dynamic fluctuation-corrected void fraction lies between β' and β''. Radial void fraction profiles are obtained separately with the uncorrected data (β') and the corrected data (β''). The average of the two profiles is considered the dynamic fluctuation-corrected void fraction profile.

Statistical fluctuation correction

Radioactive decay obeys Poisson's distribution law and is prone to random statistical fluctuations in the gamma-ray emission. It is well known from counting statistics that the maximum error involved in any intensity counts N is equal to $N1/2$. Since the measured void fraction is related to three intensities as given in Eq. (11.73), the effect of statistical fluctuation has to be determined. In this method, it can be shown that the error due to statistical fluctuation is described by Eq. (11.74).

$$\frac{\Delta\alpha}{\alpha} = \frac{1}{\alpha}\left(\frac{1}{\ln\left(I_g / I_l\right)} \right) \cdot \left[\frac{1}{I} + \frac{\alpha^2}{I_g} + \frac{(\alpha - 1)^2}{I_l} \right]^{\frac{1}{2}} \tag{11.74}$$

Herein, ε_i is the dimensionless error in one particular measurement.

Calibration, effort and accuracy

Due to the high density especially of the heavy liquid metals quite strong γ-sources are required. In case of [Satyamurthy, *et al*., 1998] a cobalt-60 emitter with an activity of 2775 MBq was chosen as

the γ-ray source. Moreover, for the measurements 1.33 MeV photons were used which expands the capabilities of most of the liquid metal laboratories.

To determine the overall accuracy in measuring the void fraction profile, a static simulation system of gas and liquid metal is required similarly as for the X-ray technique in order to determine the individual levels corresponding to a specific void fraction value. The output of this process which must be performed with the liquids later used in the experiment is a calibration curve. If this is properly done void fraction profiles with an accuracy of about ±5% can be measured with the γ-ray absorption.

11.5.2.3 Neutron radiography (NR)

Neutron radiography (NR) is one of radiographic techniques which make use of the difference in attenuation characteristics of neutrons in materials [von der Hardt and Röttger, 1981]. Since thermal neutrons easily penetrate heavy materials like dense metals and are attenuated well by light materials as those containing hydrogen, NR was developed as a technique for non-destructive inspection which is complementary to X-ray radiography in the automobile and aerospace industries [Barton, 1993]. Recently, the application has spread to various scientific fields such as agricultural, medical and dental sciences, as well as application to porous materials like concrete and brick. Moreover, fluid research with use of the dynamic method of NR, namely the real-time NR has been a great hit because this technique is suitable for visualisation of a multiphase flow in a metallic casing [Mishima, *et al*., 1992; Hibiki, *et al*., 1994a] and a liquid metal [Takenaka, *et al*., 1994]. With spreading application fields, it is thought that the research trend is changing from qualitative to quantitative applications. Some attempts have been made to use *NR* not only as a tool for visualisation but also as a tool for quantitative measurement. Quantitative utilisation can be classified into two categories.

The first is to use the geometrical information extracted from NR images, for example, a measurement of particle trajectory and velocity [Ogino, *et al*., 1994], and hold up in a fluidised bed [Chiba, *et al*., 1989]. The second is to use the attenuation characteristics of neutrons in materials, for instance, measurement of void fraction in multiphase flow [Mishima, *et al*., 1993], [Hibiki, *et al*., 1993]. For this purpose, quantification method, namely the Σ-scaling method was developed [Hibiki & Mishima, 1996].

Basic concept of the neutron radiography

The mass attenuation coefficient of X-rays increases monotonically with the atomic number. On the other hand, thermal neutrons easily penetrate most of metals, while they are attenuated well by such materials as hydrogen, water, boron, gadolinium and cadmium. In other words, X-ray radiography takes advantage of the difference in densities, while NR takes advantage of the difference in neutron absorption cross-sections. Therefore, it is clear that NR is more suitable for observing the fluid behaviour in a metallic duct and liquid metals.

The block diagram of the imaging system for high-frame-rate NR with a steady neutron beam is shown in Figure 11.5.5. Here, the test section is set up in front (right-hand side) of the scintillator. When the neutron beam penetrates two-phase flow in the test section, the beam is attenuated in proportion to the liquid layer thickness along its path. Thus, the neutron beam projects the image of two-phase flow. The neutron beam which conveys the image of two-phase flow is changed into an optical image by the scintillator. The luminous intensity of the optical image is then increased by an image intensifier to obtain a better image. After the image is enlarged with a telephotographic lens, it

Figure 11.5.5. Schematic view of the neutron components falling on the converter screen and the subsequent path for processing the data for the void fraction measurement using neutron radiography (NR)

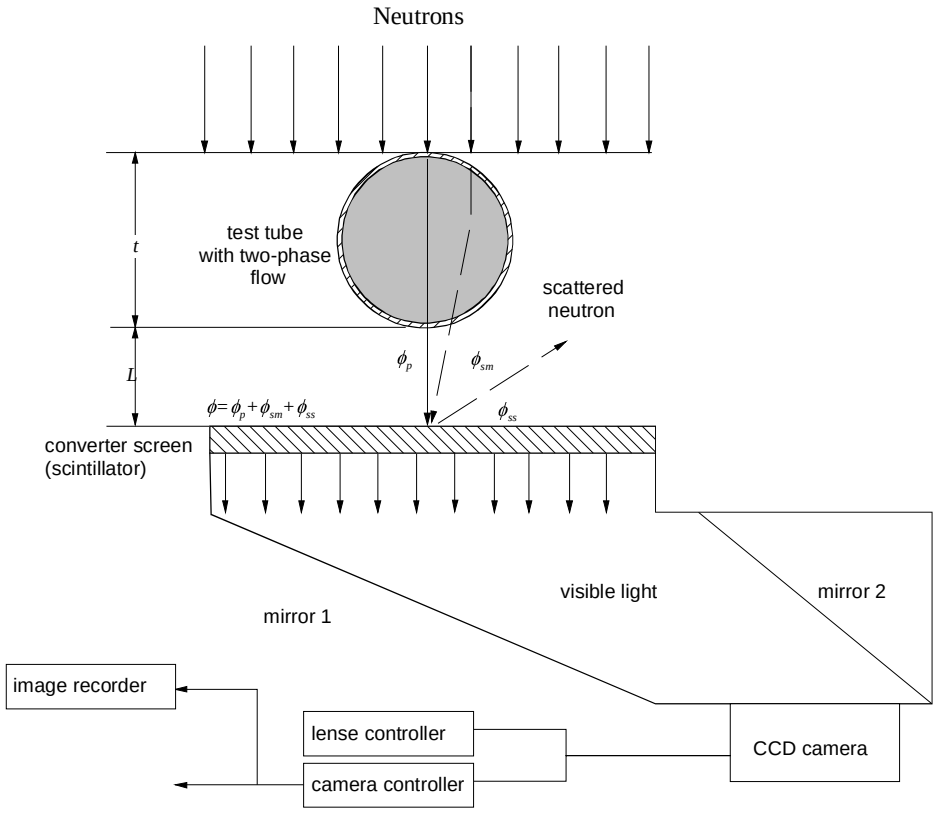

is detected with a high-speed video camera. The quality of the obtained image can be improved by using an image processing system consisted of an image memory and image processor. The following are necessary conditions to achieve a high-frame-rate NR for liquid metal two-phase flows:

a) a considerable large high flux neutron source (nuclear reactor);

b) a high sensitivity scintillator;

c) a high-speed video system with high reliability and long recording time;

d) a high performance image intensifier or a high sensitivity camera.

Each condition is discussed briefly below.

a) The neutron source

The neutron beam of thermal reactors is not mono-energetic. The spectrum has a Maxwellian distribution in the thermal region, a distribution proportional to 1/E above 0.5 eV, and a bump in the fast region around 2 MeV. Above 10 MeV, the distribution drops rapidly. In sample materials this leads to beam hardening. As the sample becomes thicker, the lower energy parts of the spectrum are depleted at a faster rate than the higher energy parts because of the larger cross-section at low energy, decreasing the effective attenuation coefficient for thicker samples. Thus, a correction for beam hardening is inevitable.

Fast neutron radiography (FNR) is attractive as a non-destructive inspection technique due to the excellent matter penetration characteristics of fast neutrons. It is especially suitable for non-destructive inspection of industrial products that are too thick or dense to be inspected by conventional thermal neutron radiography (NR). Despite the availability of various fast neutron sources such as nuclear reactors, radioisotopes, and accelerators without a neutron moderator, FNR is not in widespread use. One of the reasons for this is the difficulties in clearly discriminating γ-rays associated with the neutron beam. These problems were overcome by the use of imaging plates with γ–ray discrimination [Matsubayashi, *et al*., 2001] and an FNR converter using wavelength-shifting fibres [Matsubayashi, *et al*., 2003].

b) Conversion screen or scintillator

The scintillator to be used in high-frame-rate *NR* should have characteristics of a high light yield, high resolution, short light decay time. Since rare earth scintillators of gadolinium compounds have a long light-decay time and glass scintillators have a low light-yield, these are not applicable to high-frame-rate NR. Only zinc sulphide scintillators mixed with lithium fluoride meets currently the above three conditions.

c) High speed camera

The purpose of developing high-frame-rate NR with a steady neutron beam is to visualise rapid phenomena for a long time period. Therefore, a high-speed video with a long recording time should be used, although the sensitivity is also important.

d) Image intensifier

Regarding the image intensifier a high amplification rate of order 105 with a high frame rate and a high resolution in terms of ´line pairs per millimetres is required to capture oscillations. The image intensifier has to be matched to the high speed camera.

Due to the oscillations of the neutron spectrum in a reactor, spatial variations of the beam and varying random noise a lot of effort has to be spent in the pre-processing of images to correct systematic noise errors. A detailed description of this procedure can be found in [Richards, *et al*., 2004]. Once the pre-processing is done and the reference measurements to obtain the flat field images for a single-phase only (gas/liquid), no duct inside are conducted in order to correct for scattering, etc. the void fraction measurement can start.

The principle of the void fraction measurement

The flux of incident neutron ϕ_{th} is attenuated in the liquid and the structure material of the test section, thus:

$$\phi = \phi_{th} \cdot \exp\left[-\Sigma_G \, \delta_G - \Sigma_L \, \delta_{ML} - \Sigma_t \, \delta_t\right] + \phi_S \tag{11.75}$$

where ϕ and ϕ_S denote the total neutron flux falling on the converter and scattered neutron component, respectively. Ignoring the neutron absorption in the gas phase, the measured grey levels *G* are given by the following equations for the gas-filled (subscript "*G*"), liquid-filled (subscript "*L*"), and two-phase mixture-filled (subscript "*ML*") test sections.

$$\begin{aligned}\tilde{G}_G^0 &= C\phi_{th}\cdot\exp\left[-\Sigma_t\,\delta_t\right]+G_0 \quad ;\\ \tilde{G}_L^0 &= C\phi_{th}\cdot\exp\left[-\Sigma_L\,\delta_L-\Sigma_t\,\delta_t\right]+G_0 \quad ;\\ \tilde{G}_M^0 &= C\phi_{th}\cdot\exp\left[-\Sigma_L\,\delta_{ML}-\Sigma_t\,\delta_t\right]+G_0\end{aligned} \tag{11.76}$$

where G_0 is the offset term which consists of scattered neutron component G_S and dark current G_D; $G_0 = G_S + G_D$. The tilde (~) denotes that the grey levels among the images were normalised, i.e. by matching the reference brightness at some point outside the test section where neutron attenuation is negligible. Usually the dark current term G_D is uniform and can be treated as an offset. On the other hand the scattered neutron component G_S is not always uniform. To treat G_0 as an offset, the scattered neutron component G_S should be spatially uniform. The scattered neutron component G_S consists of neutrons scattered in the test section G_{SM} and those scattered in the surrounding background objects G_{SS}:

$$G_S = G_{SM} + G_{SS} = C\left(\phi_{SM} + \phi_{SS}\right) \tag{11.77}$$

Since ϕ_{SS} is, in most cases, spatially uniform, the scattered neutron component G_S could be made spatially uniform if ϕ_{SM} is spatially uniform or negligible. This condition can be achieved by taking a sufficiently large distance L' between the test section and the converter. The minimum of this distance is currently being estimated experimentally to be about the width of the test section. With this uniform G_S, the term G_0 can be treated as a constant offset. Then, from Eq. (11.76), the offset term G_0 can be determined using the grey levels obtained from the liquid filled and gas-filled test sections by:

$$G_0 = G_S + G_D = \frac{\tilde{G}_L^0 - \tilde{G}_G^0\exp\left(\Sigma_L\delta_L\right)}{1-\exp\left(\Sigma_L\delta_L\right)} \tag{11.78}$$

Finally, the void fraction α is obtained by:

$$\alpha_0 = 1-\frac{\delta_{ML}}{\delta_L} = \frac{\ln\left(\tilde{G}_L/\tilde{G}_M\right)}{\ln\left(\tilde{G}_L/\tilde{G}_G\right)} = \frac{\ln\left(\tilde{G}_L^0 - G_0/\tilde{G}_M^0 - -G_0\right)}{\ln\left(\tilde{G}_L^0 - G_0/\tilde{G}_G^0 - -G_0\right)} \tag{11.79}$$

In this method, the offset term G_0 is determined based upon the total macroscopic cross-section Σ_L, and quantitative information is derived from grey levels which are relative quantities by nature. In this sense, this is called Σ-scaling method. As discussed above, this method assumes that the offset term G_0 can be made spatially uniform by taking a large distance L'. It should be noted here that the un-parallelness of the incident neutron beam causes image blur, especially in the vicinity of material boundary. The spatial resolution is given by the distance L' and the L/D ratio of the NR facilities as follows:

$$R = \frac{L'}{\left(L/D\right)}. \tag{11.80}$$

Therefore the appropriate range of $L'$to be used in f-scaling method should be an optimum value taking account of the above two requirements. This method was tested with a known void profile [Matsubayashi, *et al*., 2004].

Moreover, to confirm this method for the void fraction of two-phase flow in a rectangular duct gas velocities calculated from the void fractions measured by the NR method are compared with those by conductance probe methods [Mishima, *et al*., 1993], [Saito, *et al*., 2005] as shown in Figure 11.5.6(a). Since the measured values by high-frame-rate NR are particularly affected by the statistical variation

Figure 11.5.6. (a) Comparison of the measured void fractions taken by the real-time NR, optical and conductance probe methods with the drift correlation from [Mishima, *et al*., 1997]. (b) Simultaneous time series of void fraction and resistive (conductance) probe signals in a lead-bismuth nitrogen two-phase flow from [Saito, *et al*., 2005].

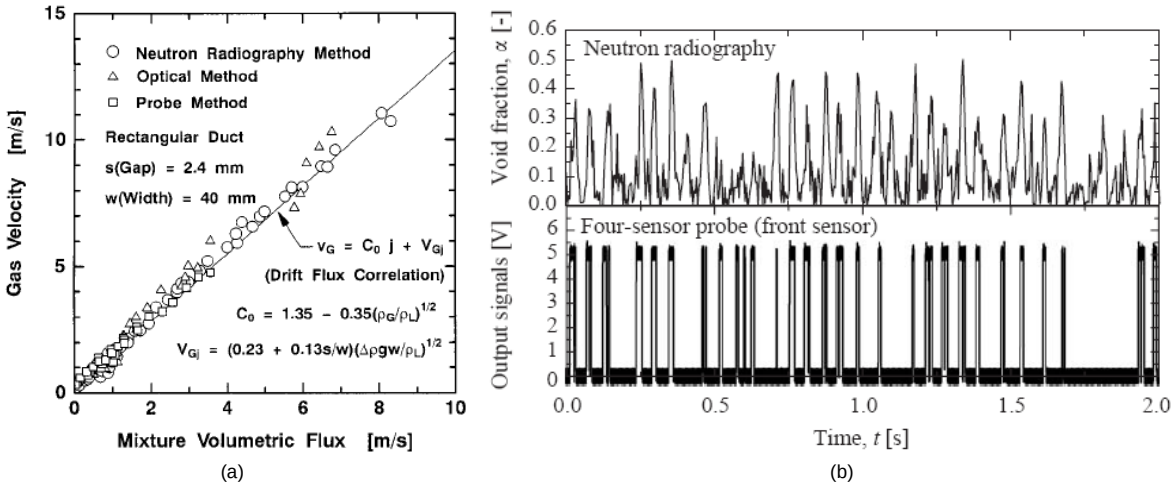

of neutrons, the integrated image of the images obtained by the real-time NR with the recording speed of 30 frames per second instead of the high-frame-rate NR was used here. The solid line indicates the prediction by the drift flux correlation for a rectangular duct [Griffith, 1963], [Ishii, 1977]. It is shown that the measured values are consistent with each other and correlated well by the drift flux correlation. The measurement error by the NR method is estimated to be less than 5%. The sensitivity of the high speed NR compared to intrusive methods like resistive (or conductance) probes is by orders of magnitudes larger than the latter. They are not affected by local effects close to a probe tip, wetting effects are material compatibility. With one scan consisting of several frames a complete void fraction profile along a tube can be acquired. By using an Abel integration, which implicitly assumes axis-symmetry even the two-dimensional void fraction profiles can be reconstructed, see [Saito, *et al*., 2004, 2005]. A comparison of the NR performance and its resolution to a conductance probe is shown in Figure 11.5.6(b) on the example of a time series of the measured void fraction.

11.5.3 Resistive or conductance probes

The resistive probes are local sensors with an electrically conducting tip (Cr/Ni wires, tungsten, stainless steel or platinum, with diameters ∅ 0.1 mm) in direct contact with the liquid. These kinds of probes are usually supplied with an AC current operating typically at frequencies in the range from 1-25 kHz. The AC source induces an electric current flowing from the probe tip to an opposite electrode (e.g. the probe support or the channel wall). The gas contact at the sensitive wire is detected by an interrupt of the electrical current. Due to the huge differences in the electrical conductivity between the gas and the metal, one obtains sharp signals easy to evaluate by a threshold method.

The measuring quantity is the ratio of the gas contact time to the total sampling time. This ratio yields a time averaged local void fraction. From this method also the number of bubbles during the total sampling time are known and hence the bubble frequency. The measurement principle of resistive probes is shown in Figure 11.5.7.

Figure 11.5.7. (a) Measuring principle of the resistive probes. (b) Typical signal delivered by a single-wire resistive probe in a sodium/argon bubbly flow.

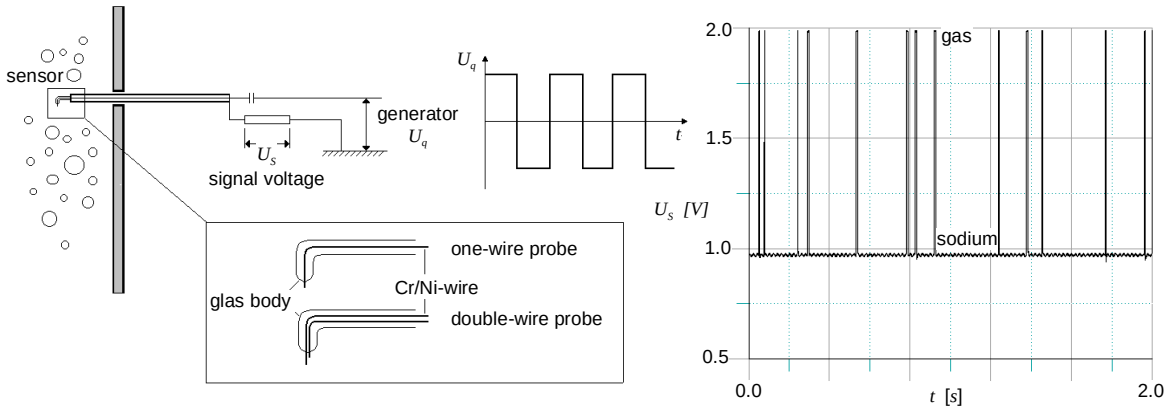

If the probe is supplied with a single wire tip the local void fraction α can be measured. A double wire probe, where the two electrodes are installed with a distinct displacement in flow direction, allows in addition the determination of the bubble velocity from the time delay of the signal between both electrodes. Further, the bubble chords can be yielded from the product of the velocity and the measured gas contact time at the probe. Methods to transform the chord-length distributions into bubble-size distributions have been suggested by several authors. In any case the significant interaction between the bubbles and the local sensor has to be taken into account. Large measuring errors have to be expected for the measurement of the bubble velocity or the chord length by means of double-wire probes if not appropriate measures are taken.

The electrical resistive probe method is attractive for bubbly flow measurements because of its relative simplicity and wide applicability. It detects the passage of interfaces at the tip of each sensor, and uses this data to determine void fraction and bubble size and velocity, see [Delhaye, 1983], [Serizawa, *et al*., 1975] or [Kocamustafaogullari & Wang, 1991]. The optic fibre has a faster response, but besides the opaqueness of liquid metals, the found commercial probes are both expensive and too fragile to use in heavy liquid metals and in the large bubble column experiments typically appearing.

Early versions involved only one needle, which gave two different signals depending upon whether the needle tip was in a bubble or in liquid. [Hills, 1974] used a short needle with a single 90° bend and investigated the radial variation of gas hold-up in a vertical bubble column. [Neal and Bankoff, 1963] also used the single 90° bend configuration and analysed bubble signals in terms of autocorrelation functions to obtain local values of gas fraction, bubble frequencies and bubble size.

[Serizawa, *et al*., 1975] developed the method further and presented a double-sensor probe for measuring local values of air-water bubbly flows. This probe had the advantage that it was capable of measuring bubble velocity from the time lag between a pair of upstream-downstream signals. It consisted of two identical electrically insulated needles placed side-by-side with their tips about 5.0 mm apart. [Kocamustafagullari & Wang, 1991] recommended a 2.5 mm separation to account for possible bubble size and bubble velocity. A comprehensive list of previous probe designs is given in [Sanaullah, *et al*., 2001]. The problem with the two-point probe is the difficulty of matching the signals from the two needles which correspond to the same bubble, especially since bubbles do not always rise vertically, and often strike the probe with a glancing blow.

One attempt to improve the situation is to use a five-point probe [Burgess & Calderbank, 1975] or [Buchholz & Steinemann, 1984] with a leading needle surrounded by four needle tips in the same horizontal plane a few millimetres downstream of the central tip. The extra complexity involved has meant that these devices have not been used as much as the simpler two-point probe. One of the major concerns with multiple probes is that the leading needle may interfere with the bubble, and so disturb the reading of the downstream needle(s). The Burgess & Calderbank's algorithm (1975) for analysing data from his five-point probe rejected any bubble not seen simultaneously by three equi-spaced downstream needles, thus ensuring that only "head-on" collisions, least likely to be affected, were analysed. This, however, meant that only a very small sample of the bubble population was included, raising doubts about whether the sample was representative.

The orientation of the resistive probe needles is commonly either horizontal (perpendicular to the bubble path) or vertical. In the horizontal configuration, the ability of the probe to withstand the lateral drag of the fluid becomes an important factor; in the double needle probe, this leads to uncertainty about the exact vertical positions, and hence the separation, of the tips. However, with any double sensor probe, the two tips must be vertically one above the other, which is impossible if both needles are vertical. Most recent workers have used two very fine needles touching each other. However, the use of touching needles means that there is a danger of the liquid meniscus in the channel between them affecting the behaviour of the downstream needle tip. A common orientation in commercial two-point optic-fibre probes is to separate the two needles, but to bend the upstream one so that the two tips are aligned, but this raises the question as to whether the different orientations of the two probes influences the result.

Probe design

A design of a two-pole and a four pole probe used in liquid metal experiments is shown in the Figures 11.5.8. The wires have usually a distance of 2-5 mm from each other and are aligned with respect to the main flow direction. A too large a separation can introduce errors in the detected signals as multi-bubble contact may occur between two signals originating from the same bubble, whereas too small a separation will lead to errors in the estimation of velocity. The two sensors are electrically insulated from the probe body, except their tips, which are made by simply cutting the ends off the insulated wires. The other ends of the wires are soldered to two coaxial cables. The soldered connections are carefully electrically insulated using air dried insulating varnish and as an additional measure for safe insulation soldered connections are wrapped by heat shrinking plastic tubes. The other

Figure 11.5.8. (a) Schematic illustration of an inclined dual-sensor resistive probe from [Sanaulla, *et al*., 2001]. (b) Sketch of a four-pole resistive sensor used in PbBi by [Saito, *et al*., 2005].

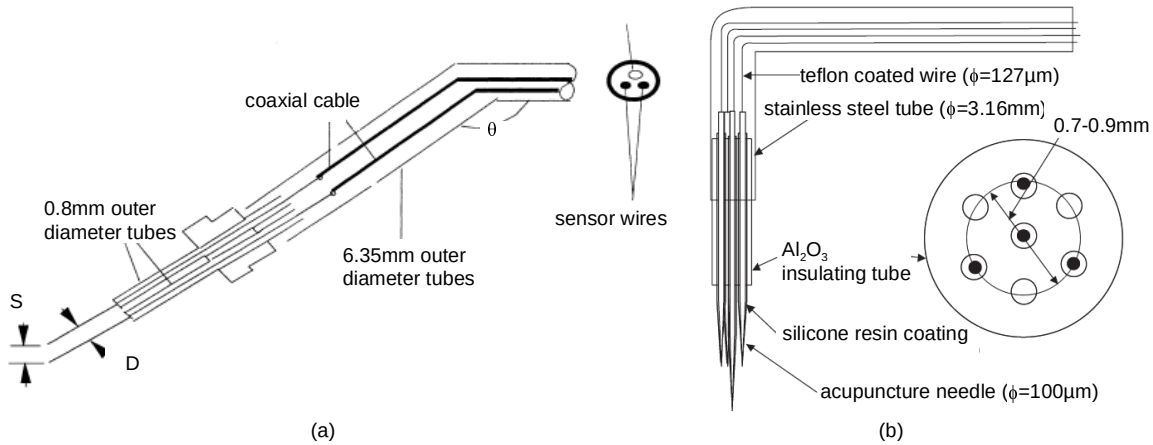

ends of the coaxial cables are connected to the bubble signal processor. The screens of these cables are joined to a lead whose other end touches the liquid metal in the column as the "ground". The signal processor mainly compares the resistance between the probe tip and the ground. A constant potential of several volts DC is applied across each needle and the potential across a series resistor is amplified to provide the output signal.

Data processing

The raw signals obtained by the probe are not square-waves as to ideal contact or not. This is due to the relatively slow drainage of liquid film formed around the sensor tip, which leads to a slow rise time as compared to the sharp fall time when the sensor re-enters the water. To obtain bubble properties, it is necessary to have data in terms of perfect square-waves with the rise and fall corresponding to the precise moment when the needle enters and leaves the gas phase. For this purpose, the raw data are differentiated, and the moment when the value of the derivative crosses a certain threshold is used as the interface contact time. This processing can be implemented via software algorithms. A detailed description is given in the thesis of [Cheng, 1997].

The local void fraction α can be calculated from the sum of duration time t_g for bubbles at the upstream probe for the sample time T:

$$\alpha = \frac{\Sigma t_g}{T} \tag{11.81}$$

Using the time lag between the signals for the two sensors and the vertical distance L between them, the velocity of the i-th bubble, u_{Bi}, can be determined by:

$$u_{Bi} = \frac{L}{t_{di}} \tag{11.82}$$

where the average displacement time of liquid-gas interface and gas-liquid interface for a bubble travelling between the two sensors is given as:

$$t_{di} = \frac{1}{2}\left(t_{dri} - t_{uri}\right) + \frac{1}{2}\left(t_{dfi} - t_{ufi}\right) \tag{11.83}$$

where subscript "*d*" and "*u*" corresponds to downstream and upstream, respectively, and "*r*" and "*f*'' corresponds to rise and fall signals, respectively. The bubble chord length L_{Bi} is then obtained as:

$$L_{Bi} = u_{Bi}\left(t_{uri} - t_{ufi}\right) \tag{11.84}$$

where the upstream contact time is used, as explained above, for its greater reliability.

Estimating bubble size distribution from the bubble chord length distribution is not easy, and even estimating the mean bubble size and velocity is not without problems. Since the probe is more likely to see a large bubble than a small one, complicated weighting factors are needed. In order to use the resistive probe for two-phase studies, it is most important to establish a statistical model that relates the local interfacial area concentration to the measured quantities. Over the past twenty years, different statistical models for local interfacial area concentration measurement using a double-sensor probe have been developed. In this context only the four most common models are described. The evaluation of multi-tip probes is more sophisticated and requires several estimates, which would expand the scope

of this presentation. A detailed description of the methods there required is given in the papers by [Dias, *et al*., 2000], [Kim, *et al*., 2001] or [Shen, *et al*., 2005]. Here, only the different methods for two-tip arrangements are described.

Statistical methods to evaluate the local interfacial area concentration

a) Kataoka's statistical model (1986)

According to the definition of the local interfacial area concentration by [Ishii, 1975], [Kataoka, *et al*., 1986] carried out derivations and established a statistical model that related the local time-averaged interfacial area concentration a_i to the harmonic mean of the interfacial velocity. Consider the main flow is in *z*-direction. Assume that the bubbles are spherical, the probe passes every part of the bubbles with an equal probability, and there is no statistical relation between interfacial velocity and the angle between the interfacial velocity and the normal vector of the interface. With this statistical model the time-averaged interfacial are concentration can be expressed as:

$$\bar{a}_i^t = 4N_t \cdot \left(\overline{\frac{1}{u_{szj}}}\right) \cdot \frac{1}{1-\cot\left(\frac{\alpha_0}{2}\right)\ln\left(\cos\frac{\alpha_0}{2}\right)-\tan\frac{\alpha_0}{2}\ln\left(\sin\frac{\alpha_0}{2}\right)} \tag{11.85}$$

where u_{szj}, α_0 and N_t denote *z* component of the interfacial velocity, the maximum angle between the interfacial velocity and the mean flow direction, and the number of bubbles measured per unit time, respectively. On the derivation of Eq. (11.85), it is also assumed that the angle between the bubble interfacial velocity and the main flow direction, α, is random with an equal probability within some maximum angle α_0. The value of α_0 is determined from the statistical parameters of the measured interfacial velocity. Assuming that the interfacial velocity fluctuations in three directions are equilateral [Kataoka, *et al*., 1986] derived the relationship between the maximum angle α_0 and the standard deviation of bubble velocity fluctuation in the main flow direction with the following form:

$$\frac{\sin 2\alpha_0}{2\alpha_0} = \frac{1-\sigma_z^2/\overline{u_{szj}^2}}{1+3\sigma_z^2/\overline{u_{szj}^2}} \tag{11.86}$$

where σ_z denotes the root mean square of the interface velocity fluctuation. For more details on the mathematical modelling of this measurement method, one can refer to [Kataoka, *et al*., 1986]. The interfacial area a_i can the be used to estimate the Sauter mean diameter d_s, using:

$$d_s = \frac{6\alpha}{\bar{a}_i} \tag{11.87}$$

b) Kalkach-Navarro's statistical model (1993)

[Kalkach-Navarro, *et al*., 1993] assumed that the bubbles were spherical and the bubble sizes were represented by a probability distribution function, $f(V_j)$, where $f(V_j)\Delta V$ was the number of bubbles per unit volume having a volume between V_j and $V_j + DV$. From the geometrical consideration, they proposed the following statistical model for local interfacial area concentration measurement:

$$\bar{a}_i^t = (36\pi)^{\frac{1}{3}} \sum_j f(V_j) V_j^{2/3} \Delta V_j \tag{11.88}$$

where V_j is the volume of the group-*j* bubbles and calculated from the chord length measured by a double-sensor probe. In order to determine $f(V_j)$, the maximum chord length measured is divided into equal partitions, then a probability of each partition of chord length is obtained. Assuming the bubbles can be penetrated at any point with equal probability by the sensor tips, a triangular matrix, which represents the relationship between the probability of the chord length cut by sensors and the probability of bubble radius, is established. Then, the bubble size probability distribution function, $f(V_j)$, can be derived from the probability distribution of the bubble radius. In this model, however, the authors derives straightway the relations for local measurement from the chord length distributions, and take no account for the effect of bubble lateral motions.

c) Hibiki's statistical model (1998)

[Hibiki, *et al*., 1998] conducted a similar derivation to Kataoka, *et al*. (1986) based on basically the same assumptions, except for the probability density function of α, the angle between the bubble interfacial velocity and the main flow direction. In view that the probability density function of a has a peak in the main flow direction from the experimental data, they replaced the equal probability within a maximum angle of α, using the following relations:

$$g(\alpha)=\begin{cases}\dfrac{1}{\alpha_0^3}(\alpha-\alpha_0)^2 & for \quad 0\le\alpha\le\alpha_0\\ 0 & for \quad \alpha_0\le\alpha\le\pi/2\end{cases} \tag{11.89}$$

They derived the following relations between the maximum angle, α_0, and the standard deviation of bubble velocity fluctuation in the main flow direction:

$$\frac{3}{\alpha_0^2}\left(1-\frac{\sin 2\alpha_0}{2\alpha_0}\right)=\frac{1-\sigma_z^2/\overline{u_{sz}^2}}{1+3\sigma_z^2/\overline{u_{sz}^2}} \tag{11.90}$$

d) Wu's statistical model (1999)

[Wu and Ishii, 1999] carried out sensitivity study through numerical method on double-sensor conductivity probe measuring local interfacial area concentration. They assume that the bubble velocity fluctuation is isotropic and the bubble is spherical. Considering the effects of bubble lateral motions and the distance between the two tips of the double-sensor probe, and taking the contribution of the missed bubbles into account, a statistical model is obtained also from the definition by [Ishii, 1975] as:

$$\bar{a}_i^t=\frac{2N_b}{\Delta T(N_b-N_{miss})}\cdot\left(\overline{\frac{1}{u_{szj}}}\right)\cdot\left[2+\left(\frac{u_b'}{u_b}\right)^{2.25}\right] \tag{11.91}$$

where ΔT,N_b,N_{miss}, and u_b'/u_b denotes the sampling time, the total number of measured bubbles, the number of the missed bubbles, and relative bubble velocity fluctuation, respectively. The missed bubbles referred to those that are touched by the first sensor but not by the second sensor, or those that pass the second sensor ahead of the first sensor in view of the bubble lateral motions. The number of the missed bubbles can be obtained from the double-sensor probe signals directly. From numerical method, [Wu & Ishii, 1999] suggest the relative standard deviation of the inverse of the measured interfacial velocity to characterise the relative bubble velocity fluctuation with the following form:

$$\frac{u_b'}{u_b}=0.85\cdot\frac{\sqrt{\overline{1/u_{szj}}-\left(\overline{1/u_{szj}}\right)^2}}{\left(\overline{1/u_{szj}}\right)} \tag{11.92}$$

where 0.85 has been determined by their numerical analysis. When the bubble diameters are in the range from $1.2\Delta s$ to $3\Delta s$, the authors report that the error of the above relation is in the range of ±10%, where Δs denoted the distance between the two tips of the double-sensor probe.

Experimental experience and accuracy

The impact of inclination of the probe with respect to the main flow is a critical issue. Here, especially the effect of the interaction between the two needles, by calculating bubble frequency or void fraction from the upstream or the downstream needle makes this obvious. The accuracy of the double tip probes can be checked by comparing the calculated values of the void fraction and the gas superficial velocities with those determined manometrically. The agreement is of course not better than the statistical methods used for the signal processing and thus around ±10%.

A better agreement is only obtained for more advanced statistical methods. If e.g. the bubbles are categorised into two groups, such that group one includes spherical and distorted bubbles and group two includes cap and slug bubbles, then correction methods in calculating the local a_i for missing and non-effective bubble signals can be formulated accounting for different contributions from various bubble interfaces. Such a procedure was successfully tested by [Kim, *et al*., 2001]. The deviation between experiment and numerical simulations shrinks to a few per cent only.

11.5.4 Ultrasound Doppler velocimetry (UDV) for two-phase flows

Detection of bubbles or particles in a dominant liquid two-phase flow inside pipes or vessels is important in research and industries. The ultrasonic pulse-echo method allows by means of liquid metal adapted waveguides to measure up to temperatures of 620°C [Eckert, *et al*., 2003], and dense media with a high sound velocity as gallium (~2600 m/s, compare [Brito, *et al*., 2001], however, to use the ultrasound technique for the determination of two-phase flows is quite new. A first attempt to analyse a two-phase flow using this technique was made by [Hofmann & Rockstroh, 1996]. There, a straight-beam transmitting-receiving probe transmits short bursts at regular intervals in the range 0.1 to 4 kHz and more, having an ultrasonic frequency in the range 1 to 10 MHz. The ultrasonic waves penetrate the wall and the two-phase flow. They will be directly reflected by the bubbles or particles and by the inner back wall of the vessel. The back wall echo is more intense in comparison with the direct echo in most cases. Reflected waves are received partially by the same probe and displayed on the screen of an ultrasonic echo detector as an echogram, as shown schematically in Figure 11.5.9(a).

If the sizes of objects (bubbles) and arrangements (structure elements like the pipe or an immersed body) are much greater than the ultrasonic wavelength the behaviour of ultrasonic waves can be considered as similar to optics in the following. If the inclination of reference object (the bubble) with respect to the emitter/sensor is too large, the cross-section the intensity of the received echo goes to zero. Assuming a homogeneous cylindrical sound field and neglecting any changes in wave mode, the largest inclination angle α_{R0} of a plane reflector (bubble) to be allowed can be calculated as follows:

$$\alpha_{R0} = \frac{1}{2} a\tan\left(\frac{d_p c_l}{2c_s l_s\left(1+\frac{c_l l_l}{c_s L_s}\right)}\right) \tag{11.93}$$

where c_s, c_l are the sound velocities of the wave guide and the liquid metal, l_s and l_l the length of the waveguide and the that of the fluid in sound direction, respectively. Having a probe transducer

Figure 11.5.9. (a) The principle of ultrasonic pulse-echo technique for two-phase flow measurement. (b) Experimental scheme of the PbBi bubbly flow facility from [Eckert, *et al*., 2003].

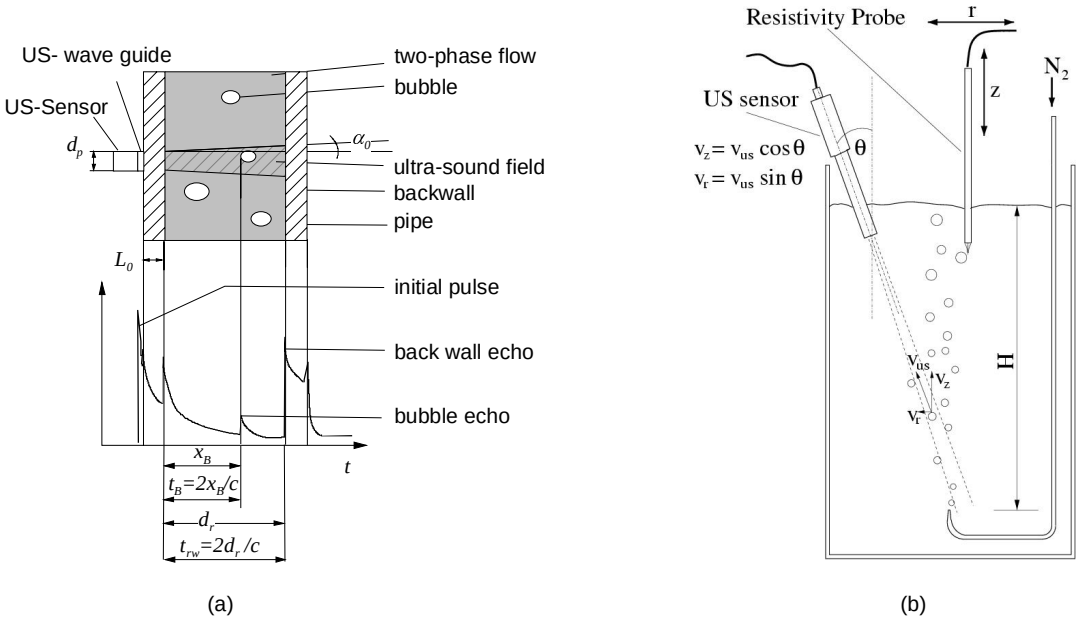

diameter d_p = 10 mm, l_l = 40 mm, l_s = 135 mm, c_l = 1730 ms^{-1} (liquid lead-bismuth), c_s = 5730 ms^{-1} (stainless steel), this angle has a value of α_{R0} =0.21° only! That means, an echo cannot be received by the probe if $\alpha_R > 0.21°$.

A great progress for the use of UDV in two-phase flows was achieved by the work of [Suzuki, *et al*., 2000, 2002]. When the ultrasound probe UVP is applied to bubbly flows, the system records velocities of both phases together. In their studies, the phase discrimination is made using pattern recognition. All stored instantaneous velocity profiles are classified into two groups with regard to existence of bubble data. If no bubble crosses the measuring line when an ultrasonic pulse is emitted, the obtained instantaneous velocity profile should give only negative values at all the measuring points in the channel. Such instantaneous velocity profiles are stored as Group A (ensemble averaged local liquid velocity profile distant from bubbles). On the other hand, if a bubble exists on the ultrasonic beam path, the obtained velocity profile has positive values near the gas-liquid interface. These profiles are stored as Group B (velocity profile around a bubble). The Group B profiles are rearranged according to the distance from the bubble's surface. Furthermore, in relation to the influence of wakes behind leading bubbles, instantaneous velocity profiles of Group B are subdivided into two groups, Groups B1 and B2. Group B1 includes velocity profiles that contain effects of leading bubbles. When the instantaneous velocity profile is not affected by leading bubbles, the profile is categorised into Group B2. The presence of the wake effect is determined by another pattern recognition. If a positive small peak exists between the transducer and the bubble's surface in an instantaneous velocity profile, that small peak is considered as the effect of the leading bubbles, or the wake. As a result of this pattern recognition and conditional sampling of data, the ensemble-averaged velocity is obtained at each relative distance from a bubble's surface.

Eckert, *et al*. (2003) improved Suzuki's technique and applied it to PbBi melts up to 300°C and CuSn melts with up to 620°C using nitrogen as gas. A sketch of their experimental set-up, which they referenced against a resistivity probe is shown in Figure 11.5.9(b).

An example of a typical velocity profile obtained from the bubbly flow can be seen in Figure 11.5.10(a). The lower velocity at the small measuring depths corresponds to the flow of the liquid metal that is driven by the rising bubbles. Since the ultrasonic pulse is reflected at the bubble interface, the velocity measured can be interpreted as an interfacial velocity. If the entire ultrasonic energy is reflected by the bubble as demonstrated in this example, no information can be received from measuring depths behind the bubble position, which is called the shadow effect. Measurements of the phase velocities and the bubble frequency can be obtained only for low void fractions ($\alpha < 0.1$), unless tomographic systems consisting of several transmitters and receivers are used as e.g. proposed by [Xu, *et al*., 1997] and [Beckord, *et al*., 1998]. However, such systems were currently not applied tow liquid metal two-phase flows.

Figure 11.5.10. (a) Typical measured velocity profile of a single bubble case from [Eckert, *et al*., 2003]. (b) Example of a calculated probability density function to separate both phase velocities.

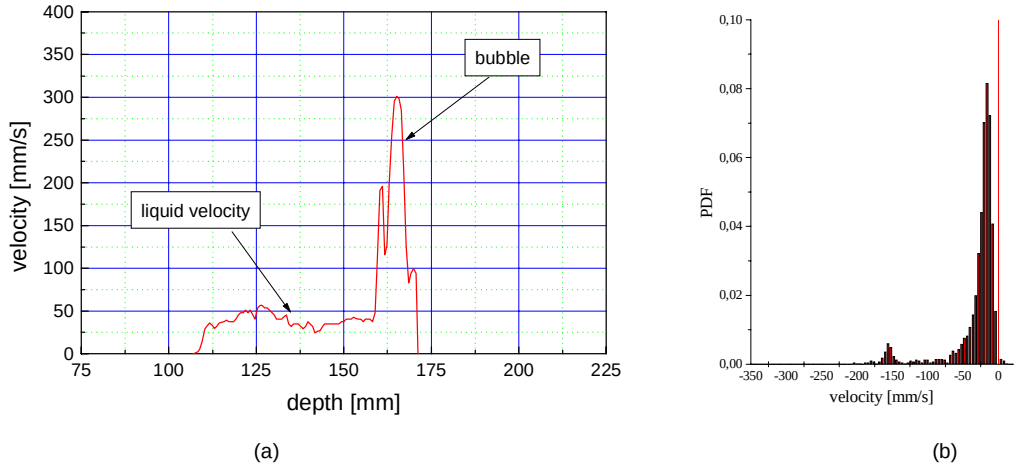

A phase separation of the measured velocities of the liquid and gas can be performed by calculating the corresponding probability density functions (PDFs). Here, the assumption is made that the PDFs of both phases can be expressed by a normal distribution, as shown for example in Figure 11.5.10(b). The PDFs were calculated in the [Eckert, *et al*., 2003] paper on the basis of 4.096 velocity profiles.

11.6 Temperature measurements

11.6.1 Thermocouples

The measurement of the liquid lead-bismuth temperature is usually performed using NiCr-Ni thermocouples being mantled by a stainless steel tubing. A careful determination of the temperature is necessary to determine the thermophysical data of the fluid. The diameter of the used elements varies between 0.25 mm and 3.0 mm depending on the time scales to be resolved at the desired location. Because of the high heat transfer coefficients that are characteristic of a liquid metal the frequency response of thermocouples is far higher than in conventional fluids. According to [Krebs & Bremhorst, 1983] a 0.25 mm sheathed thermocouple with an insulated junction gives undamped signals in sodium in excess of at maximum 40 Hz.

The temperature signal originating from a thermocouple arises from the thermo-electric effect. The connection of two different materials is called thermocouple. If two different types of metals are connected together by welding, soldering or only by twisting a voltage is generated. This can be

measured at the end of the two materials. At the connection of two different metals the electrons are changing from one metal into the other. Authoritatively for this process is the escape work of the electrons. The metal with the lower escape work delivers electrons and becomes positive. Thereby an electric field ϕ arises in the interface.

The contact voltage Δϕ which is generated in the contact surface is proportional to the Boltzmann distribution of the temperature T and also to the relation of the free-electron density n_A and n_B. This is the so-called Seebeck effect.

$$\Delta\phi = \frac{kT}{e_0} \ln\left(\frac{n_A}{n_B}\right) \tag{11.94}$$

where k is the Boltzmann constant and e_0 the elementary charge. The terms in the right side can be combined to the material constant k_{AB}. Then the equation reduces to:

$$\Delta\phi = k_{AB} \cdot T \tag{11.95}$$

About 13 “standard” thermocouple types are commonly used. Eight have been given internationally recognised letter type designators. The letter type designator refers to the electromotive force (emf) table, not the composition of the metals – so any thermocouple that matches the emf table within the defined tolerances may receive that table’s letter designator. Some of the non-recognised thermocouples may excel in particular niche applications and have gained a degree of acceptance for this reason, as well as due to effective marketing by the alloy manufacturer. Some of these have been given letter type designators by their manufacturers that have been partially accepted by industry. Each thermocouple type has characteristics that can be matched to applications. Industry generally prefers *K* and *N* types because of their suitability to high temperatures, while others often prefer the *T* type due to its sensitivity, low cost and ease of use. In Table 11.6.1 the standard thermocouple types are presented. The table also shows the temperature range for extension grade wire in brackets.

There are four common ways in which thermocouples are mounted with in a stainless steel or Inconel sheath and electrically insulated with mineral oxides. Each of the methods has its advantages and disadvantages. Good relatively trouble-free arrangement will be reached by the sealed and isolated from sheath mounting. The principal reason for not using this arrangement for all applications is its sluggish response time – the typical time constant is 75 seconds. The sealed and grounded to sheath mounting can cause ground loops and other noise injection. But, it provides a reasonable time constant (40 seconds) and a sealed enclosure. A faster response time constant (typically 15 seconds) is given by the exposed bead mounting. But it lacks mechanical and chemical protection, and electrical isolation from material being measured. The porous insulating mineral oxides must be sealed.

The fastest response time constant is gotten by the exposed fast response type. Typically for this arrangement are 2 seconds but with fine gauge of junction wire the time constant can be 1-100 ms depending on their diameter. In addition to problems of the exposed bead type, the protruding and light construction makes the thermocouple more prone to physical damage.

Because of their physical characteristics, thermocouples are the preferred method of temperature measurement in many applications. They can be very rugged, are immune to shock and vibration, are useful over a wide temperature range, are simple to manufactured, require no excitation power, there is no self heating and they can be made very small. No other temperature sensor provides this degree of versatility. Thermocouples are wonderful sensors to experiment with because of their robustness, wide temperature range and unique properties.

Table 11.6.1. ANSI registered thermocouple groups containing the accuracy, range and composition

Type	Positive material	Negative material	Accuracy*** Class 2	Range °C (extension)	Comments
B	Pt, 30%Rh	Pt, 6%Rh	0.5% >800°C	50 to 1820 (1 to 100)	Good at high temperatures, no reference junction compensation required.
C**	W, 5%Re	W, 26%Re	1% >425°C	0 to 2315 (0 to 870)	Very high temperature use, brittle.
D**	W, 3%Re	W, 25%Re	1% >425°C	0 to 2315 (0 to 260)	Very high temperature use, brittle.
E	Ni, 10%Cr	Cu, 45%Ni	0.5% or 1.7°C	-270 to 1000 (0 to 200)	General purpose, low and medium temperatures.
G**	W	W, 26%Re	1% >425°C	0 to 2315 (0 to 260)	Very high temperature use, brittle.
J	Fe	Cu, 45%Ni	0.75% or 2.2°C	-210 to 1200 (0 to 200)	High temperature, reducing environment.
K*	Ni, 10%Cr	Ni, 2%Al 2%Mn 1%Si	0.75% or 2.2°C	-270 to 1372 (0 to 80)	General purpose high temperature, oxidising environment.
L**	Fe	Cu, 45%Ni	0.4% or 1.5°C	0 to 900	Similar to J type. Obsolete – not for new designs.
M**	Ni	Ni, 18%Mo	0.75% or 2.2°C	-50 to 1410	
N*	Ni, 14%Cr 1.5%Si	Ni, 4.5%Si 0.1%Mg	0.75% or 2.2°C	-270 to 1300 (0 to 200)	Relatively new type as a superior replacement for K type.
P**	Platinel II	Platinel II	1.0%	0 to 1395	A more stable but expensive substitute for K & N types.
R	Pt, 13%Rh	Pt	0.25% or 1.5°C	-50 to 1768 (0 to 50)	Precision, high temperature.
S	Pt, 10%Rh	Pt	0.25% or 1.5°C	-50 to 1768 (0 to 50)	Precision, high temperature.
T*	Cu	Cu, 45%Ni	0.75% or 1.0°C	-270 to 400 (-60 to 100)	Good general purpose, low temperature, tolerant to moisture.
U**	Cu	Cu, 45%Ni	0.4% or 1.5°C	0 to 600	Similar to T type. Obsolete – not for new designs.

* Most commonly used thermocouple types. ** Not ANSI recognised types. ***See IEC 584-2 for more details.
Materials codes: Al – aluminium, Cr – chromium, Cu – copper, Mg – magnesium, Mo – molybdenum, Ni – nickel Pt – platinum, Re – rhenium, Rh – rhodium, Si – silicon, W – tungsten

On the down side, the thermocouple produces a relative low output signal that is non-linear. These characteristics require a sensitive and stable measuring device that is able provide reference junction compensation and linearisation. Also the low signal level demands that a higher level of care be taken when installing to minimise potential noise sources. The measuring hardware requires good noise rejection capability. Ground loops can be a problem with non-isolated systems, unless the common mode range and rejection is adequate.

In case of monitoring the temperature in electromagnetic flow meters or electromagnetic pumps misreadings may occur due to the ferromagnetic properties of the Ni-NiCr thermocouple. This effect increases dramatically if temperature gradients or gradients of the magnetic field exist. Numerous effects listed afterwards can lead to misreadings and as a consequence to misinterpretations during the operation. The temperature control far away from the magnets is performed by Ni-NiCr thermocouples. The dependence of the measurement signal against a reference ice point ($T = 0$°C) is shown in Table 11.6.2. The temperature measurements within the magnetic field are carried out using Cu-CuNi (copper-constantan) thermocouples, which dependence on the temperature is also shown in Table 6.2.

Figure 11.6.1. Sheath options of thermocouples (NI, 2003)

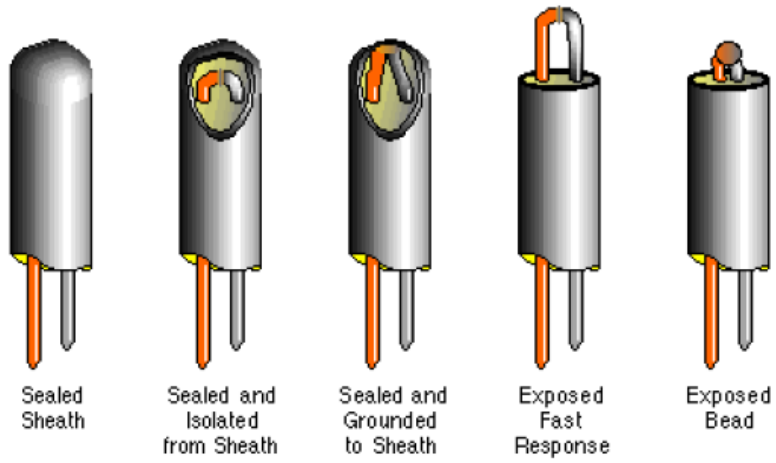

Table 11.6.2. Electric voltage of the thermocouples Cu-CuNi and Ni-NiCr in millivolts as a function of the temperature in the range from 0°C to 400°C. The temperature function is calculated from the electric voltage produced by the thermocouple with the following polynom: T [°C] = A0 + A1.U[mV] + A2.U2[mV].

Temperature	Cu-CuNi	Ni-CrNi	Temperature	Cu-CuNi	Ni-CrNi
0°	0.00	0.00	210°	9.74	8.54
10°	0.40	0.40	220°	10.29	8.94
20°	0.80	0.80	230°	10.85	9.34
30°	1.21	1.20	240°	11.41	9.75
40°	1.63	1.61	250°	11.98	10.16
50°	2.05	2.02	260°	12.55	10.57
60°	2.48	2.43	270°	13.13	10.98
70°	2.91	2.85	280°	13.71	11.39
80°	3.35	3.26	290°	14.30	11.80
90°	3.80	3.68	300°	14.90	12.21
100°	4.25	4.10	310°	15.50	12.63
110°	4.71	4.51	320°	16.10	13.04
120°	5.18	4.92	330°	16.70	13.46
130°	5.65	5.33	340°	17.31	13.88
140°	6.13	5.73	350°	17.92	14.29
150°	6.62	6.13	360°	18.53	14.71
160°	7.12	6.53	370°	19.14	15.13
170°	7.63	6.93	380°	19.76	15.55
180°	8.15	7.33	390°	20.38	15.98
190°	8.67	7.73	400°	21.00	16.40
200°	9.20	8.13	410°	21.62	16.82
Fit function polynom	A0	A1	A2	Temperature range	
Cu-CuNi.	3.4834965	23.22235	-0.21285	0°-410°C	
Ni-CrNi	-0.4179542	24.79475	-0.0201893	0°-380°C	

In principle six (!) thermo-magnetic effects exist which can influence the temperature measurement. An overview and a detailed description of these effects is given in the article of [Kollie, *et al*., 1977] and [Eringen, 1980]. The effects can be categorised as:

a) transverse effects Righi-Leduc effect and Nernst-Ettingshausen effect;

b) longitudinal effects in a transverse field;

c) longitudinal effects in a longitudinal field.

Both, b) and c) cause changes in the thermal conductivity and the Seebeck coefficient of a material. Of these effects the Righi-Leduc and the two longitudinal effects of the Seebeck coefficient are besides the Nernst-Ettingshausen effect the most important in thermocouple thermometry in a magnetic field. In general appropriate design considerations and material choices have to be made before instrumenting a test section. Only the consideration of the afterwards named effects and order of magnitude estimations prevent long term and exhausting calibration measurements.

The Nernst-Ettingshausen effect

If a temperature gradient ∇T is perpendicular to a magnetic field $\vec{\boldsymbol{B}}$ an electric field $\vec{\boldsymbol{E}}$ will be produced perpendicular to both quantities related to Eq. (11.96). The magnitude of the electric field is determined by the Nernst-Ettingshausen coefficient Q, which is a material property like the thermal conductivity of a material.

$$\vec{\boldsymbol{E}} \quad = \quad Q\left(\nabla T \times \vec{\boldsymbol{B}}\right) \tag{11.96}$$

The electromotive force *EMF* produced given by the integral along the wire from zero to the length l:

$$EMF \quad = \quad \int_{s=0}^{s=l}\left[Q\left(\nabla T \times \vec{\boldsymbol{B}}\right)\right] \quad ds \tag{11.97}$$

The Nernst-Ettingshausen factor Q for the four compounds appearing in the thermocouples Ni-NiCr and Cu-CuNi are shown in Table 11.6.3.

Table 11.6.3. Nernst-Ettingshausen coefficient Q and magnetic permeability μr of different thermocouple materials

Material	Q [10-11 V/(°C Gauss)]	μr magnetic permeability
Copper (Cu)	0.27	1
Copper-nickel (CuNi)	0.71	1
Ni (alumel)	5.25	5
NiCr (chromel)	27.00	1

Let us consider a configuration in which a temperature gradient of 50°C per mm exists, the thermocouple has a diameter of 0.5 mm and the magnetic field strength is 2 Tesla (2.10^4 Gauss). The thermocouple wires may have a length of 30 mm perpendicular to the temperature gradient and the magnetic field and they are insulated from each other by a magnesium oxide ceramic. A calculation which includes the heat conduction in the thermocouple yields the following astonishing result. The measurement error for a copper-constantan thermocouple for this set-up yields 1.015°Kelvin; for Ni-NiCr, however, on such a short length an error of 33.2°Kelvin is measured. Of course, the big assumed temperature gradient has been chosen to outline the measurement errors.

The Righi-Leduc effect

If a temperature gradient ∇T is oriented perpendicular to a magnetic field $\vec{\boldsymbol{B}}$ a temperature gradient ∇T_t will develop transverse to ∇T and $\vec{\boldsymbol{B}}$ according to Eq. (11.98).

$$\nabla T_t \quad = \quad S\left(\vec{\boldsymbol{B}} \times \nabla T\right) \tag{11.98}$$

Herein, S is the Righi-Leduc coefficient. However, Eq. (11.98) applies only if no heat flow occurs in direction of ∇T_t, which is under adiabatic conditions. Similar to the Nernst-Ettingshausen effect a line integral for the temperature difference ∇T can be formulated, which reads to:

$$\Delta T \quad = \quad \int_{s=0}^{s=l} \left[S\left(\vec{\boldsymbol{B}} \times \nabla T\right) \right] \quad ds \tag{11.99}$$

The Righi-Leduc effect results finally in a indicated temperature in a magnetic field that is different from that indicated without a magnetic field. However, for a 1 m long Ni-NiCr wire in a magnesiumoxid mantle exposed to a magnetic field of 2 Tesla and a transverse temperature gradient of 50°C/1 mm the error would be 45°C. The Righi-Leduc coefficient of nickel is 10^{-7}/Gauss whereas the NiCr value was assumed to be infinitely small in the absence of data.

The Seebeck-effect

The Seebeck coefficient of metals is changed in the presence of magnetic fields. Such changes cause errors in the temperature measurement because the thermal electromotive force of a thermocouple E_t is defined as line integral:

$$E_t \quad = \quad \int_{s=0}^{s=l_p} \left[Se_p \, \nabla T \right] \quad ds \quad - \quad \int_{s=0}^{s=l_n} \left[Se_n \, \nabla T \right] \quad ds. \tag{11.100}$$

along the length of the positive branch (l_p) and the negative branch (l_n) of the thermocouple. The positive and negative Seebeck coefficients Se_p and Se_n of non-ferromagnetic materials changes usually rather weak with the magnetic field [Kollie, *et al*., 1977]. For ferromagnetic materials the change is more expressed. The Seebeck coefficients for the two thermocouple pairs considered are shown in Table 11.6.4.

Table 11.6.4. Seebeck coefficients Se from [Kollie, *et al*., 1977] and [Powell, *et al*., 1974]

Material	Se [10-9 V/(°C)]
Copper (Cu)	±1
Copper-nickel (CuNi)	3±1
Ni (alumel)	37±1
NiCr (chromel)	2±1

Galvanomagnetic effects

Up to now only thermomagnetic effects are discussed. However, where magnetic fields appear also galvanomagnetic effects may appear due to the interaction of electric and magnetic fields and lead to a miscellaneous reading of a temperature signal. For example the Ettingshausen galvanomagnetic

effect, with the coefficient *Pg*, produces a transverse temperature gradient in a transverse magnetic field $\vec{B}$ and a current density *j* according to Eq. (11.101).

$$\nabla T \quad = \quad Pg\left(\vec{j} \times \vec{B}\right) \tag{11.101}$$

The coefficients *Pg* and the Nernst-Ettingshausen coefficient *Q* are related through the absolute temperature *T* and the thermal conductivity λ by Eq. (11.102):

$$\lambda\, Pg \quad = \quad T \cdot Q \tag{11.102}$$

11.6.2 Heat-emitting temperature-sensing surfaces (HETSS)

A technology to determine the heat flux transferred from a liquid metal flow through a thin walled structure is given by the heat emitting temperature sensing surface (HETSS) technique [Platnieks, *et al*., 1998] or [Patorski, *et al*., 2000].

The active element of the method is a simple surface that allows a well defined heat flux density to be generated in selected areas and the resulting temperature distribution to be recorded simultaneously. A HETSS represents the boundary between the solid and the liquid flow to be measured. Technically, the surface is an ensemble of electrically heated ohmic resistors whose electrical resistance and power dissipation can be measured with a definite spatial resolution. Measuring the potential difference Δϕ and the electric current *I* in each HETSS unit the dissipated power can be determined from the product (Δϕ – *I*) of the two locations, while their ratio (Δϕ/*I*) is the resistance between them, which depends on the temperature. The measured power release and the detected local resistance correspond in principle to the local heat transfer coefficient α, which is detected using this method. In order to measure this quantity several aspects have to be fulfilled. The surface resistor must be thin enough to ensure a large heat resistance in longitudinal direction and it must be backed by a thermal insulation in order to direct most of the heat through the liquid via the structural material.

The local heat transfer coefficient α does not only depend on the local cooling capabilities of the flow but also strongly on the distribution of the heat flux density. Therefore, a sophisticated design of the foil shape is required in order to attain the heat flux distribution desired. Figure 11.6.2 illustrates the operation principle of a HETSS element.

Figure 11.6.2. (a) Technical sketch of a HETSS element used in the KILOPIE-MEGAPIE experiment. (b) Measurement principle of a HETSS element [Platnieks, *et al*., 2000].

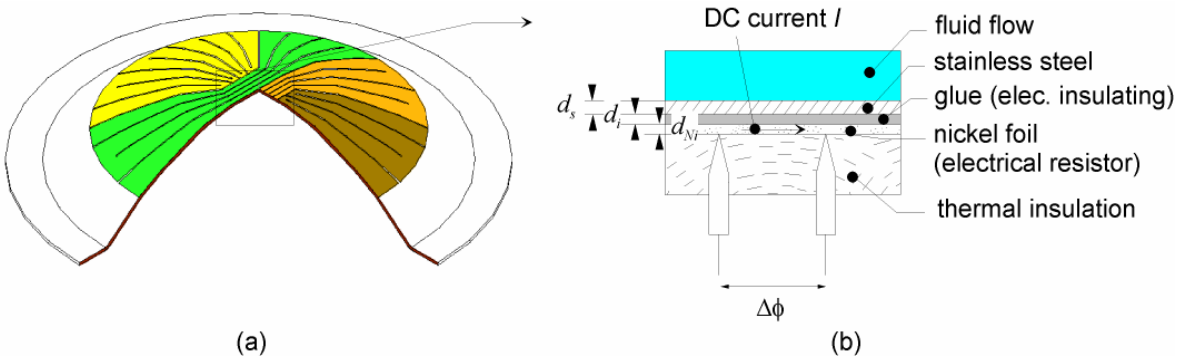

The time dependent temperature $T(t)$ between two discrete points m and n of a segment of a HETSS element can be calculated:

$$T_{m,n}(t) = \frac{\dfrac{\phi_{m,n}}{\phi_m / k_m} - r_{m,n} \cdot \dfrac{T}{T_0}}{\alpha \; r_{m,n} \dfrac{T}{T_0}} - \frac{\phi_{m,n} \cdot \phi_m}{A_{m,n} \cdot k_m} \cdot \left(\frac{d_i}{\lambda_i} + \frac{d_S}{\lambda_S} \right) \tag{11.103}$$

Herein, $\phi_{m,n}$ is the measured potential difference between the discrete points m and n, ϕ_m the potential at m, k_m the instrument resistance, $r_{m,n}$ the unheated HETSS unit resistance between the points m and n, T/T_0 the ratio of the bulk temperature and the temperature of the unheated HETSS, $A_{m,n}$ the surface of the HETSS unit between the points m and n, $d_{,i}$ the thickness of the insulation and λ_i its heat conductivity and finally $d_{,s}$ is the thickness of the steel and its corresponding heat conductivity λ_s. The unheated HETSS unit resistance and the reference temperature are given by the following time integration:

$$r_{m,n} = \frac{1}{\tau} \int_{t=0}^{t=\tau} \left[\left(\frac{\overline{\phi_m}}{\phi_m(t)} \right)^2 \cdot \left(\frac{\phi_{m,n}(t)}{\phi_m(t)/k_m} - \frac{\overline{\phi_{m,n}}}{\overline{\phi_m}/k_m} \right) \Big/ \left(\left(\frac{\overline{\phi_m}}{\phi_m(t)} \right)^2 - 1 \right) \right] \; d\tau \quad ; \tag{11.104 a,b}$$

$$T_0 = \frac{1}{\tau} \int_{t=0}^{t=\tau} T(t) \; d\tau$$

Eqs. (11.103) and (11.104) reveal drastically the difficulties using the HETSS technology as a measurement tool. Besides the tremendous effort needed for the calibration of the device and the rather exact fabrication know-how the following uncertainties has to be quantified:

- accuracy of the measurement chain;
- detailed knowledge of the heat transport trough the glue and the steel;
- heat losses through the environment and tangential to the foil (electric, convective and radiation losses;
- wetting behaviour of the liquid through the steel wall.

Despite these difficulties the HETSS technology represents a non-intrusive method to measure local temperatures and moreover allows simulating various heat loading scenarios of surfaces as they may appear in nuclear or chemical engineering applications, *c.f.* [Patorski, *et al*., 2001].

A challenge in context of the HETSS is the fabrication technology. In order to attain sufficiently high heat fluxes (up to 50 W/cm^2) a thin nickel foil (around 50 μm thick) is glued to a 0.5 mm thick steel dish and is heated electrically by a DC current. The nickel heating foil can be specifically tailored, which allows to simulate different heat release scenarios. In order to get accurate results from the HETSS the element should employ adiabatic conditions to the ambient except for the test port. This can be achieved by a vacuum chamber or by an appropriate thermal insulation. The electric signals from the HETSS are obtained by pin contacts touching the nickel foil at discrete positions delivering a potential to the data acquisition. From these values the local heat flux can be calculated and the local temperature can be determined. Finally, the estimation of local convection heat transfer coefficient α is a result of ratio of the local heat flux to the difference of local surface temperature to the bulk temperature of the adjacent fluid. The spatial resolution perpendicular to the strips in the central part

of the foil is equal to the width of the strip. For a typical digital (16 bit, 1 digit = 40 μV) measurement equipment and appropriate integration time, the accuracy of the measurement in the middle can be predicted to approximately ±1% and at the periphery of the nickel foil to about ±10%.

11.7 Level meters

11.7.1 Direct contact sensors

The simplest system to detect a level in a container are simple electrode contact switch. Two states can be measured by using this system, namely if the contact height is arrived or not.

These kinds of systems are mostly simple self made constructions. The contact electrode technique takes advantage of the good electrical conductivity of the liquid metal. If an initially open electric circuit stressed by a voltage of 24 V is closed the moment where the liquid metal surface contacts the spike of the electrode the potential decreases. This can be captured by a reference circuit an gives the digital signal. In order to gather more information about the actual liquid level, it is necessary to install an array of these filling level meters or to traverse the level meter. A sketch of such a level meter and a photograph of a spark electrode are shown in Figure 11.7.1.

Figure 11.7.1. (a) Sketch of a spark electrode to detect a defined liquid metal level within a container and photograph of a level electrode used in the KALLA laboratory of FZK. (b) Swimmer arrangement to detect the level height using an electric potentiometer.

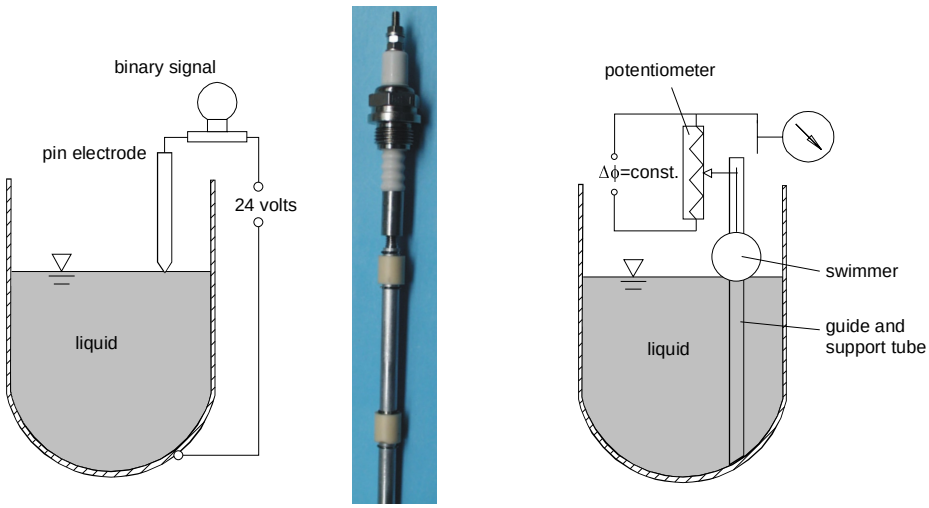

Other direct contact systems are swimmers, in which a lighter body is immersed in the container. Due to the high density of heavy liquid metals like, lead and its alloys, mercury, InGaSn and others different solutions are possible. The swimmer may be directly attached to a shaft connected with a resistive electronics or it may contain a magnet transmitting the level to a senor outside. The out put of such systems show a continuous signal which is proportional to the height of the liquid metal level within the container. A schematic drawing of a swimmer arrangement is shown in Figure 11.7.1(b). The advantage of the swimmer and the electrode systems is that they are cheap and reliable, because in such arrangements the detection system is decoupled from the high temperatures and the corrosive properties of the liquid.

Other direct level measurement methods are differential pressure gauges mounted to the container in such a way that one bore is connected to the bottom and the other branch is in the gas atmosphere above the liquid level. The liquid level corresponds to the measured pressure difference Δp in the way:

$$\Delta p = \rho \cdot g \cdot \Delta h \tag{11.105}$$

where ρ is the fluids density, g the gravity constant and Δh the liquid level height. This method is preferred especially for heavy liquid metals which have high density. A principal sketch is shown in Figure 11.7.2.

Figure 11.7.2. Level measurement using differential pressure gauges

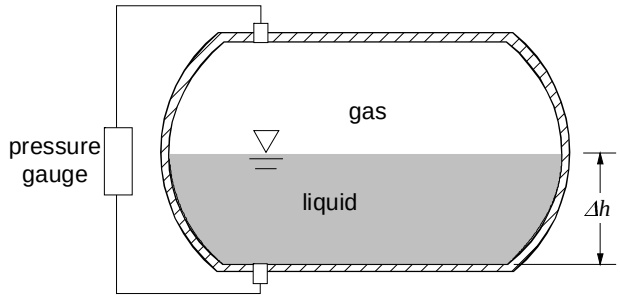

Another option to measure the liquid level in a container is offered by the bubbling technique, successfully performed in the CIRCE loop of ENEA. Here, bubbles of inert gas are injected via a Venturi tube into the liquid. While measuring the gas pressure in the bubble tube, the level can be recorded at the discrete position using only one sensor, which is not in direct contact with the liquid and thus temperature limitations for the use of such a kind do not exist. However, this type of level meter requires a calibration for the specific type of orifice at the outlet of the venture tube. Moreover, a simultaneously measuring thermocouple at the outlet of the tube is required accounting for the surface tension difference between the gas and the liquid at the different temperature levels. The technical realisation in a test–stand at the CRICE facility of ENEA is shown in Figure 11.3.1(c).

Other direct contact sensor types are ultra-sonic sensors connected to the volume of interest from underneath. For heavy liquid metals melting at temperatures above 120°C wave guides are necessary to decouple the ultra-sonic sensor from the hot medium. Generally, for this purpose two types of level and distance instrument are used in process industries: continuous and binary instruments. Both can be realised with ultrasound reflection techniques applying Eq. (11.106)

$$c = \lambda \cdot f = \frac{\Delta x}{\Delta t} \tag{11.106}$$

where c is the sound speed, λ the wave length, f the frequency, Δx the path length and Δt the transit time. The time of flight (TOF) Δt of a pulse sent by the device and reflected from the surface (or object) is measured and c is known. Often the propagation of ultrasonic waves in air or inert gas is used. Then compensations for temperature and speed of sound changes due to vapours are needed. In dependence on the ultrasonic frequency (most devices work with ultrasonic frequencies from around ten to a few hundred kilohertz) a measurement range from millimetres to a few metres can be realised. Distance sensors operating in gas and using broadband ultrasonic transducers achieve a high local resolution in the direction of sound propagation. Accurate measurements down to a resolution of 0.25% can be expected. In latest developments of distance sensors with extremely high resolution, techniques of scanning acoustic microscopy are exploited [Kim, *et al.*, 1999].

In many conventional ultrasonic distance sensors simple comparator circuits are used to detect the arrival of the reflected signal in a specific time window. Such distance sensors are employed in the automation of industrial processes, for example the positioning of work pieces, as well as in the chemical industry. Level measurement becomes difficult when more than one object creates echoes or the surface is rapidly changing its level, e.g. in case of a draining. For this reason intelligent ultrasonic sensors have been developed in the past, which have the capability to evaluate partial echoes in complex echo profiles. In [Eccardt, *et al*., 1995] a concept of signal processing for an intelligent distance sensor and its realisation is described. The main point is to separate real target echoes from misleading echoes by evaluating a set of suitable rules. Fuzzy logic techniques are used. The results are very important for level measurements. The spectrum of ultrasonic distance or level sensors reaches from relatively simple configurations to intelligent sensor systems. Endress & Hauser (Switzerland) has with the Prosonic system a large variety of continuous liquid/solid level instruments and limit switches on the market. Milltronics (Canada) offers a wide spectrum of level instruments; Honeywell (USA) offers distance and proximity sensors. Lundahl (USA) sells programmable ultrasonic sensors, which can be used for most level and presence detection applications. Many other producers are also on the market. Continuous ultrasonic level instruments compete with hydrostatic, radar and float technologies. About 20% of the level instruments are based on ultrasound. It is expected that the market share of ultrasonic instruments will increase since ultrasound is non-intrusive and the technology is well accepted. However, in the future radar techniques will gain more importance for the reasons of higher accuracy and dropping costs [Hauptmann, *et al*., 2002].

In the context of liquid metal application for the level detection the ultrasound technique was put in the direct contact sensor class, since especially in heavy liquid metal systems often a very clean atmosphere is used. In order to achieve this often the loop systems are filled against vacuum. In a vacuum, however, no acoustic signal can be transmitted and thus here a direct coupling to the medium via a waveguide is required [Zhmylew, *et al*., 2003].

11.7.2 Non-intrusive level sensors

Non-intrusive methods for the level detection in a container can be principally based on optic, acoustic, electromagnetic or nuclear methods. Since nuclear methods in terms of X-ray, γ-ray or neutron tomography are extremely expensive due to the high attenuation especially of heavy liquid metals, they are mostly not used to acquire the level height within a container. But, in principle this technique can also be applied for level measurement. The relations to detect the surface height are in principle given for these techniques in Section 11.5.2 for void measurement systems. In this context we concentrate ourselves on measurement principles based electromagnetic waves and radar waves. The optic sensors to detect surface waves are presented in the context of surface shape detection in the following chapter.

11.7.2.1 Electromagnetic level sensors

One of the simplest electromagnetic level sensing tools is based on the electromagnetic induction. Assume two plane parallel arranged coils, in which one is AC powered by a constant sinusoidal potential supply, the adjacent coil passive coil detects the sinusoidal excitation with a certain amplitude, depending on the distance between active and passive coil. The detection amplitude rapidly decreases if a well electrically conducting fluid rises in the container. Amplitude decrease is directly proportional to the height of the liquid level in the vessel. Such a system is schematically depicted in Figure 11.7.3, in which in an open tube two coils are inserted. For the level detection purpose mostly the support tube configuration is used, but, the support tube can also be placed directly in the neighbourhood of the

Figure 11.7.3. Sketch of an electromagnetic level meter used for sodium and lead-bismuth application in KALLA

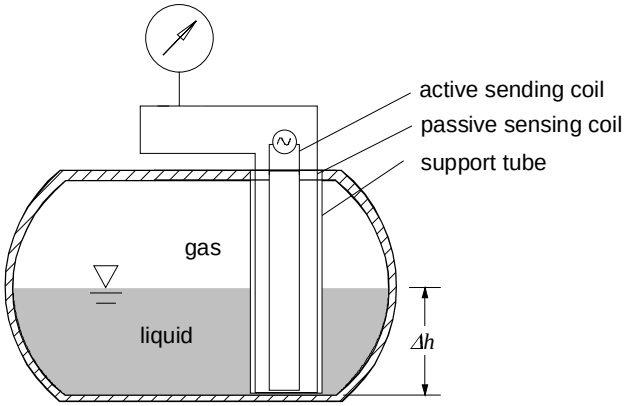

container. Then, however, the sensitivity of the device has to be calibrated new and is of course less than in the support tube configuration. Typically excitation frequencies of 45-400 Hz are used. In order to save money of a fast data acquisition system often the RMS value of the sensing coil is taken and subtracted from constant other potential in order to attain a level monitoring from 0% to 100%. Due to the decoupling of the sending and sensor device from the medium it can be used for arbitrary temperature ranges. In sodium such level meters worked up to 700°C, see [GEC Energy Systems, 1981]. Recently they have been set into operation in the THESYS loop of KALLA.

11.7.2.2 Radar distance measurement

The easiest way to measure the range of an object is to broadcast a short pulse of radio signal, and then time how long it takes for the reflection to return. The distance range R is one-half the product of round trip time τ (because the signal has to travel to the target and then back to the receiver) and the speed of the signal.

$$R = \frac{c_0 \cdot \tau}{2} \tag{11.107}$$

where c is the speed of light in a vacuum. Since the speed of light is relevant the round trip times are very short. For this reason accurate distance measurement were difficult until the introduction of high performance electronics, with older systems being accurate to perhaps a few %. The receiver cannot detect the return while the signal is being sent out – there is no way to tell if the signal it hears is the original or the return. This means that a radar has a distinct minimum range, which is the length of the pulse divided by the speed of light, divided by two. In order to detect closer targets you have to use a shorter *pulse length*.

A similar effect imposes a specific maximum range as well. If the return from the target comes in when the next pulse is being sent out, once again the receiver cannot tell the difference. In order to maximise range, one wants to use longer times between pulses, the *inter-pulse* time. These two effects tend to be at odds with each other, and it is not easy to combine both good short range and good long range in a single radar. This is because the short pulses needed for a good minimum range broadcast have less total energy, making the returns much smaller and the target harder to detect. One could offset this by using more pulses, but this would shorten the maximum range again. So each radar uses a particular type of signal. Long range radars tend to use long pulses with long delays between them,

and short range radars use smaller pulses with less time between them. This pattern of pulses and pauses is known as the pulse repetition frequency (PRF), and is one of the main ways to characterise a radar. As electronics have improved many radar systems now can change their PRF.

Another form of distance measuring radar is based on frequency modulation. A frequency comparison between two signals is considerably more accurate, even with older electronics, than timing the signal. By changing the frequency of the returned signal and comparing that with the original, the difference can be easily measured. In these systems a "carrier" radar signal is frequency modulated in a predictable way, typically varying up and down with a sine wave or saw-tooth pattern at audio frequencies. The signal is then sent out from one antenna and received on another, and the signal can be continuously compared. Since the signal frequency is changing, by the time the signal returns to the aircraft the broadcast has shifted to some other frequency. The amount of that shift is greater over longer times, so greater frequency differences mean a longer distance, the exact amount being the "ramp speed" selected by the electronics. The amount of shift is therefore directly related to the distance travelled, and can be displayed on an instrument. This signal processing is similar to that used in speed detecting Doppler radar.

Usually radar systems to detect levels are made for the petrochemical industry, where large containers appear. In liquid metal systems with small dimensions the frequencies or the pulse repetition frequencies required to detect level distances in the range of millimetres are in the range of 15-300 GHz. Nevertheless using the frequency modulation technique a first test with a cheap sensor showed reasonable results with an accuracy of ±2 cm compared to a pressure gauge system.

11.8 Free surface measurements

In many nuclear applications heat fluxes appear causing temperatures beyond the sustainable limit of any structural material. A prominent example is the development of the free surface target for the planned international material irradiation facility IFMIF, where accelerated neutrons (>14 MeV) are shot directly on a lithium target, see e.g. [Ida, *et al*., 2002], [Jameson, *et al*., 2004] or [Ida, *et al*., 2005]. Another example also using a free lithium target is the SUPER FRS target planned to set into operation at GSI [Geissel, *et al*., 2003]. There, a pulsed uranium ion beam is accelerated and fragmented in a gravity driven vertical lithium jet. Regarding the nuclear heavy liquid metal application for waste transmutation the MYRRHA target is one of the examples of a free surface lead-bismuth cooled target, see e.g. [Abderrahim, *et al*., 2001].

Except for the nuclear application especially the metal casting companies face the problems of the instabilities occurring during the manufacturing process. As an example during the steel and alumina casting wavy surfaces can establish while the liquid metal flows in direction of the gravity field. If the wavy surface solidifies in an undesired manner the subsequent manufacturing process is significantly disturbed.

Therefore, techniques are required which allow to monitor and to control free surface flows. As liquid metals are opaque, corrosive and operate in most cases at relatively large temperatures, the discussion in this chapter concentrates mainly on non-intrusive optic or acoustic measurement devices.

11.8.1 Optic methods

One of the problems of liquid metals is that their optical reflection coefficient is close to one, which means that they are totally reflecting. This causes in most cases difficulties in using highly sensitive optical distance measurement methods. Commercially available photo-multipliers, in particular, are

too sensitive for a totally reflecting material. But, some of the liquid metals show wave length regimes, in which the reflectivity is significantly reduced. For example liquid lead has a reflectivity of 0.94 at a wave length of $\lambda = 900$ nm. At $\lambda = 584$ nm corresponding to yellow light the reflectivity is decreased to 0.62, but it increases to 0.92 at $\lambda = 500$ nm again [Blaskett, 1990]. Making use of this behaviour, e.g. by means of using a yellow filter triangulation methods, can be used. Consequently, before any optic method is used a detailed literature study or pre-experiments should be performed in order to take advantage of the individual properties of the metal used in the experiment.

The basic principle of active non-contact range-finding devices is to project a signal (radio, ultrasonic or optical) onto an object and to process the reflected or scattered signal to determine the distance. If a high resolution rangefinder is needed, an optical source must be chosen because radio and ultrasonic waves cannot be focused adequately. In addition to absolute distance measurement, laser range finding devices are traditionally used for 3-D vision, dimensional control, positioning or level control. Optical distance measurement methods can technically be put into three categories: interferometry, time-of-flight and triangulation methods. Considerable progress has been achieved during recent years by understanding the basic physical and information theoretical principles of range sensing. It appears advances in the design of lasers, integrated optics devices, emitter and receiver electronics will lead to further interesting developments. In this context, some laser range-finding techniques for industrial applications are briefly presented: triangulation, pulsed time-of-flight (TOF), phase-shift measurement and frequency-modulated continuous wave (FMCW) modulation. All these approaches are still further developed because the choice of the technique to be used depends mainly on the required application. Moreover, each of them presents limitations, which are discussed here.

Many applications do not allow contact or alterations to an object or surroundings to suit the measurement system, e.g. by changing the reflectivity of the surface with paint. These non-contact measurement techniques have found widespread use in heritage, environment modelling, virtual reality, robotics and many industrial fields. The true problem of these methods remains the fast and precise acquisition of the depth map with a large volume and in a natural environment. The most critical parameters of such systems are the depth measuring range z and the depth resolutions δz. Figure 11.8.1 illustrates the measuring and resolution ranges that are covered by the existing industrial measuring systems. The highest absolute resolutions are achieved by interferometry, which reaches accuracies of $\lambda/100$ and can measure ranges up to 10 m using multi-wavelength techniques. Active triangulation can be used with high resolution from the millimetre range up to several meters. Here the accuracy depends mainly on depth of field and can be as high as 10 μm for small depths.

Figure 11.8.1. Relative resolution of methods for optical shape and distance measurements from [Simoni, *et al*., 2002]

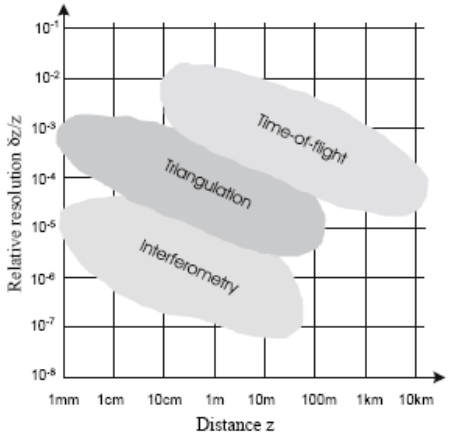

Finally, time-of-flight techniques allow measurement of depths in the range from tens of mm up to tens of km [Simoni, *et al*., 2002]. Here the depth estimation is an extreme challenge for time measurement and accuracy, being mainly dependent from mechanical and electronic drifts and independent from distance, is of the order of some mm.

The surface shape of liquid metal films can be imaged and digitised using the following basic components: a light source to define a specific pixel(s), such as an encoding-decoding process (e.g. triangulation, fringe and pattern projections and time of flight), a sensing device composed of a collecting lens and a photo detector that converts light energy to electrical signal, an analogue-to-digital converter, and finally a computer to process, display, and store the raw data [Rioux, *et al*., 1989].

The following reviews the basic concepts behind optical triangulation for three-dimensional digitising applications. It emphasises the critical elements of optimal design and the limitations related to the use of coherent light. It is shown, for example, that speckle noise is a fundamental limit for the position sensing of laser spot centroid. This has an impact on the choice of the position sensor geometry.

Of crucial importance is the choice of the light source. Conventional light sources can and are used for optical triangulation, but laser sources have unique advantages for 3-D surface imaging. One of these is brightness, which cannot be obtained by an incoherent emitter. Another is the spatial coherence that enables the laser beam to "stay in focus" when projected on the scene. Nevertheless, this property is limited by the law of diffraction, which is written here as the propagation (along the *z* axis) of Gaussian laser beams:

$$\omega(z) = \omega_0 \cdot \left[1 + \left(\frac{\lambda \cdot z}{\pi {\omega_0}^2} \right)^2 \right]^{\frac{1}{2}} \tag{11.108}$$

and, defining depth of field D_f using the Rayleigh criterion gives:

$$D_f = 2 \cdot \pi \cdot {\omega_0}^2 / \lambda \tag{11.109}$$

which shows that the depth of field D_f is larger when the laser wavelength λ is small (toward the blue) and/or when the laser beam spot size ω_0 is large. A detailed analysis is given in [Rioux, *et al*., 1987].

11.8.1.1 Optical triangulation

On scattering, the spatial coherence of the laser light is lost, which means that the depth of field used at the projection can be useful only if the lens aperture is closed down at the collection. Otherwise the focused laser spot is imaged as a blurred disk of light on the photo-detector. A solution to this problem is to modify the conventional imaging geometry to conform to the Scheimpflug condition.

Essentially this geometry enables the photo detector surface to "stay in focus" with the projected laser light. Its construction is very simple when the focal planes of the lens are used. A typical triangulation measuring geometry is shown in Figure 11.8.2. A finely collimated laser source is used to probe the scene or object of interest. The probe works in continuous wave (CW) mode. A portion of the back-reflected light is focused onto a linear position sensitive device, PSD, placed at a fixed distance d from the laser module. Indeed, it is known that a point on the projection axis located at *f* (point *A*) will be imaged at infinity. Consequently the inclination angle of the photo-detector is defined

Figure 11.8.2. (a) Optical triangulation measurement geometry.
(b) Sepckle noise limits the position sensing resolution.

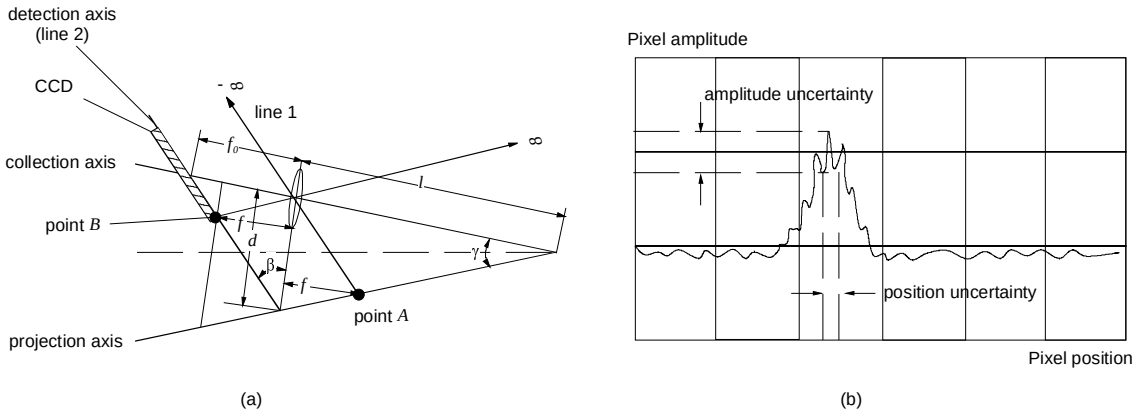

by drawing a line between that point and the principal point of the collecting lens (line 1). Similarly, on the other side of the lens, one knows that a point at infinity will be imaged at a distance *f* from the lens. The inclination and position of the photo detector are then obtained by constructing a line (line 2) parallel to line 1 passing through the point *B*.

The position of the laser spot on the PSD is related to the distance of the object by the relation:

$$z = \frac{d \cdot f_0}{p + f_0 \tan\gamma} \tag{11.110}$$

where d is the distance between the collecting optics and the laser, f_0 is the focal length of the collecting optics, p is the spot position on the sensor, and γ is the deflection angle of the laser beam.

The accuracy in the distance measurement depends on depth and on the ability to define the spot position on the PDS. A simultaneous collection of chromatic information is also possible by using an RGB laser and splitting the back-reflected light into its colour components by means of a diffracting element, see e.g. [Baribeau, *et al.*, 1992] A complete three-dimensional data set is obtained by scanning the laser beam in a raster mode over the object or scene of interest.

Sampling the shape along the *x* and the *y* axes is usually done in a straightforward manner [time or space interval, depending on the geometry of the photo detector(s)]. Sampling along the third dimension (*z* axis) often requires image pattern centroid location and interpolation. This is where coherence shows its limitation. Indeed, because of the coherent nature of the laser projection, the imaged laser spot on the photo detector(s) is corrupted with speckle noise. Here again, the geometry of the optical system and the wavelength of the light are the parameters.

Figure 11.8.2(b) shows how speckle noise adds to the uncertainty of an imaged laser spot. The origin of the modulation observed in the profile is related to the scattering of a pure wavelength when diffusion occurs at the surface of the object. Within the projected laser spot, each scatterer can be regarded as a coherent emitter, and because there are many of them within the area of illumination the resulting image is the coherent sum of spatially incoherent sources. The result is a random modulation multiplying the expected smooth light profile. [Baribeau & Rioux, 1991] formulated the relationship between the geometrical parameters as:

$$\sigma^2 = \lambda^2 f_0^2 / 2\pi(\phi\cos\beta)^2 \tag{11.111}$$

where σ^2 is the position variance, λ the wavelength of the laser light, f_0 is the lens-CCD distance on the optical axis, ϕ is the aperture of the collecting lens, and β is the Scheimpflug angle. When typical values are given for each parameter, the centroid uncertainty is found to be of the order of a few micrometers, and more interesting, the physical dimensions of the photo-sensor elements have no effect on that limit. Consequently, the larger the photo-sensors, the better are the performances of the 3-D digitiser in terms of sensitivity, speed, and depth of view. In practice, using wider photo-sensor elements means that the interpolation is done over a wider dynamic range. As an example, if the speckle noise limits is at 2 mm and the photo-sensor width is at 16 mm, one requires only 5 bits of numerical interpolation. On the other hand, if the photo-sensor width is 50 mm, 7 bits of interpolation are required. Notice that at least 2 bits are added to the ratio to reduce quantisation (or numerical) noise to a negligible level.

Some concluding remarks

Digitising shapes requires careful design consideration. For all active approaches including optical triangulation, the most critical element in order to achieve high-resolution imaging is the projection system, not the collecting system. In fact, in some cases it is found that optimum performances are obtained where the photo-sensor elements are of larger sizes. This is quite the opposite the case if only two dimensions are of interest, there only the use of a small sensor ensures a high location sensitivity.

11.8.1.2 Time-of-flight distance measurement

11.8.1.2.1 Pulsed TOF method

The laser pulse time-of-flight (TOF) distance measuring technique was originally used in military and surveying applications. It refers to the time it takes for a pulse of energy to travel from its transmitter to an observed object and then back to the receiver (t_d). If light is used as energy source, the relevant parameter involved in range counting is the speed of light (~roughly $c = 30$ cm/ns). A TOF system measures the round trip time between a light pulse emission and the return of the pulse echo resulting from its reflectance off an object. Using elementary physics, distance is determined by multiplying the velocity of light by the time light takes to travel the distance. In this case, the measured time is representative of travelling twice the distance and must, therefore, be reduced by half to give the actual range to the target. To obtain 1 mm accuracy, the accuracy of the time interval measurement should be 6.7 picoseconds.

Since a single pulse is adequate for the unequivocal determination of distance with centimetre precision and accuracy depends only weakly on distance, this method is particularly appropriate, for example, in applications involving distances longer than 1 m, applications where reflectors are not used and fast measurement applications such as scanning. In addition, averaging enables millimetre or even sub-millimetre precision to be achieved. The advantage of the TOF system arises from the direct nature of its sensing as both the transmitted and returned signals follow essentially the same direct path to an object and back to the receiver. To achieve these goals, the basic building blocks of a TOF range finder have to be realised in the form of high-performance integrated circuits. [Bosch & Lescure, 1995] provide an excellent review of absolute distance measurement in one of the SPIE Milestone volumes.

Principle set-up

A pulsed TOF distance measuring device consists of a laser transmitter emitting pulses with a duration of 5 to 50 ns, a receiver channel including a *p-i-n* or an avalanche photodiode, amplifiers, an automatic gain control (AGC) and timing discriminators. The emitted light pulse (start pulse) triggers

the time interval measurement unit, and the reflected light pulse (stop pulse) stops it. The distance to the target is proportional to the time interval. A block diagram of a laser range finder is shown in Figure 11.8.3(a).

Figure 11.8.3. (a) Block diagram of a TOF laser range finder operating in the pulsed mode. (b) Timing jitter and walk.

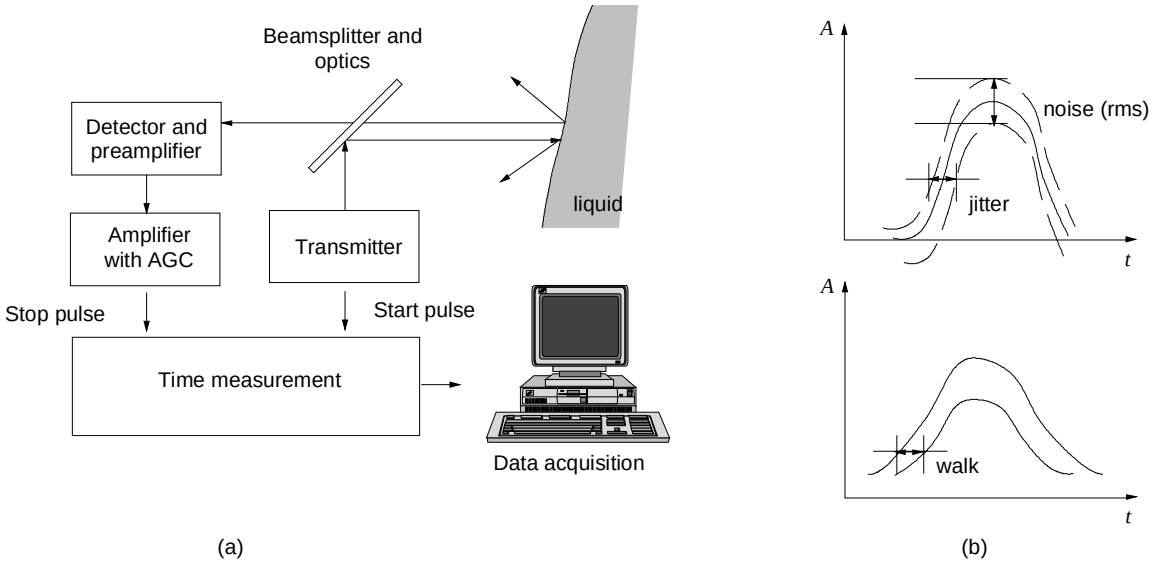

The selection of laser type depends on the intended measurement range and the required speed. For laboratory purposes with small distance fast repetition frequencies are required. This restricts the choice of the laser to laser diodes, which are capable to be used at rates of tens of kilohertz, the DH type even reaches the Megahertz level [Amann, *et al*., 2001].

Problems of pulsed TOF measurements: Time jitter and walk, non-linearity and drift

The main sources of inaccuracy in laser rangefinders are noise-generated timing jitter, walk, non-linearity and drift. Typical noise sources include noise generated by the electronics, shot noise caused by the background radiation induced current and shot noise created by the noise of the signal current. Jitter in timing determines mainly the precision of the range measurement. The amount of timing jitter is proportional to noise amplitude (root mean square ~rms) and inversely proportional to the slope of the timing pulse at the moment of timing (du/dt). A single-shot resolution of 1 cm can typically be achieved with a good signal (SNR = 100, signal to noise ratio) using the 100 MHz bandwidth of the receiver channel. However, precision deteriorates as the distance increases and the pulse amplitude decreases proportional to the square of the distance [Määttä, *et al*., 1993]. Pulse amplitude and shape variations create timing error in the time-pickoff circuit and that error is called walk error. Jitter and walk in leading edge timing are shown in Figure 11.8.3(b).

The time discriminator is a very important part of a precision time measurement system. The task of the discriminator is to observe time information from the electric pulse of the detector preamplifier and to produce a triggering signal at the right instant. The choice of time derivation method depends on the desired time resolution, counting rate and required dynamic range of the pulse. Commonly used principles in discriminator design include leading edge timing (constant amplitude), zero crossing timing (derivation), first moment timing (integration), and constant fraction timing. Constant fraction discrimination (CFD) compensates with idealised pulse shapes for walk caused by both amplitude and

rise time and is commonly used in the TOF measuring units of laser range finders. The principle behind the operation of CFD is the search for an instant in the pulse when its height bears a constant ratio to pulse amplitude. The occurrence of this point produces a triggering pulse. The constant fraction instant can be examined with a high gain differential emitter-coupled logic (ECL) comparator, which amplifies the difference of the attenuated and the delayed pulses [Maier & Sperr, 1970]. CFD compensates for walk caused by amplitude and rise time, but not for walk caused by non-linear shape variations. Zero crossing and first moment timing compensate for amplitude variations, while leading edge timing fails to compensate for any variation described.

The transmitter, gain-control and time-interval measurement units are also critical for the accuracy of the system. The transmitter should be able to produce a stable laser pulse shape. This may call for the temperature stabilisation of the diode. The dynamic phenomena of the laser diodes, relaxation oscillations, should also be considered when designing the pulsing scheme as they may easily lead to significant changes in laser pulse shape. Gain control is needed to adjust the dynamics of the timing pulse to that of the timing discriminator. The amount of control needed depends on the measurement range, construction of the optics and reflectivity variations of the object. An adjustable optical attenuator at the receiver optics can be used to realise gain control. The advantage of this method over electrical gain control is its delay stability over a wide control range. Recently, the dynamic range of electronic gain control methods has increased quite remarkably, [Ruotsalainen, *et al*., 1999]. The time interval between the start and stop pulses is measured with the time-to-digital converter (TDC), which is a fast, accurate and stable time-interval measuring device that uses, e.g., a digital counting technique together with an analogue or digital interpolation method [Räisänen, *et al*., 1998]. The single shot resolution of the TDC is typically better than the noise generated timing jitter.

The final precision of the distance measurement can be greatly improved by averaging, with the improvement being proportional to the square root of the number of results averaged. Thus, by averaging 100 successive measurements, the final resolution can be improved to the tenth of millimetre level, the corresponding measurement time being 1 ms with a pulsing rate of 100 kHz, for instance. If the statistical error is averaged to a negligible level, the accuracy of the system is defined by its systematic errors such as nonlinearity in the time interval measurement scale and drift.

11.8.1.2.2 TOF laser phase-shift distance measurement

In a phase-shift distance measurement device, the optical power is modulated with a constant frequency. The basic operating scheme of the device is shown in Figure 11.8.4. A sine wave of frequency f_{rf} generated by the main oscillator modulates the dc-current of the laser diode. After reflection from the target, a photodiode collects a part of the laser beam. Measurement of the distance D is deduced from the phase shift $\Delta\phi = 2\pi \cdot f_{rf} \cdot \Delta t$ between the photoelectric current and the modulated emitted signal:

$$D = \frac{1}{2} c \frac{\Delta\phi}{2\pi} f_{rf} \tag{11.112}$$

where c is the speed of light in free space and Δt the time of flight (TOF).

When $\Delta\phi = 2\pi$, the unambiguous distance measurement is limited to $\Lambda = c\, f_{rf}/2$. To ameliorate the accuracy of this set-up, the phase shift is not directly measured at the working high frequency but at an intermediate frequency $f_{rf} = |f_{rf} - f_{ol}|$ using a heterodyne technique that preserves the phase shift versus distance. The signals of the two mixers outputs are filtered by a passband circuit tuned on f if and with a Δf_{if} bandwidth.

Figure 11.8.4. Block diagram of a phase shift laser distance measurement using a heterodyne technique

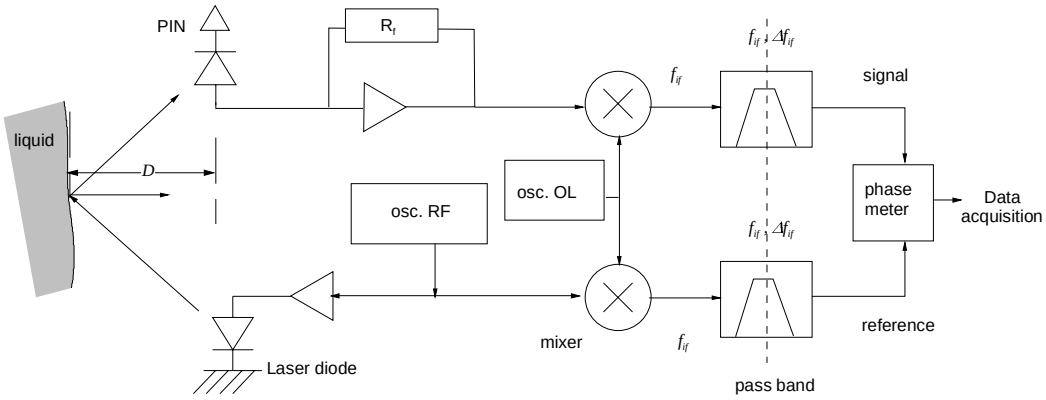

When the target area is as large as the area illuminated by the transmitter, the received signal power P_R is given by the relationship:

$$P_R = T_T \cdot T_R \cdot \frac{\rho_d}{\pi} \cdot P_0 \cdot \cos\theta \frac{A_R}{D^2} \tag{11.113}$$

where P_0 is power output of the laser diode, T_T the collection and transmission efficiency of transmitter, T_R the transmission of the receiver optics, ρ_d the Lambertian reflection coefficient of the fluid, θ the laser beam incident angle on the surface, A_R the area of receiver lenses.

Only the Lambertian component is used for the calculation of the photoelectric signal; the specular component is ignored in Eq. (11.113). As a matter of fact, the term $\rho_d P_0/\pi$ is the power intensity (~ in watts per steradion) reflected perpendicular to the liquids surface. From this equation it becomes obvious that the method is not able to operate a high Lambertian reflection coefficients (>0.8). For the use in liquid metals specific adapted wave lengths of the laser and appropriate filter systems must be applied. Also for these methods a careful error analysis must be performed, which is in principle described below, for a more specified information on this technique the related literature cited gives sufficient information.

Error analysis

a) High levels of the rf channel

The power budget shows that the ratio P_R/P_0 may vary with a factor greater than 1000 if the distance D varies for example from 1 to 10 m. Thus, when the photoelectric signal amplitude varies with a factor 1000, the phase-shift error $\delta\varphi$ introduced by this variation must be less than 0.1° for an error distance measurement δ_D of 2.5 mm. But, with large amplitude of the useful signal, distortion and clipping introduce phase-shift errors. To avoid this error, the first solution is the defocusing of the photodiode, so that it receives less light when measured distances are small. A second solution is increasing the feedback of the mixer to avoid distortion and clipping [Perchet, *et al*., 1997].

b) Intermediate frequency shift

With a low-power laser diode, a narrow bandwidth amplification improves the signal to noise ration (SNR). For a white noise at the input, the output of a pass band second-order filter presents a noise-equivalent bandwidth B_n given by the relationship [Cherry &Hooper, 1968]:

$$B_n = (\pi / 2) \cdot \Delta f_{rf} \tag{11.114}$$

Thus, the rms noise of the useful signal is proportional to the square root of the bandwidth Δf_{if}. Because of symmetry, it can be supposed that the frequency drift δf_{rf} or δf_{ol} of one oscillator balances the drift of the other one. No error is present if the two intermediate frequency filters are identical on reference channel and signal channel. But if the value of the bandwidth is too narrow, we must take into account the device mismatch effects introduced in intermediate frequency tuned circuits by the frequency drifts of f_{rf} and f_{ol}. For example, for Rauch filter structure, the quality factor $Q = f_{if}/\Delta f_{if}$ and the tuned frequency f_{if} mismatches are imposed by the presence of capacitance mismatches.

However, to guarantee the resolution, the best method consists of keeping the value of the intermediate frequency constant by a phase-locked loop technique. In [Payne, *et al*., 1992] and [Goldmann, *et al*., 1997] 20, 100 m distance measurement to a retro-reflector is obtained (~i.e., with a good SNR) with errors of less than 50 μm (!). The stable $f_{\text{rf}} = 1.5$ GHz modulating frequency is generated from the 15$^{\text{th}}$ harmonic of a 100 MHz output of a Rubidium atomic clock.

c) Influence of crosstalk

Electrical crosstalk between the transmitter and the receiver produces another important error. When the photoelectric signal and the modulation current of the laser diode have the same frequency f_{rf} , the synchronous leakage v_{crosst}, arising from the modulation current source, is superimposed on the working photoelectric signal v_{ph}. The two signals are added vectorially. The trans-impedance amplifier associated with the photodiode must be shielded to exclude undesired external signals. However, because the influence of the crosstalk cannot be totally removed with shielding techniques, different methods have been proposed. To remove the effects of this field leakage, the gain switch of a laser diode is used as a light comb generator, and an avalanche photodiode (APD) selects the second harmonic of the photoelectric signal [Seta & Ohishi, 1987]. Another method, based on the use of a Pockels cell, has been proposed to obtain a measured signal at a frequency that is a multiple of the modulation frequency, although its implementation is still rather in its infancies [Lescure, *et al*., 1991].

The crosstalk errors at the modulation frequency f_{rf} determine the minimum signal-to-induction ratio necessary to obtain a given accuracy. For example, to limit the maximum error phase shift $\delta\varphi$ to 0.1°, the amplitude ratio of the photoelectric signal on the leakage signal must be 600 (~55 dB). Because the induced signal is “masked” by the electrical noise, the SNR must be higher than 55 dB. This condition is difficult to satisfy when the frequency modulation f_{rf} of a low-power laser diode is higher than 10 MHz. The maximum distance measurement error δD_{max} is independent from the modulation frequency and increases with the square of the distance, *c.f.* Eq. (11.113). Because the photoelectric current and crosstalk are added vectorially, a periodic error is obtained versus distance *D*. In this way, this error can be compensated. This method was proposed initially by [Müller, *et al*., 1997].

To determine a rough estimation of the crosstalk between the driver laser and the photodiode, a model of fictitious sources of perturbation at the input of the transimpedance amplifier has been proposed by [Bosch & Lescure, 1997]. The coupling is represented by the mutual capacitance and the mutual inductance. These models show the advantage of using an APD. Indeed, the gain of the primary photoelectric current occurs inside the semiconductor crystal itself, and it can be assumed that the crosstalk becomes superimposed on the output signal only when the signal has been amplified. But, as APD areas are small, this gives a small field of view of the receiver. For 3-D vision, if only the laser beam is deflected by micromirrors, a large field of view of the receiver is necessary, when no scanning mirrors are used in the receiver channel. A large *p-i-n* photodiode surface gives such a field

of view. So, the large photodiode capacitance increases the time constant at the input of signal channel, that reduces the bandwidth and/or the phase margin of the transimpedance amplifier. One solution is to compensate the photodiode capacitance by a tuned circuit. This technique is possible because the phase-shift distance device is working at one frequency f_{rf} only.

Some final remarks

Distance measurement by the phase-shift technique is a good method to obtain a resolution of some tens of millimetres with non-co-operative targets. For co-operative targets, i.e. sharp liquid waves, the resolution can be better than 50 μm, with high-frequency modulation. Because the photoelectric current is a sine wave, a photodiode with a large area can be used to achieve a wide angle of the field of view. In this way, it is possible to scan the laser beam by micro-mirrors, enabling compactness and low cost. Nevertheless, this method requires a large angle of view to the liquid metal surface, which is not given in some applications. Moreover, a careful look has to be taken the fluid used in the individual experiment and the corresponding wave length of the laser.

11.8.1.2.3 TOF optical radar

Optical distance measurement with the optical radar technique, often called FMCW technique, has been used in various applications such as non-contact surface profiling, fibre optic sensing, reflectometry, positioning and tomography. The interest in the FMCW technique is due to the large dynamic range and the high resolution, particularly at short range sensing. Because of the recent progress in the area of laser diode technology, high performance FMCW ranging systems can currently be realised with electronically tuneable laser diodes. A comprehensive description of this technique may be taken from the articles of [Beheim & Fritsch, 1983], [Strzelecki, *et al*., 1988], [Slotwinski, *et al*., 1989], [Burrows & Liou, 1990] and [Diekmann, 1994]. Below the operation principle of the FMCW technique is described and the system performance achievable with laser diodes at the current state is discussed.

The principal setup of an optical FMCW radar system is illustrated in Figure 11.8.5(a). The optical power from a frequency modulated laser diode, the instantaneous frequency of which is periodically shifted by Δf, is used as probing signal as shown in Figure 11.8.5(b).

The periodic and linear frequency chirp may practically be performed by applying a saw-tooth bias current to the modulator section of the wavelength-tuneable laser diode. The laser output passes an optical isolator to avoid deteriorations of the laser frequency by reflections and is then sent simultaneously to the object and the reference mirror, and the reflected signals are then superimposed in a square law detector diode. Owing to the detection process that is proportional to power, i.e. the amplitude squared, both signals are mixed in the detector and the main ac component of the electrical output is at the frequency difference f_{if} of the two optical signals. The detector output is fed into an amplifier-limiter so that unintentional amplitude modulation is suppressed. Finally, the intermediate frequency f_{if} of the reflected signals is measured with a frequency counter. Due to the square law mixing process the amplitude of the detector output at f_{if} is proportional to the amplitudes (not the powers) of the object signal and the reference, respectively. Accordingly, the dynamic range of the FMCW technique is twice as large as that of the pulse radar technique, where the electrical signal is proportional to the object signal power.

The distance difference between object and reference mirror R, which is the relevant quantity to be determined, is proportional to f_{if} as indicated in Figure 11.8.5(b). Since the round-trip delay time t of the object signal is given as:

$$\tau = 2R/c \tag{11.115}$$

where c is the light velocity, the intermediate frequency amounts to:

$$f_{if} = \Delta f \cdot \tau / t_m = 2 \cdot \Delta f \cdot R / c\, t_m \tag{11.116}$$

where t_m denotes the ramp period, which is typically of the order 0.1 to 1 ms. Accordingly, the distance sensing is done by an electric frequency measurement (usually in the kilohertz regime), while in the case of the more popular pulse radar, the delay time is measured directly. As the ramp period can be chosen arbitrarily, the FMCW radar can determine t values in the picosecond range, according to millimetre distances R, by simply performing a frequency measurement in the kilohertz regime. Consequently, no high-speed electronic is required to determine delay times even in the subpicosecond range.

Figure 11.8.5. (a) Schematic set-up of an optical radar using a tuneable laser diode as light source. Instantaneous optical frequencies versus time of the object and reference mirror optical signals. (b) In case of a linear optical frequency ramp, the intermediate frequency f_{if} is constant between t_1 and t_2. (c) In case of a non-linear optical frequency ramp, a chirping intermediate frequency occurs.

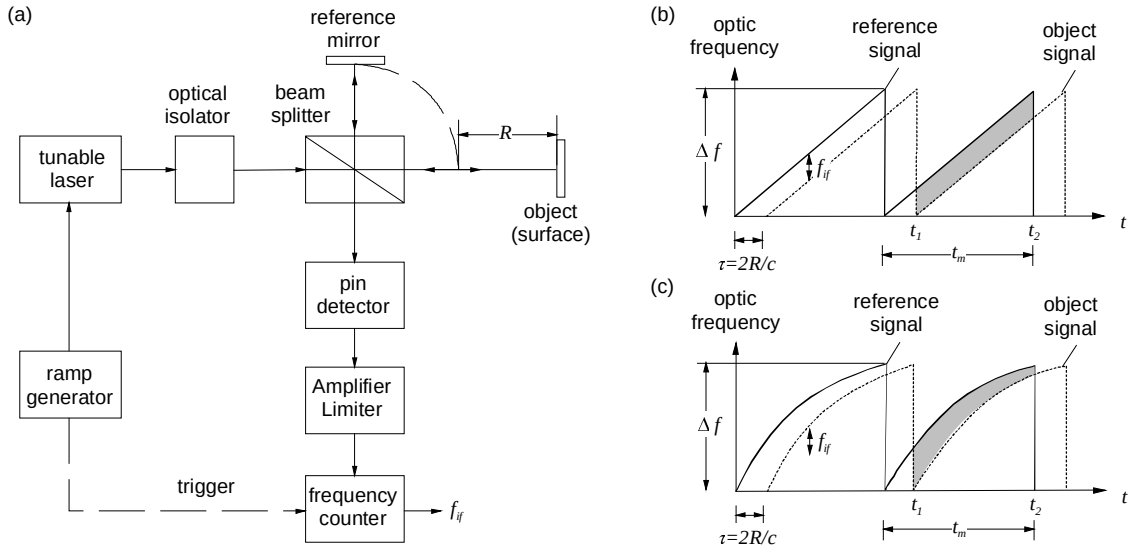

Limitations

Unfortunately, the frequency modulation response of a laser diode is, in general, non-uniform against the modulation frequency, so that a linear optical frequency sweep cannot be realised by a linear modulation of the control current. In addition, the frequency versus control current characteristic is also in general non-linear. As a consequence, deviations from the linear ramp as shown in Figure 11.8.5(c) usually occur that, in turn, lead to a variation of the intermediate frequency f_{if} . While the total phase difference ϕ as indicated by the shaded areas in Figures 11.8.5(b) and 11.8.5(c) is still proportional to τ and the distance R as long as $t << tm$, the variation of f_{if} during each ramp increases the total intermediate frequency bandwidth and, consequently, the noise level that finally limits the accuracy. A usual technique to eliminate the effect of the nonlinear frequency ramp is to use simultaneously a reference Line, so that the ratio of distance R and the length of the reference line is independent of the linearity of the frequency ramp. Various schemes have been presented to linearise the optical frequency sweep of the laser diodes, which commonly utilise a reference delay line to determine the variations of the intermediate frequency f_{if}.

The maximal measurable distance of an optical radar system based on laser diodes is limited by the coherence length of the laser diode. The finite value of the latter, which typically is of the order of several tens of meters is a consequence of the laser diode phase noise that also determines the spectral line width. Correspondingly, laser diodes with narrow line-widths within the frequency sweep range are best suited for the measurement of longer distances.

Experimentally, high resolution in the submicrometer regime has been demonstrated with diode laser FMCW ranging systems [Burrows & Liou, 1990]. Using widely continuously tuneable laser diodes with Δf of 500 GHz, a spectral line width of 25 MHz, and a repetition period t_m of 10 ms, the one-shot relative accuracies for distances of 1 m and 1 cm down to millimetres, respectively, amount to $4.3 \cdot 10^{-5}$ and $2.7 \cdot 10^{-4}$ [Diekmann & Amann, 1995]. These results clearly prove the high performance of this technique for the accurate and fast measurement of short distances and, considering the large modulation bandwidth of laser diodes, make this technique also well suited for 3-D viewing systems.

11.8.1.3 Projection techniques

The demands of the automobile industry to manufacture precise mostly reflecting surfaces in order to allow for a fully automatic production process controlled by manipulators led in the past decade to the development of rapid 3-D surface detection techniques. Most of these techniques are based on projection of the object on an observing CCD camera. An overview and the related literature on new developments in fast 3-D surface quality control can be found in the article by [Leopold, *et al*., 2003]. In general several reflection techniques can be used such as structured lighting reflection, coded lighting or colour lighting. Most of the can only be used to objects at rest. Flowing heavy liquid metals, however, reveal a spectrum of motion on different time scales, which requires a fast acquisition technique. Thus the information to describe the surface is not only a function of the geometry but also of the time.

Due to this fact mostly fringe projection systems are used for acquiring rapidly three-dimensional surface information. These systems are robust against surface texture and reliable. Using fringe projection even objects with large surface gradients and large extensions in the direction of recording can be captured. The fringe projection also allows to measure shapes or films without any gradients, which is impossible using the stereo-matching [Böhm, 2001].

The fringe projection is based on the light sheet technique as principally shown in Figure 11.8.6. A single line is projected on the on the liquid metal film (the object) and observed under another angle by a camera. The deformation of the line yields parallaxis and thus the three-dimensional form along the line. In order to acquire a surface many lines are projected in a dense distance from each other onto the object. In order to obtain a definite information all fringes are not projected simultaneously onto the surface. They are rather projected in a defined time series onto the surface as a binary pattern. Most of the systems used in the manufacturing industry use for the encoding the Gray sequence, in which for *n* lines only *ldn* patterns are projected on the liquid surface. This Gray code sequence solves very roughly the correspondence between the projector co-ordinates and the camera co-ordinate on the pixel level. In order to attain a sub-pixel accuracy another pattern sequence must be projected on the surface. Most efficiently operates the phase shifting technique, which is described below and schematically depicted in Figure 11.8.7, but two general disadvantages of the phase shifting technique should be mentioned in this context.

The phase shift method assumes a sinusoidal representation of the fringe pattern on the sensor (which is the camera), which is not given in a frame based projection system. This yields to measurement errors. The sinusoidal form of the fringe pattern must first be generated. This can be

Figure 11.8.6. Principle of the light sheet and the encoded light sequence with the camera and the projector

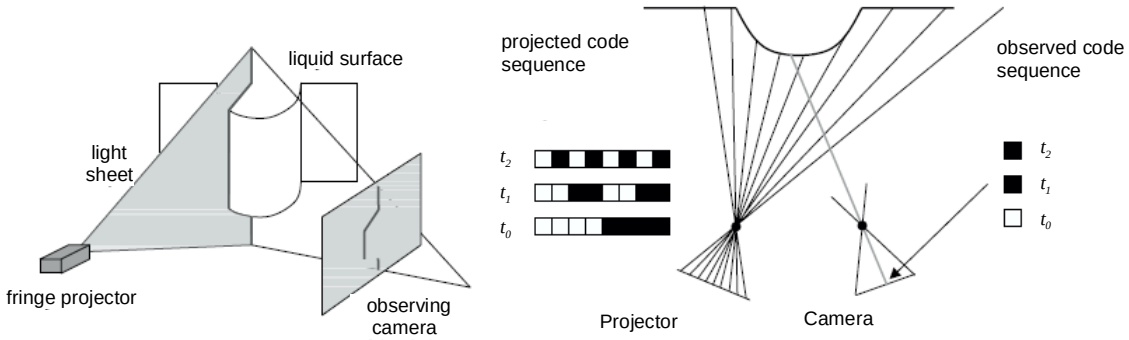

achieved by a defined defocusing of the projection unit. This has the disadvantage that the defocusing only leads in a certain distance of the object to the projector to the desired result. If the distance of the object surface varies strong in camera direction, then the fringe pattern will be depicted only in a few areas of the object sinusoidal in many others however not. A second option to generate a sinusoidal pattern of frame projectors offers the use of an optic low-pass filter in front of the projector. But this is only possible in direction of the fringes so that a cross-projection is not longer feasible.

A second disadvantage of the phase shift technique is the analysis of the correspondence of one camera pixel to the projected fringe line. Using the phase shift technique an odd or even but in any case a natural pixel co-ordinate of the camera is correlated with a sub-pixel co-ordinate of the projector. If several cameras observe the same fringe sequence a direct pixel-to-pixel correspondence between the cameras can be established.

In order to avoid the disadvantages of the phase shift technique the line shift method was developed [Gühring, *et al*., 2000]. The line shift method is not based on the assumption of a sinusoidal depiction of the fringe pattern. Here, for each projected fringe line separately the centre in the picture is determined, see Figure 11.8.7. This allows correlating natural numbered projector co-ordinates with sub-pixel co-ordinates of the camera and thus enables a direct coupling of the frame measurements of several cameras, which observe the same fringe sequence. Due to this fact an increased redundancy is obtained and a higher accuracy is ensured. Another advantage of the line shift technique is a better compensation of eventual reflectivity changes at the liquid metal surface. Unfortunately, this new technology has currently low temporal resolution in the range of 10 Hz. But due the increasing computer technology and speed in the near future a more efficient system can be expected.

11.8.1.3.1 Fringe projection

In the fringe projection technique, a known optical fringe pattern is projected onto the surface of interest; the distribution of the fringe pattern on the surface is perturbed in accordance with the profile of the test surface, thereby enabling direct derivation of surface profiles. Phase shifting techniques [Quan, *et al*., 2001] are usually employed by projecting several fringe patterns with prescribed phase shift; however, these techniques are restricted to static objects. In many cases, 3-D surface profiling is required for vibrating objects or for objects with continually changing profile. With the availability of high-speed digital recording, it is possible to record projected fringe pattern with rates exceeding 10000 frames per second (fps). Recently several methods have been reported to retrieve the phase map from these images. [Huang, *et al*., 1999] developed a colour-encoded fringe projection technique to obtain the phase map by separating fringes with different colours followed by phase shifting. Previous

Figure 11.8.7. Gray-code sequence and the both alternatives to determine the sub-pixel correlation in the phase shift and the line shift technique (after [Böhm, 2001])

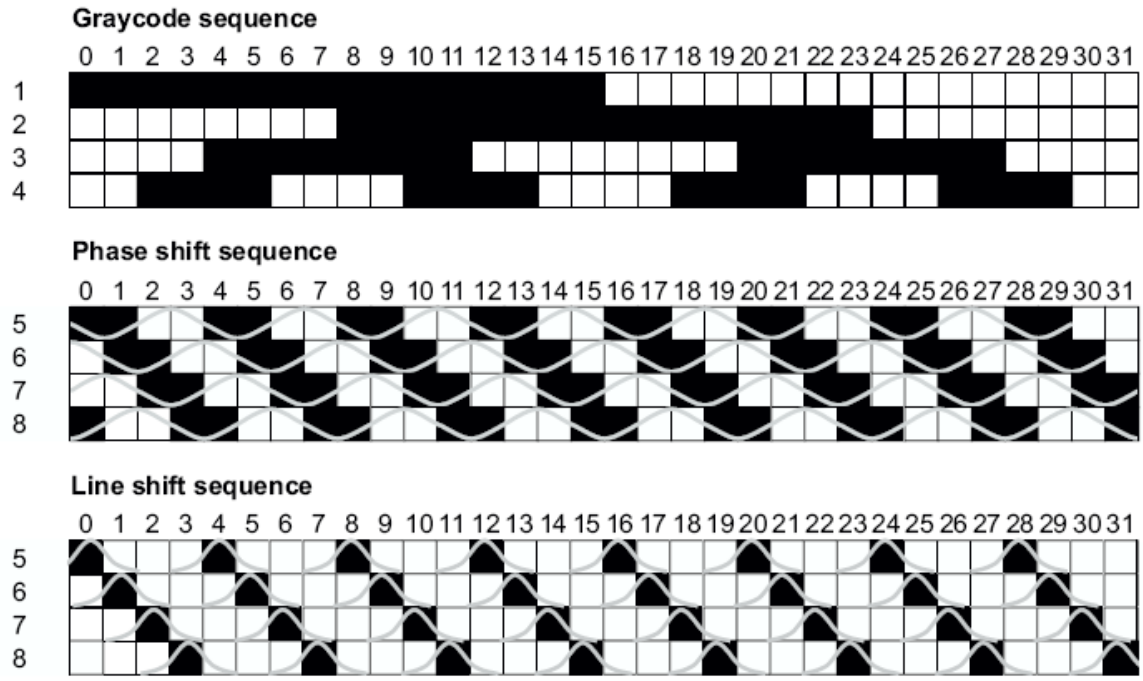

investigations by [Tay, *et al*., 2003] have shown that fast Fourier transform (FFT) with carrier fringe method is another effective approach. It requires fringes with high spatial frequency acting as a carrier. With proper filtering in frequency domain, the contour can also be evaluated. These two approaches are based on a similar concept in getting the phase map in spatial co-ordinates along the time axis. [Pawlowski, *et al*., 2002] developed a novel approach to retrieve point-by-point phase values using 1-D FFT along the time-axis. The spatial phase map at a certain instant can be obtained by combining the phase value of each point. Unlike Pawlowski's method of 1-D FFT, the current simple but robust trend is to retrieve point-by-point phase values along the time-axis [Tay, *et al*., 2004]. This method utilises a liquid crystal display (LCD) fringe projector and a high-speed CCD camera with telecentric gauging lens. High quality linear fringe patterns are projected on a vibrating object and the fringe patterns are imaged consecutively by a high-speed CCD camera. Applying phase scanning method initially reported by [Li, *et al*., 2001] on these fringe patterns, the surface profile at any instant, as well as the amplitude and frequency of the vibration, can be reconstructed.

The shape measurement based on the use of long working distance microscope, the LCD fringe projection and the phase-shifting methods allows even to measure large height measurement ranges up to 500 mm [Quan, *et al*., 2001] with accuracies in the range of microns.

Operation principle

Figure 11.8.8(a) shows the schematic layout of the projection and imaging system. With normal viewing, the phase change due to height *h* is given by:

$$h = \frac{L}{d} S = \frac{L}{d} \cdot \frac{\phi}{2 \cdot \pi \cdot f_0} = k \cdot \phi \tag{11.117}$$

where L is the distance between the LCD projector and the reference plane, d is the distance between the projector and camera axis, f_0 is the spatial frequency of the projected fringes on the reference plane and k, which can be obtained by calibration, is an optical coefficient related to the configuration of the system. ϕ is the phase angle change which contains the surface height information.

Figure 11.8.8. (a) Schematic layout of the projection and imaging system in the fringe projection technique. (b) Top view of the camera system.

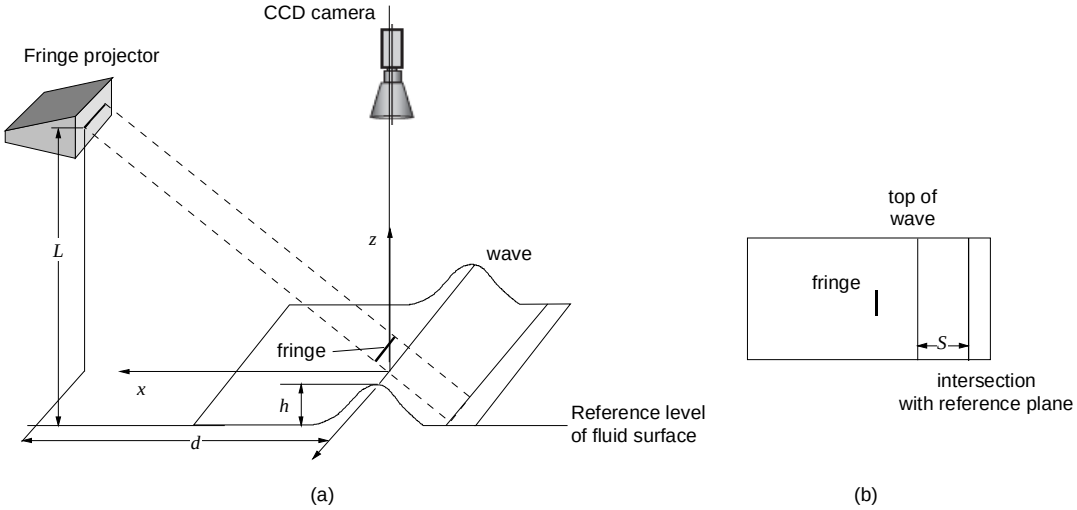

When a vertical sinusoidal fringe pattern is projected onto a moving three-dimensional surface, the distribution of the grating is perturbed by two factors, the motion or deformation of the surface and the initial profile of the test surface, when it is not deformed. The mathematical representation of the intensity distribution I captured by a CCD camera is governed by Eq. (11.118).

$$I(x,y,t) = a(x,y,t) + b(x,y,t)\cdot\cos\left[2\pi f_0 x + \phi_0(x,y) + \phi(x,y,t)\right] \tag{11.118}$$

where $a(x\,y,t)$ and $b(x,y,t)$ are the background and modulation factor, respectively, $\phi_0(x,y)$ is an initial phase which contains the shape information, and $\phi(x,y,t)$ is a time-dependent phase function related to the object vibration or deformation. $a(x\,y,t)$ and $b(x,y,t)$, which are also functions of time, are both slowly varying functions. Hence, $a(x\,y,t)$ and $b(x,y,t)$ can be regarded as constants in one period of intensity change. This assumption is of limiting nature with respect to the temporal resolution of fringe projection technique. Several images or frames are required, in which the surface shape is assumed to be constant. Assuming a frame rate of 250 frames per second as in the Tay, *et al*. experiment and at least eight frames, which are required to define the shape a temporal resolution of at maximum 30 Hz of the surface can be achieved.

If the amplitude of the surface motion is large enough, the variation of $\phi(x,y,t)$ will be larger than 2π, which implies more than one period intensity change. In most cases, this assumption can be satisfied by proper selection of carrier fringe frequency, projection angle and imaging area. With this assumption, the detectable maximum and minimum values of intensity within one period of intensity change at a certain point $P(x_p, y_p)$ on the test surface can be written as:

$$\begin{aligned} I_{\max}(x_p,y_p) &= a(x_p,y_p) + b(x_p,y_p) \\ I_{\min}(x_p,y_p) &= a(x_p,y_p) - b(x_p,y_p) \end{aligned} \tag{11.119}$$

Subsequently Eq. (11.118) is rewritten as:

$$I(x_p, y_p, t) = \frac{1}{2}\left[I_{\max}(x_p, y_p) + I_{\min}(x_p, y_p)\right] + \frac{1}{2}\left[I_{\max}(x_p, y_p) - I_{\min}(x_p, y_p)\right]\cos\Phi_p(x_p, y_p, t), \tag{11.120}$$

where:

$$\Phi_p(x_p, y_p, t) = 2\pi \cdot f_0 x_p + \phi_0(x_p, y_p) + \phi(x_p, y_p, t) \tag{11.121}$$

Hence the phase value can be expressed as:

$$\Phi_p(x_p, y_p, t) = \arccos\left[\frac{2I(x_p, y_p, t) - I_{\max}(x_p, y_p) - I_{\min}(x_p, y_p)}{I_{\max}(x_p, y_p) - I_{\min}(x_p, y_p)}\right] \tag{11.122}$$

As the first two terms in Eq. (11.121) are constants on the time-axis, the relative phase variation due to surface deformation at point *P* can be obtained as:

$$\phi(x_p, y_p, \Delta t) = \Phi_p(x_p, y_p, t_2) - \Phi_p(x_p, y_p, t_1) \tag{11.123}$$

At a certain time *T*, the phase map representing the contour of the surface can be expressed as:

$$\Phi(x, y, T) = 2\pi \cdot f_0 x + \phi_0(x, y) + \phi(x, y, T) \tag{11.124}$$

where $\phi(x,y,T)$ denotes the phase which is related to the surface deformation at instant *T*. Both phases $\phi(x_p,y_p,\Delta t)$ and $\phi(x,y,T)$ are wrapped phase values, as $\Phi_p(x_p,y_p,t)$ given by Eq. (11.122) is within 0 to π. For unwrapping, the values of ϕ at each point are converted from $[0,\pi]$ to $[0,2\pi]$. The phase values after conversion are determined by two factors, namely direction of deformation and the slope of intensity $\partial I/\partial t$ along the time-axis. Table 11.8.1 shows the details of the conversion. Unwrapping the phase values $\phi(x_p,y_p,\Delta t)$ given by Eq. (11.124) along the time-axis is a 1-D problem; retrieving the continuous phase values from $\phi(x,y,T)$ in Eq. (11.124) is a 2-D unwrapping problem, where numerous unwrapping algorithms are applicable, see e.g. [Ghiglia & Pritt, 1998].

Table 11.8.1. Conversion of phase values from $[0,\pi]$ to $[0,2\pi]$

Phase value in $[0,\pi]$	Direction of deformation	Slope of intensity along time axis $\partial I/\partial t$	Phase value in $[0,2\pi]$ after conversion
	Forward	≥0	$2\pi-\phi$
ϕ		<0	ϕ
	Backward	≥0	ϕ
		<0	$2\pi-\phi$

Experimental resources

For a free surface experiment a vertical sinusoidal fringe pattern is projected onto the fluid by a programmable LCD projector. The fringe patterns are captured at right angle to the surface at rest by a high speed CCD camera, e.g. KODAK Motion Corder Analyzer, SR-Ultra. Using a telecentric gauging lens ensures that the magnification of telecentric lens is independent of the working distance, in

contrast to conventional lenses. It remains constant regardless of the object distance from the camera. This reduces magnification error due to the deformation and greatly extends gauging depth of field. With this special lens, the positions of a moving object in the image plane remain the same, while only the fringe pattern is shifted periodically. The pitch of the fringe pattern and the angle of projection are selected according to the amplitude of surface deformation.

At the start-up the coefficient k in equation must be determined in a calibration procedure. Therefore, the fluid surface is set to a known distance in the z-axis and the corresponding phase difference on the surface for different heights is determined by the conventional four-step phase shifting method.

In a next step the surface of interest can be investigated. Therefore, the minimum and maximum intensities occurring at each point must be determined. The extreme positions of surface deformation vibration are readily identified by the computer since the first derivative of intensity $\partial I/\partial t$ of most pixels in the image changes sign (either from positive to negative or vice versa). If this is performed the real test run can start.

For each pixel, several data points along the time axis are obtained. Figure 11.8.9(a) shows the grey value variation of a discrete point of a polished coin in the [Tay, *et al*., 2004] experiment, which was defined vibrated on a table. The extreme positions of the vibration are encircled in Figure 11.8.9(b). The corresponding wrapped phase values of this experiment are presented in graph 11.8.9(b). After unwrapping along the time-axis, the continuous phase profile depicted in Figure 11.8.9(c) is obtained. Subsequently the frequency of vibration can be calculated from the time shift of the maxima; in this case it is evaluated as 5.68 Hz. The amplitude of phase change at this point A_Φ is known after unwrapping, from which the surface height at this point can be calculated.

Figure 11.8.9. (a) Grey value variation at a discrete point in the [Tay, *et al*., 2004] experiment. (b) Wrapped phase value at this point. (c) Continuous-phase profile after unwrapping.

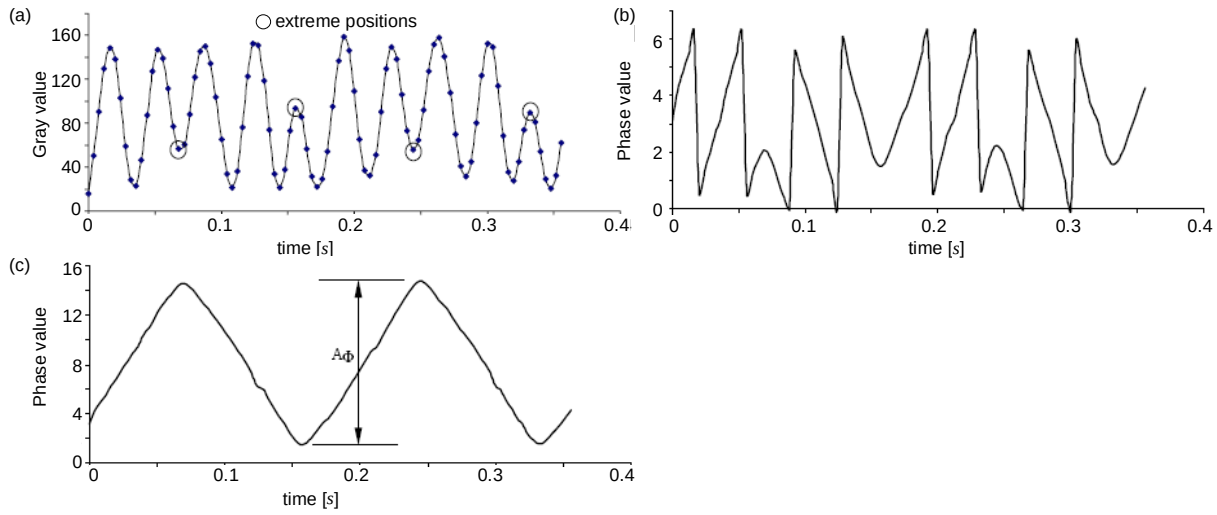

Often it can be observed that the maximum and minimum values of each cycle of phase variation (2π change) are slightly different. This is due to fluctuation of the LCD panel and intensity of the projector light source. Relatively large errors in the phase profile also occur when the grey value approaches the extreme values. The errors are introduced by: 1) the maximum or minimum values detected by the camera are slightly different from the actual extreme grey scale values; (2) for a sine-wave configuration, a slight difference in grey level near the extreme values causes a large

change in phase value. The errors can be minimised by proper selection of the recording rate and frequency of the carrier fringes such that the number of sampling points is optimised within one cycle of grey level change.

At a certain instant time *T*, a combination of phase values on each pixel produces a wrapped spatial phase map. After unwrapping, the continuous phase map, which represents the surface profile, can be obtained. Using the calibrated coefficient *k*, the phase map can be converted into a 3-D surface profile. Very often some vertical stripes are observed on the phase map, this is due to the errors introduced by the extreme values of grey level mentioned above. In spatial co-ordinate, these errors can be reduced by applying a filtering mask on the phase map. In many commercial systems, a 3×3 median mask is used.

To verify the accuracy of this technique, a comparison can be made with the fast Fourier transform (FFT) and conventional four-step phase shifting methods [Quan, *et al*., 2001]. Four fringe patterns with a phase increment of $\pi/2$ are projected onto a stationary test surface using the same experimental setup. For each fringe pattern, an averaged image can be obtained from numerous images. Four of such images are subsequently used in the four-step phase shifting algorithm, while one of the images is used for the FFT method. As the phase evaluation is carried out point-by-point along the time-axis, the phase scanning method is best suited to determination of a surface with a complicated profile. The maximum difference of the phase value between both methods is small. In the [Tay, *et al*., 2004] experiment surface height differences of 0.01 mm could be resolved.

It is worth noting that the fringe projection technique is limited to out-of-plane displacement from a reference, and high quality sinusoidal fringes are required to identify the maximum and minimum grey values. The recording rate of the camera should also be higher than the frequency of surface deformation. A recording rate of at least eight times of the temporal change of the surface deformation frequency is found adequate.

Some concluding remarks

The fringe projection technique requires besides the large and expensive experimental set-up a lot of computational effort. A critical issue using this technique is to extract the phase signal from a number of phase shifted fringe patterns.

The phase angle obtained is wrapped by a factor of 2π and can be unwrapped by different phase unwrapping algorithms [Strand and Taxt, 1999] or [Ghiglia and Pritt, 1998]. However, the problem of path dependence, due to the existence of residues in a wrapped phase map, is often encountered during the phase unwrapping process. This means by following different unwrapping paths, an algorithm would produce different results. Several methods have been reported to eliminate the influence of residues. A block path algorithm proposed by [Goldstein, *et al*., 1988] connects positive residues and negative residues by “branch cuts”. By following a path without crossing any branch cut, it is able to produce a unique unwrapped phase map and hence the phase unwrapping process would be path independent. The algorithm connects a residue with its nearest opposite charge neighbour based on a least length principle. Although this strategy is effective in generating short branch cuts, it does not take into consideration of the quality of phase data. A high-quality phase area may be separated into discrete regions, which would result in discontinuities in a surface profile. An alternative method is the quality-guided phase unwrapping algorithm, which uses a quality map to guide the unwrapping process instead of directly eliminating residues. Since the algorithm is an integration process, in which the unwrapped phase value of a pixel is dependent on the phase values of pixels that have been unwrapped, an accurate quality map would lead reliable phase data to be unwrapped at an early stage and hence unwrapping errors would be confined to a minimum area. [Bone, 1991] first incorporated

phase quality into phase unwrapping by means of a quality mask. This was followed by the work of [Quiroga, *et al.*, 1995], [Lim, *et al.*, 1995] where quality-guided algorithm is developed from "a quality mask" to an adaptive algorithm without the need of a threshold.

A quality map consists of arrays of values that define the quality or goodness of each pixel in a phase map. Depending on applications, various quality maps can be generated. Some quality maps are derived from a wrapped phase map; while others are extracted directly from the data where wrapped phase is derived, such as the fringe contrast map. Regardless of how a quality map is derived, the algorithm that uses the quality map to guide phase unwrapping is similar. A detailed quality-guided phase unwrapping algorithm can be found in [Ghiglia and Pritt, 1998] and the fringe contrast based phase unwrapping algorithm is a type of quality guided phase unwrapping algorithm. The fringe contrast based algorithm unwraps high contrast phase at an early stage and low contrast phase at a later stage so that low contrast data do not affect high contrast data. The algorithm does not consider the influence of residues. Instead, it is based on the assumption that an accurate fringe contrast map would guide an unwrapping path without encircling any unbalanced residues. A detailed description can be found in [Chen, *et al.*, 2005].

Currently no liquid metal experiment to the knowledge of the author has been performed using this technique, but the results obtained for nearly reflecting moving surfaces shows encouraging results. Moreover, the recent progress in the image processing techniques triggered by the particle image velocimetry (PIV) as well as the use of this technique in the car manufacturing industry in combination with the rapidly increasing computing power offers the potential feasibility in the near future for the application in liquid metal systems.

11.8.1.3.2 Laser speckle interferometry

If a laser beam illuminates a continual deformation of a surface, it will lead to a temporal speckle pattern on the observation plane. Recording this time-dependent speckle pattern the deformation of the surface of an object can be obtained. In general two methods, the scanning phase method (SPM) and the time sequence phase method (TSPM), are used for measuring the displacement caused by the deformation in temporal speckle pattern interferometry (TSPI). Their principle is that by capturing a series of speckle interference patterns related to the object deformations, the fluctuations in the intensity of the interference patterns can be obtained. Through scanning these fluctuations and estimating both the average intensity and modulation of the temporal speckle interference patterns, the phase maps for whole-field displacements are calculated. In this way one is capable of quantitatively measuring continual displacements simply using a conventional electronic speckle pattern interferometry (ESPI) system without phase shifting or a carrier. The elaboration on the new methods is given in the paper by [Li, *et al.*, 2001] or [Toh, *et al.*, 2001].

The data reduction of the acquired images and the subsequent image processing is similar to that of the fringe projection. The speckle interferometry also requires a significant mathematical and computational effort. Due to the use of a more sophisticated optical system compared to the fringe projection the image processing is more time consuming. However, the attainable spatial resolutions using speckle interferometry is an order of magnitude larger than that of the fringe projection. The principle set-up of the speckle interferometer is shown in Figure 11.8.10.

The phase map of a displacement field caused by the deformation of the surface can be evaluated directly with temporal series of speckle patterns captured by a conventional ESPI system or a speckle interferometry system. This is a real-time shifting or time-carrier method, where the phase change is caused by the continuous deformations of the tested surface. It is significant to simplify the

Figure 11.8.10. Schematic of the deformation analysis system for the temporal speckle pattern method

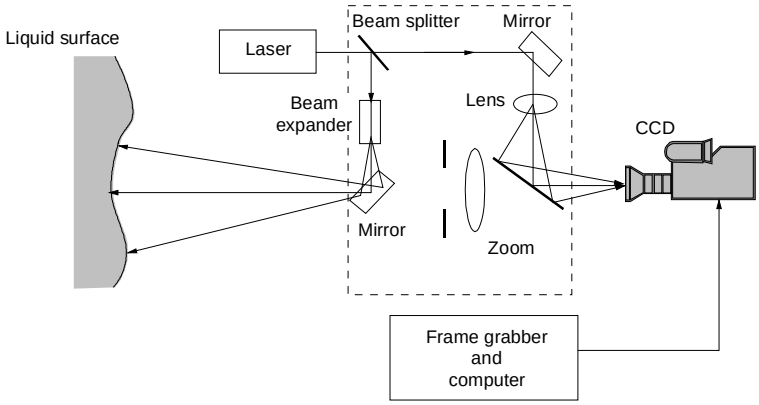

measurement system, so as to be suitable to an execrable environment. Comparing with the Fourier transform method, SPM and TSPM simply needs fewer frames to evaluate the phase map. In the lower limitation, only one period including six frames is necessary to evaluate the phase data. This means that the displacement down to half of a wavelength of the illumination beam still can be resolved. The upper limitation of the measurement highly depends on the correlation of the temporal speckle patterns and the storage ability of a computer system. However, the total displacement measured by the speckle interferometry methods is much greater than by the ESPI with the same testing system.

11.8.2 Acoustic distance measurements

Generally, two possibilities to acquire the surface shape of a wavy liquid metal surface are possible. The first is to install the ultrasound sensor in the gas phase and transport the sound waves through the gas. This technique requires first a gas filling as transport medium and a detailed knowledge of the temperature layering within the gas, which determines the sound velocity; but, it has the advantage of the temperature decoupling of the sensor from the liquid and moreover, the wetting problem as well as the corrosion of the sensor is avoided. However, in most problems the free liquid metal surface is shaped by the pressure field and the velocity distribution within the flow. Hence, for a detailed analysis of the problem at least two quantities must be known. Applying, an ultrasound sensor directly in the fluid gives the opportunity to capture the velocity field and the surface height, but faces the above named problems. The subsequent paragraphs first describe the surface shape measurement using an ultra-sonic system operating through air and the second one a system, which acquires both velocity and surface position using a sensor being in direct contact with the liquid metal.

11.8.2.1 Ultrasonic distance measurement using frequency shift-keyed signal

The techniques of distance measurement using ultrasound in air or noble gases include the time-of-flight (TOF) technique (see e.g. [Parilla, *et al*., 1991], [Marioli, 1992], [Tardajos, *et al*., 1994]), single-frequency continuous wave phase shift [Young and Lee, 1992], two-frequency continuous wave method (e.g, [Shoenwald and Smith, 1984]), combining methods of TOF and phase-shift (e.g. [Gueuning, *et al*., 1997]), multi-frequency continuous wave phase shifts (e.g. [Kimura, *et al*., 1995] or [Huang, *et al*., 1999]) and a multi-frequency AM-based ultrasonic system [Yang, *et al*., 1994]. The TOF method has been extensively discussed in the recent literature. The pulse propagates through the transmission medium and is reflected by the surface. The reflection using ultrasound is independent of the optical properties of the fluid compared to the previously discussed optic

techniques. The time taken for the pulse to propagate from transmitter to receiver is proportional to the reflector's range. The distance between the reflector and transducer site is $d = (c \cdot t)/2$, where c is the sound velocity and t the TOF. Using TOF to measure the distance, the system errors are primarily due to amplitude degradation of the received signal, and uncertainty in the speed of sound. The method is more efficient when the energy transferred between emission and reception is high, but it is strongly limited by the ultrasonic transducers, which must be of rather high quality factor, high power, and high cost. Increasing the frequency of the pulse transmitted can improve the accuracy and the resolution, but the higher frequency of the pulse transmitted, the greater the attenuation per unit distance. Therefore the maximum measurable distance will also be reduced. Normally, if distances in air of a few meters are to be measured, frequencies in the range 20-100 kHz must be used in order to maintain suitable receiver signal levels [Webster, 1994]. So the TOF method of range measurement is subject to high levels of errors (about 1 cm) when used in an air medium, thus limiting its applications.

In order to obtain accurate distance estimations, a superior system choice is the phase data of a steady-state frequency received signal with reference to its transmitted signal. This is because the distance information is derived from the phase difference of a repeating signal which is sampled for a statistically significant number of wave periods. Thus, the random variations in phase shift (originating from turbulence, environmental noise, electronic noise, etc.) tend to cancel themselves out in an averaging process. Most applications of range measurement in air using ultrasound apply a phase-shift analysis of single-frequency continuous-wave transmission [Figueroa and Barbieri, 1994]. If the transmitter is energised with a continuous sinusoidal signal, the signal corresponding to the received acoustic wave can be written as $Vr(t) = Ar \sin(\omega t + \theta)$. Here Ar is the peak value of the received signal, ω is the resonant angular frequency of the transducer, and θ is the phase shift, which is linearly proportional to the measured surface distance. The range or distance L can be determined by the phase shift θ of a single frequency if the maximum ranging distance does not exceed one full wavelength; otherwise phase ambiguity will occur. Thus the maximum achievable range for transducer with a resonant frequency of 40 kHz is about 4.25 mm which is too short for scientific interests. Although this disadvantage can be improved by a multiple-frequency continuous wave technique, which calculates the surface distance at ranges much greater than one wavelength, the range of measurement is still too short (only 1500 mm) [Huang, *et al*., 2002].

[Gueuning, *et al*., 1997] presented an algorithm for the distance measurement which combines both the pulse TOF method and the phase-shift method and can obtain accurate distance measurement better than 1 mm. The technique is based on a particular signal processing method which determines the approximate TOF by computing the cross-correlation between the envelope of the transmitted and received signals. The carrier phase shift between emission and reception is then computed in order to refine the final result. But the accuracy of this computed the phase shift is limited by the amplitude accuracy of the samples and the resolution of the analogue to digital (A/D) converter, and the refined range does not exceed a wavelength of the transmitted signals. [Webster, 1994] presents a method that is based upon the binary frequency shift-keyed (BFSK) signal followed by data acquisition and signal processing of phase-digitised information from the received signal. The method can reduce many of the problems that arise when dealing with the non-ideal behaviour of ultrasonic transducers. But the TOF is estimated by the time at which the transition between the frequency f_1 and f_2 occurs and is determined from the phase data, which are easily influenced by noise, and errors arise.

In the newest technological trend combined methods are used to achieve better, more accurate distance measurement. In these distance measurement systems two independent signal part are analysed. One part estimates the TOF, and the other part calculates the phase-shift difference between the transmitted and received signal. This method is based upon the transmission of a BFSK signal. Upon reception of the pulse, the TOF is computed by the time at which the change between each discrete frequency occurs and two phase shifts between the transmission and reception signals are detected in

order to enhance the accuracy of the time measurement. The phase shifts are computed by a counter technique to avoid the limitation caused by the amplitude of the signal and the finite bits of the A/D converter.

Operation principle

The principle of the distance measurement system is similar to the operation of using a ruler. At first a coarse measurement is done, and then a fine measurement is adopted to refine the final result. Thus the high accuracy is achieved.

The transmitted signals and the received signals are shown in Figure 11.8.11. The S_T is the transmission signal of a BFSK, which has two frequencies f_1 and f_2 depicted in Figure 11.8.11(a). The T_r is the period of S_T. The S_R is the received signals corresponding to the transmitted signals as illustrated in Figure 11.8.11(b).

Figure 11.8.11. UDV signal emission for surface distance measurement. (a) Transmitted signals and (b) received signals.

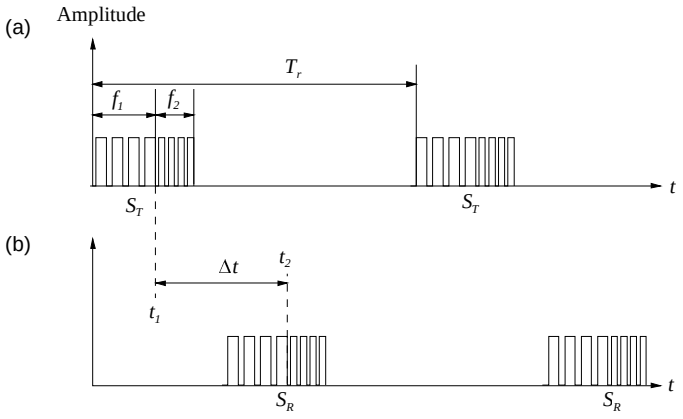

There are two steps to processing of the received signal. The elapsed time Δt (TOF), which is the round-trip travel time of the transmitted signal from the transmitter to the reflective target (surface) and back to the receiver, can be calculated by received/transmitted signals and written as $\Delta t = t_2 - t_1$. Here, t_1 is the time when f_1 changes to f_2 of the transmitted signal, t_2 is the time when f_1 changes to f_2 of the received signals corresponding to the transmitted signals. The distance of the emitter to the surface can be expressed as $d = (c\,\Delta t)/2$, where c is the sound velocity.

The detection of the phase shift is based on the two-frequency continuous wave method of ultrasonic distance measurement. The phase shift of θ_1 and θ_2 can be detected by the received signals corresponding to the transmit signals. A continuous wave with frequency f_1, and a received signal (SR) with frequency f_1 and f_2 are shown in Figure 11.8.12. The phase shift θ_1 is the difference in phase between the continuous wave and the received signal at f_1. The phase θ_1 can be written as $\theta_1 = 2\pi(t_2 - t_1)/T_1$, where T_1 is the period of the received signal of f_1. Similarly, the phase θ_2 is the difference in phases regarding the received signal at f_2. A comparison of the two phase shifts allows calculating the distance. The formulas can be written as:

$$L = \frac{1}{2}\left(n_1 + \frac{\theta_1}{2\pi}\right)\lambda_1 \quad \text{and} \quad L = \frac{1}{2}\left(n_2 + \frac{\theta_2}{2\pi}\right)\lambda_2 \tag{11.125}$$

where L is the distance between the surface point and transducer site, λ_1, λ_2 are the wavelengths of the ultrasound, n_1, n_2 are integers, and θ_1, θ_2 are phase shifts. Due to the different wavelengths, the expression for the difference of the phase shift may be derived from Eq. (11.125) in the way:

$$\Delta\theta = \pi \cdot L\left(\frac{1}{\lambda_2} - \frac{1}{\lambda_1}\right) \tag{11.126}$$

The integers n_1 and n_2 in Eq. (11.125) have only two possible values: $n_1 = n_2$ and $n_2 = n_1 + 1$. So the difference of the phase shifts can be defined by the following algorithm:

$$\begin{aligned} &\text{If } \theta_2 > \theta_1, \text{ then } \Delta\theta = \theta_2 - \theta_1 \text{ and} \\ &\text{If } \theta_2 < \theta_1, \text{ then } \Delta\theta = \theta_2 - \theta_1 + \pi \end{aligned} \tag{11.127}$$

If the velocity of ultrasound along the signal path is constant, say c, the wavelength λ can be determined as: $\lambda_1 = c/f_1$, $\lambda_2 = c/f_2$. Here, f_1 and f_2 are the frequencies of the ultrasonic wave. From Eq. (8.19) the distance of the surface can be expressed as:

$$L = \frac{\Delta\theta}{\pi} \cdot \frac{c}{\Delta f} \text{ with } \Delta f = f_2 - f_1 \tag{11.128}$$

The distance to the surface L can be uniquely determined by the difference of the phase shifts $\Delta\theta$, if the maximum distance does not exceed the half of wavelength of Δf. Otherwise a phase ambiguity will occur. The maximum achievable detecting range with Eq. (8.18)a is about 4.375 mm and with Eq. (11.128) is about 175 mm (taking c = 350 m/s, f_1 = 40 kHz, f_2 = 41 kHz).

Figure 11.8.12. Illustration of the of the two phase shifts θ_1 and θ_2

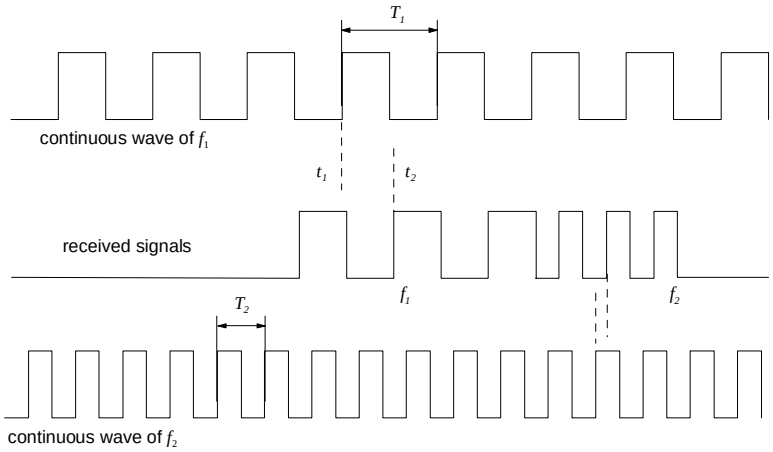

In order to obtain a high accuracy over a large distance d the following algorithm can be used. The distance d can be obtained by $d = (c\ \Delta t)/2$, where the Δt is TOF. d is divided into regions $[(k-1)Lr, kLr]$ (k = 1,2,3,...) a schematically depicted in Figure (8.14)a. The Lr is the wavelength of Δf. The distance d can be expressed as:

$$d = \frac{1}{2}\left[(k-1) + \left(\frac{\Delta\theta}{2\pi}\right)\right] \cdot \frac{c}{\Delta f} \text{ again with } \Delta f = f_2 - f_1 \tag{11.129}$$

where k is an integer. The region defined by $[(k-1)Lr, kLr]$ is referred to as the number k region. The $k-1$ integer can be obtained by Int($\Delta t\ \Delta f$) with Int [] the integer operation. So the estimate of target distance can be expressed by the following algorithm:

$$d = \frac{1}{2}\left[\mathrm{Int}(\Delta t \Delta f) + \left(\frac{\Delta\theta}{2\pi} \right) \right] \cdot \frac{c}{\Delta f} \tag{11.130}$$

In order to increase the accuracy, the number k region can be divided by l, where $l = \lambda_1 = c/f_1$. This is graphically shown in Figure (11.8.14)b. The fine scale measurement of $(\Delta\theta/2\pi)\cdot(c/\Delta f)$ can be replaced as $(m + \theta_1/2\pi)\cdot c/f_1$, where the integer m can be obtained by Int$[(\Delta\theta/2\pi)\cdot(f_1/\Delta f)]$. The final estimate of distance can be expressed as:

$$d = \frac{1}{2}\mathrm{Int}(\Delta t \Delta f) \cdot \frac{c}{\Delta f} + \frac{1}{2}\left[\mathrm{Int}\left(\frac{\Delta\theta}{2\pi} \cdot \frac{f_1}{\Delta f} \right) + \frac{\theta_1}{2\pi} \right] \cdot \frac{c}{f_1} \tag{11.131}$$

Figure 11.8.14. (a) Relation between $d = c\,t$ and $d = (k-1)\cdot Lr + (\Delta\theta/2\pi)\cdot Lr$. b.) Relation between d, Lr and l.

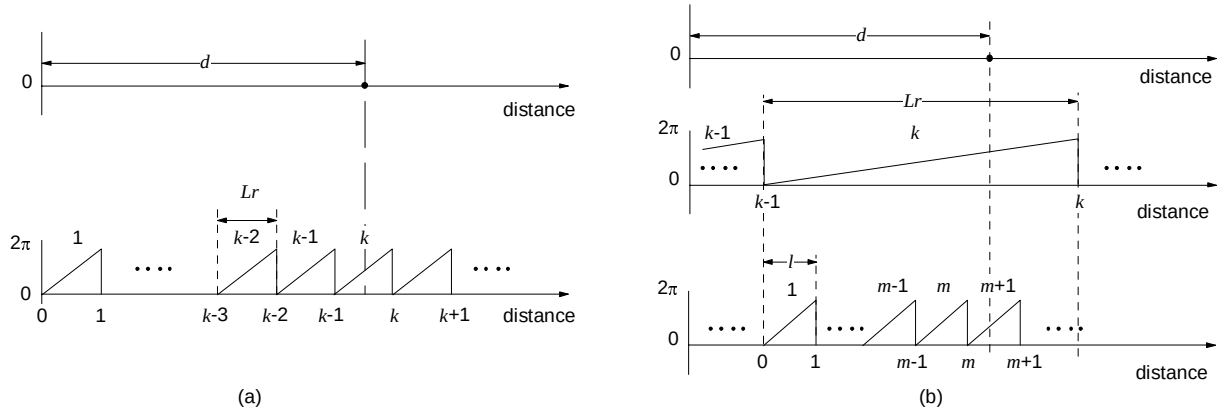

System set-up and operation

The measurement hardware consists of two acoustic transducers with matching exponential horns, a signal generation system, power amplifier, preamplifier and gain-controlled system, frequencies detected system, digital phase meter, and calibration system. A microprocessor-based controller governs the operation of the entire system, more details may be taken from [Huang, *et al*., 2002]. Before starting the distance measurement the system must be calibrated with a known distance. By choosing appropriate frequencies accuracies in the range of tenth of a millimetre can be obtained with standard variations being in the micrometer range. The temporal resolution is in the range of the UDV systems for velocity measurements in the range of 20-30 Hz. One of the biggest disadvantages affecting the measurement accuracy considerably is that the temperature distribution in the gas environment transporting the sound must be known before starting the surface measurement campaign.

11.8.2.2 Ultrasonic velocity profile meter

The liquid-phase velocity profile below interfacial waves in horizontally-stratified gas-liquid two-phase flows affects the interfacial exchanges of mass, momentum and heat and the growth of the interfacial waves. For cases of practical importance, such as stratified wavy two-phase flows, it is

generally difficult to predict theoretically or measure experimentally the liquid phase velocity profile which is coupled with the wavy interface profile. The theoretical velocity profile with the wavy interface profile is available only for limited cases, such as infinitesimal and solitary waves. Furthermore, both the velocity and interface profiles of the interfacial waves of wavy flows usually deviate greatly from such theoretical profiles.

The ultrasonic velocity profile (UVP) meter, see [Takeda, *et al*., 1994], [Takeda, 1995] or Section 11.4.1) was developed to measure an instantaneous velocity profile of liquid flows dynamically, using the Doppler shift frequency in echoes reflected at small particles flowing with liquid. The UVP meter combined two methods used in medical; a pulse method to detect the distribution of various tissues from the time delay of reflected pulses and a Doppler method to detect the velocity variation within the fluid using echoes from continuous ultrasound. The transducer emits an ultrasonic pulse, receives reflected echoes until the next pulse emission. Velocity profiles composed of two sets of information – instantaneous velocities at different locations – along the path of ultrasonic pulses, are successively obtained with a short time interval. The particle location is obtained from the time duration between the pulse emission and the echo detection. The applicability of the UVP has been demonstrated for duct flows in various configurations, see Section 11.4.1.

The fact that ultrasound totally reflects at the gas-liquid interface at any incident angles provides a simple technique to detect the liquid gas-interface. If both quantities are required simultaneously lots of precautions and countermeasures have to be taken that multiple reflections from the interface, especially if it is wavy, does not influence the velocity reading. Nevertheless, numerous possibilities to avoid multiple reflections are available and described in the paper by [Nakamura, *et al*., 1995].

11.9 Summary and final comments

The instrumentation development for special liquid metal adapted technique has increased its speed in the past decade significantly. This observation can be seen from the attached literature list and it is triggered by many aspects, which arises from the nuclear technology both in fission (fast breeder, accelerator-driven systems to transmute nuclear waste or high power density systems) and in fusion (liquid metal cooled blankets or divertors) but also in conventional engineering as steel or aluminium casting, metal refinery or crystal growth for the computer technology. In all of these fields liquid metal adapted instrumentation is required to control the process, ensure the safety and reliability of the individual facility.

The realisation of different nuclear and industrial facilities operating with liquid metals pushed the speed of innovation, since increasing energy costs enforces the demand of a simultaneously economic operation and safe operation.

Of course, the author of this chapter can not cover the whole development process currently underway. This chapter is restricted to the description of the techniques and methods known from the literature or tested by colleagues or by myself. In some cases measurement techniques are described, which were up to now not tested for liquid metals, but show from their principle the feasibility of an application to it. I tried to explain the measurement principle, to describe the algorithms to reduce the measurement data and to sketch the experimental effort to obtain the required quantities property adequately. Of course, many of the techniques described in this context reveal numerous error sources or require model assumptions. I tried to quantify the potential error sources and methodologies to avoid systematic errors. Regarding the model assumptions in some cases necessary to interpret the measured raw data I hopefully mentioned the main ideas completely to the gracious reader and gave the adequate literature sources.

REFERENCES

Abderrahim, H.A., P. Kupschus, E. Malambu, P. Benoit, K. Van Tichelen, B. Arien, F. Vermeersch, P. D'hondt, Y. Jongen, S. Ternier, D. Vandeplassche (2001), "MYRRHA: A Multipurpose Accelerator Driven System for Research & Development", *Nuclear Instruments and Methods in Physics Research A*, Vol. 463, pp. 487-494.

Allen, C.M., L.J. Hooper (1932), "Piezometer investigation", *ASME Trans.*, Vol. 54, p. 54ff.

Amman, M., T. Bosch, M. Lescure, R. Myllylä, M. Rioux (2001), "Laser Ranging: A Critical Review of Usual Techniques for Distance Measurement", *Opt. Eng.*, Vol. 40 (1), pp. 10-19.

Argyropoulos, S.A. (2001), "Measuring Velocity in High-temperature Liquid Metals: A Review", *Scandinavian Journal of Metallurgy*, Vol. 30, pp. 273-285.

Baker, M.C., R. Bonazza (1998), "Visualization and Measurements of Void Fraction in a Gas-molten Tin Multiphase System by X-ray Absorption", *Exp. in Fluids*, Vol. 25, pp. 61-68.

Barleon, L., K-J. Mack, R. Stieglitz (1996), *The MEKKA Facility: A Flexible Tool to Investigate MHD Flow Phenomena*, FZKA-Report FZKA-5826.

Baribeau, R., M. Rioux (1991), "Influence of Speckle on Laser Range Finders", *Appl. Opt.*, Vol. 30 (20), pp. 2873-2878.

Baribeau, R., M. Rioux, G. Godin (1992), "Color Reflectance Modeling Using Polychromatic Laser Range Sensor", *IEEE Transaction on Pattern Analysis and Machine Intelligence*, Vol. 14, pp. 263-269.

Barker, M. (1922), "On the Use of Very Small Pitot-tubes for Measuring Wind Velocities", *Proc. R. Soc. A*, Vol. 101, pp. 435-445.

Barton, J.P. (1993), "Neutron Radiography – Status and International Prospects", *Proceedings 5th Int. Symp. Advanced Nuclear Energy Research – Neutrons as Microscopic Probes*, Mito, Japan, 10-12 March 2003, JAERI-M93-228, Vol. 1, p. 125ff.

Beckord, P., G. Höfelmann, H.O. Luck, D. Franken (1998), "Temperature and Velocity Field Measurements Using Ultrasonic Computer Tomography", *Heat and Mass Transfer*, Vol. 33, pp. 395-403.

Beheim, G., K. Fritsch (1983), "Remote Displacement Measurements Using a Laser Diode", *Electron. Lett.*, Vol. 21, pp. 93-94.

Beitz, W., K-H. Küttner (1986), "Dubbel-taschenbuch des Maschinenbaus", Springer-Verlag, 15th edition, ISBN 3-540-12418-7, p. 1211 ff (in German).

Berge, B., K. Grjotheim, C. Krohn, R. Naeumann, K. Torkler (1973), *Met. Trans.*, Vol. 4, pp. 1945-1952.

Blaskett, D.R. (1990), "Lead and Its Alloys", Ellis Horwood Limited, Chichester, England.

Böhm, J. (2001), "Erfassung und Interpretation von dichten Oberflächendaten", DGPF-Jahrestagung, 10, Konstanz, pp. 1-9 (in German).

Bone, D.J. (1991), "Fourier Fringe Analysis: The Two-dimensional Phase Unwrapping Problem", *Appl. Opt.*, Vol. 30, pp. 3627–3632.

Bonfig, K.W. (2002), "Technische Durchflußmessung", 3, Auflage, Vulkan Verlag Essen.

Bosch, T., M. Lescure (Eds.) (1995), "Selected Papers on Laser Distance Measurement, SPIE Milestone Series", Vol. MS 115, SPIE Optical Engineering Press, Bellingham, WA.

Bosch, T., M. Lescure (1997), "Error Analysis of 1-10 m Laser Phaseshift Rangefinder", *IEEE Trans. Instrum. Meas.*, Vol. 46 (6), pp.1224-1228.

Boyarevich, A.V. (1990), "Measurement of Averaged Local Velocities in Magnetohydrodynamic Experiments", *Magnetohydrodynamics*, Vol. 26, p. 133.

Bradley, B.E., E.W. Dewing, J.N. Rogers (1984), "Light Metals", Vol. 1, pp. 541-552.

Brauer, H. (1971), "Grundlagen der Ein- und Mehrphasenströmungen", Sauerländer Verlag (in German).

Brito, D., H-C. Nataf, Ph. Cardin, J. Aubert, J.-P. Masson (2001), "Ultrasonic Doppler Velocimetry in Liquid Gallium", *Experiments in Fluids*, Vol. 31, pp. 653-663.

Buchholz, J., R. Steinemann (1984), "Application of an Electrical Conductivity Microprobe for the Characterisation of Bubble Behaviour in Gas-liquid Bubble Flow", *Part. Charact.* 1.

Burgess, J.M., P.H. Calderbank (1975), "The Measurement of Bubble Parameters in Two-phase Dispersions. I. The Development of an Improved Probe Technique", *Chem. Eng. Sci.*, Vol. 30, pp. 743-750.

Burrows, E., K. Liou (1990), "High-resolution Laser LIDAR Utilizing Two-section Distributed Feedback Semiconductor Laser as a Coherent Source", *Electron. Lett.*, Vol. 26, pp. 577–579.

Casal, V., G. Arnold (1988), "Velocimeter for Local Measurement in Liquid Metals", *1st World Conf. on Experimental Heat Transfer in Fluid Mech. and Thermodyn.*, 4-9 September 2003, Dubrovnik, Yugoslavia.

Cha, J.E., Y.C. Ahn, M.H. Kim (2002), "Flow Measurement with an Electro-magnetic Flow Meter in Two-phase Bubbly and Slug Flow Regimes", *Flow Meas. Instrum.*, Vol. 12, pp. 329-339.

Cha, J.E., Y.C. Ahn, K.W. Seo, H.Y. Nam, J.H. Choi, M.H. Kim (2003), "An Experimental Study on the Characteristics of Electro-magnetic Flow Meters in the Liquid Metal Two-phase Flow", *Flow Meas. Instrum.*, Vol. 14, pp. 201-209.

Chen, L., C. Quan, C.J. Tay, Y. Huang (2005), "Fringe Contrast-based 3-D Profilometry Using Fringe Projection", *Optik*, Vol. 116, pp. 123-128.

Cheng, H. (1997), "The Bubble-to-slug Flow Pattern Transition in Vertical Columns", PhD thesis, Department of Chemical Engineering, University of Nottingham, UK.

Cherry, E., D. Hooper (1968), "Amplifying Devices and Low-Pass Amplifier Design", Wiley, New York.

Cho, J., M. Perlin, S.L. Ceccio (2005), "Measurement of Near Wall Stratified Bubbly Flows Using Electrical Impedance", *Meas. Science Techn.*, Vol. 16, pp. 1021-1029.

Chiba, S., K. Idogawa, Y. Maekawa, H. Moritomi, N. Kato, T. Chiba (1989), "Neutron Radiographic Observation of High Pressure Three-phase Fluidization", in J.R. Grace, L.W. Shemilt, M.A. Bergougnon (Eds.), *Proceedings Int. Conf. Fluidization*, 7-12 May 1989, Banff, Alberta, Canada, Fluidization VI, *AIChE*, p. 523ff.

Chue, S.H. (1975), "Pressure Probes for Fluid Measurements", *Prog. Aerosp. Science*, Vol. 16, pp. 147-223.

Ciccarelli G., D. Frost (1994), "Fragmentation Mechanisms Based on Single Drop Steam Explosion Experiments Using Flash X-ray Radiography", *Nucl. Engng. Des.*, Vol. 146, pp.109-132.

Daidzic, N.E., E. Schmidt, M.M. Hasan, S. Altobelli (2005), "Gas-liquid Phase Distribution and Void Fraction Measurements Using MRI", *Nuc. Engng. Des.*, Vol. 235, pp. 1163-1178.

Davidson, P. (2001), "An Introduction to Magnetohydrodynamics", Cambridge University Press 2001, ISBN 0521 791 499.

Delhaye, J.M. (1983), "Two Phase Pipe Flow", *Int. Chem. Eng.*, Vol. 23 (3), pp. 395-410.

Dias, S.G., F.A. Franca, E.S. Rosa (2000), "Statistical Method to Calculate Local Interfacial Variables in Two-phase Bubbly Flows Using Intrusive Crossing Probes", *International Journal of Multiphase Flow*, Vol. 26, pp. 1797-1830.

Dickinson, J. (1975), "Turbulent Skin Fraction Techniques", Internal Rep. Laval Univ. Quebec, Canada.

Dieckmann, A. (1994), "FMCW-LIDAR with Tunable Twin-guide Laser Diode", *Electron. Lett.*, Vol. 30, pp. 308-309.

Dieckmann, A., M. Amann (1995), "FMCW-LIDAR with Tunable Twin-guide Laser Diode", in *Trends in Optical Fibre Metrology and Standards*, O.D.D. Soares (Ed.), pp. 791-802, Kluwer Academic Publishers, Dordrecht.

DIN (1952, 1982), "Durchflußmessung mit Blenden, Düsen und Venturirohren in voll durchströmten Rohren mit Kreisquerschnitt", DIN Blätter (in German).

Drowden, R.R. (1972), "Fluid Flow Measurement – A Bibliography", The British Hydromechanics Research Association, Cranfield Bedford, BHRA-10-1972.

Ducruet, C., A. Dyment (1984), “The Pressure Hole Problem”, *J. Fluid Mech.*, Vol. 142, pp. 251-267.

Durst, F., H. Kikura, I. Lekakis, J. Jovanoviae, Q. Ye (1996), “Wall Shear Stress Determination from Near-wall Mean Velocity Data in Turbulent Pipe and Channel Flows”, *Experiments in Fluids*, Vol. 20, pp. 417-428.

Eccardt, P-C., M. Vossiek, V. M’agori (1995), “Fuzzy Logic Applied to an Intelligent Ultrasonic Distance Sensor”, *Proc. EUFIT ’95*, Aachen, pp. 1-5.

Eckert, S. (1997), “Exp. Untersuchungen turbulenter Flüssigmetall-Gas-Strömungen in einem äußeren Magnetfeld”, PhD Thesis Technical Univ. Dresden and FZR-Report FZR-219, 1998.

Eckert, S., W. Witke, G. Gerbeth (2000), “A New Mechano-optical Technique to Measure Local Velocities in Opaque Fluids”, *Flow Measurement and Instrumentation*, Vol. 11, pp. 71-78.

Eckert, S., G. Gerbeth, F. Stefani, W. Witke (2003), “Measurement Techniques for Liquid Metal Velocity Measurements”, *Proc. 5th Int. Symp. on Liquid Metal Processing and Casting*, Nancy, France, pp. 261-271.

Eckert, S., G. Gerbeth, V.I.. Melnikov (2003), “Velocity Measurements at High Temperatures by Ultra-sound Doppler Velocimetry Using an Acoustic Wave Guide”, *Experiments in Fluids*, Vol. 35, pp. 381-388.

Eggels, J.G.M., F. Unger, M.H. Weiss, J. Westerweel, R.J. Adrian, R. Friedrich, F.T.M. Nieuwstadt (1994), “Fully Developed Turbulent Pipe Flow: A Comparison Between Direct Numerical Simulation and Experiment”, *J. Fluid Mech.*, Vol. 268, pp. 175-209.

El-Kaddah, N., J. Szekely, G. Carlsson (1984), *Met. Trans.*, Vol. 14, pp. 633-640.

El-Kaddah, N., J. Szekeli (1984), *J. Fluid Mech.*, Vol. 133, pp. 37-46.

Eringen, C.A (1980), “Mechanics of Continua”, Robert E. Krieger Publishing Comp., New York, p. 459ff.

Evans, J.W., S.D. Lympany (1983), *Met. Trans.*, Vol. 14B, pp. 306-308.

Figueroa, F., E. Barbieri (1991), *IEEE Trans. Instrum. Meas.*, Vol. 40, p. 764ff.

Foust, O.J. (1978), “Sodium-NaK Engineering Handbook, Volume 3”, Gordon & Breach Science Publishers, Inc., ISBN- 0-677-03040-1.

Franklin, R.E., J.M. Wallace (1970), “Absolute Measurements of Static Hole Error Using Flush Transducers”, *J. Fluid Mech.*, Vol. 42, pp. 33-48.

Gaetke, J. (1991), “Akkustische Strömungs- und Durchflussmessung”, Akademischer Verlag Berlin (in German).

GEC Energy Systems (1981), “Level Meter for Liquid Metals”, Cambridge Road, Leicester, LE8 3LH, United Kingdom.

Geissel, H., H. Weick, M. Winkler, G. Münzenberg, V. Chichkine, *et al*. (2003), "The Super-FRS Project at GSI", *Nuclear Instruments and Methods in Physics Research B*, Vol. 204, pp. 71-85.

Ghiglia, D.C., M.D. Pritt (1998), "Two-dimensional Phase Unwrapping, Theory, Algorithms, and Software", New York, Wiley.

Goldman, M., R. Creager, D. Parker, J. Payne (1997), "Rangefinder Metrology for the Green Bank Telescope", *Proc. EOS Topical Meeting on Optoelectronic Distance/Displacement Measurements and Applications*.

Goldstein, R.J. (1983), "Fluid Mechanics Measurement", Hemisphere Publishing, Springer Verlag, Berlin.

Goldstein, R.M., H.A. Zebker, C.L. Werner (1988), "Satellite Radar Interferometry: Two-dimensional Phase Unwrapping", *Radio Sci.*, Vol. 23, pp. 713-720.

Grevet, J.H., J. Szekely, N. El Kaddah (1982), *Int. J. Heat and Mass Transfer*, Vol. 25, pp. 487-492.

Griffith, P. (1963), "The Prediction of Low Quality Boiling Void", ASME Preprint 63-HT-20.

Grjotheim, K., C. Krohn, R. Naeumann, K. Torkler (1970), *Met. Trans.*, Vol. 1, pp. 3133-3141.

Grjotheim, K., C. Krohn, R. Naeumann, K.. Torkler (1971), *Met. Trans.*, Vol. 2, pp. 199-204.

Gueuning, F.E., M. Varlan, C.E. Eugene, P. Dupuis (1997), *IEEE Trans. Instrum. Meas.*, Vol. 46, p. 1236.

Gühring, J., C. Brenner, J. Böhm, D. Fritsch (2000), "Data Processing and Calibration of a Cross-pattern Stripe Projector", *ISPRS Congress 2000*, Amsterdam, Netherlands, Vol. 33.

Hall, I. (1956), "Displacement Effect of a Sphere in a Two-dimensional Shear Flow", *J. Fluid Mech.*, Vol. 1, pp. 142-162.

Harms, A., C.F. Forrest (1971), "Dynamic Effects in Radiation Diagnosis of Fluctuating Voids", *Nucl. Sci. Eng.*, Vol. 46, pp. 408-413.

Harms, A., A. Laratta (1973), "The Dynamic Bias in Radiation Interrogation of Two-phase Flow", *Int. J. Heat Mass Transfer*, Vol. 16, pp. 1459-1465.

Harvel, G.D., K. Horib, K.J. Kawanishib, S. Chang (1996), "Real-time Cross-sectional Averaged Void Fraction Measurements in Vertical Annulus Gas-liquid Two-phase Flow by Neutron Radiography and X-ray Tomography Techniques", *Nuclear Instruments and Methods in Physics Research*, Vol. A 371, pp. 544-552.

Hauptmann, P., N. Hoppe, A. Püttmer (2002), "Application of Ultrasonic Sensors in the Process Industry", *Meas. Sci. Technol.*, Vol. 13, pp. 73-83.

Heinemann, J.B., J.F. Marchaterre, S. Mehta (1962), "Electro-magnetic Flow Meters for Void Fraction Measurement in Two-phase Liquid Metal Flow", *Rev. Sci. Instr.*, Vol. 34 (4), pp. 399-401.

Herning, F. (1966), "Stoffströme in Rohrleitungen", VDI Verlag, Düsseldorf (in German).

Hibiki, T., K. Mishima, H. Nishihara, T. Motomura (1993), "Study on Air-water Two-phase Flow in a Small Diameter Tube", Annu. Rep. Res. Reactor Inst. Kyoto Univ., Vol. 36, pp. 34-44.

Hibiki, T., K. Mishima, K. Yoneda, S. Fujine, A. Tsuruno, M. Matsubayashi (1994b), "Visualization of Fluid Phenomena Using a High Frame-rate Neutron Radiography with a Steady Thermal Neutron Beam", *Nucl. Instrum. Methods Phys. Res.*, Vol. A351, pp. 423-436.

Hibiki, T., K. Mishima (1996), "Visualization and Measurements of Two-phase Flow in Metallic Ducts Using Neutrons as Microscopic Process" (3rd report, *Quantitative Measurement of Neutron Radiography Image*), *Trans. Jpn. Soc. Mech. Engrs. Ser. B*, Vol. 62 (595), pp. 919-926 (original paper in Japanese).

Hibiki, T., H. Hogsett, M. Ishii (1998), "Local Measurement of Interfacial Area, Interfacial Velocity and Liquid Turbulence in Two-phase Flow", *Nucl. Engng. Des.*, Vol. 184, pp. 287-304.

Hill, J.C., C.A. Sleicher (1971), "Directional Sensitivity of Hot Film Sensors in Liquid Metals", *Rev. Science Instr.*, Vol. 42, pp. 1461-1468.

Hills, J.H. (1974), "Radial Non-uniformity of Velocity and Voidage in a Bubble Column", *Trans. Inst. Chem. Engrs*, Vol. 52, p. 1ff.

Hochreiter, L.E., A. Sesonske (1969), "Thermal Turbulence Characteristics in Sodium-potassium", *Int. J. Heat and Mass Transfer*, Vol. 12, pp. 114-118.

Hofmann, B., M. Rockstroh (1996), "Study on Acoustic Waveguides and Reflectors for Use in Ultrasonic Two-phase Flow Measurement", *Ultrasonics*, Vol. 34, pp. 431-434.

Hooker, H.H., G.F. Popper (1958), ANL-5766.

Horanyi, S., L. Krebs (1988), Temperature Compensated Miniature Permanent Magnetic Flow Meter for Liquid Metal. Experimental Heat Transfer", *Proc. 1st World Conf. on Experimental Heat Transfer, Fluid Mechanics and Thermodynamics*, Dubrovnik, Yugoslavia, pp. 279-285.

Hori, M., T. Kobori, Y. Ouichi (1966), "Method for Measuring Void Fraction by Electromagnetic Flowmeters", Nippon Genshiryoku Kenkyuho (Rep.), JAERI 1111, Elsevier.

Huang, P.S., Q. Hu, F. Jin, F.P. Chiang (1999), "Color-encoded Digital Fringe Projection for High-speed Three-dimensional Surface Contouring", *Opt. Eng.*, Vol. 38 (6), pp. 1065-1071.

Huang, S.S., C.F. Huang, K.N. Huang, M.S. Young (2002), "A High Accuracy Ultrasonic Distance Measurement System Using Binary Frequency Shift-keyed Signal and Phase Detection", *Rev. Sci. Inst.*, Vol. 73 (10), pp. 3671-3677.

Huang, C.F., M.S. Young, Y.C. Li (1999), *Rev. Sci. Instrum.*, Vol. 70, p. 1452.

Hurd, C.W., K.P. Chesky, A.H. Shapiro (1953), "Influence of Viscous Effects on Impact Tubes", *J. Appl. Mech.*, Vol. 248, pp. 253-256.

Ida, M., H. Nakamura, H. Nakamura, H. Nakamura, K. Ezato, H. Takeuchi (2002), "Thermal-hydraulic Characteristics of IFMIF Liquid Lithium Target", *Fusion Engineering and Design*, Vol. 63-64, pp. 333-342.

Ida, M., H. Nakamura, K. Shimizu, T. Yamamura (2005), "Thermal and Thermal-stress Analyses of IFMIF Liquid Lithium Target Assembly", *Fusion Engng. Design*.

Imbeni, V., C. Martini, S. Masini, G. Palombarini (1999), *Properties of the Eutectic Alloys Pb55.5Bi and Pb17Li*, BoMet Institute of Metallurgy, University of Bologna, ENEA Report DT-EUB-00001, Part 2.

Ishii, M. (1975), "Thermo-fluid Dynamic Theory of Two-phase Flow", Eyerolles, France, Paris.

Ishii, M. (1977), *One-dimensional Drift-flux Model and Constitutive Equations for Relative Motion Between Phases in Various Two-phase Flow Regimes*, ANL-77-47.

Jaffray, D., J. Battista, A. Fenster, P. Munro (1994), "X-ray Scatter in Megavoltage Transmission Radiography: Physical Characteristics and Influence on Image Quality", *Med. Phys.*, Vol. 2, pp. 45-60.

Jameson, R.A., R. Ferdinand, H. Klein, J. Rathke J. Sredniawski, M. Sugimoto (2004), "IFMIF Accelerator Facility", *Journal of Nuclear Materials*, Vol. 329-333, pp. 193-197.

Jischa, M. (1982), "Konvektiver Impuls- Wärme und Stoffaustausch", Vieweg Verlag ISBN 3-528-08144-9, p. 137ff and p. 254ff (in German).

Johnson, A.R. (1978), *Light Metals*, Vol. 1, pp. 45-58.

Kalkach-Navarro, S., R.T. Lahey, Jr., D.A. Drew, R. Meyder (1993), "Interfacial Area Density, Mean Radius and Number Density Measurements in Bubbly Two-phase Flow", *Nucl. Engng. Des.*, Vol. 142, pp. 341-351.

Kapulla, R. (2000), "Experimentelle Untersuchung von thermisch stratifizierten und unstratifizierten Mischungsschichten in Natrium und Wasser", Dissertation 13430, Eidgenössische Technische Hochschule Zürich, Switzerland (in German).

Kataoka, I., M. Ishii, A. Serizawa (1986), "Local Formulation and Measurement of Interfacial Area Concentration in Two-phase Flow", *Int. J. Multiphase Flow*, Vol. 12 (4), pp. 505-529.

Kim, T.J., Z. Kojro, M. Pluta, M. Schmachtl, M. Schubert, T. Gudra, W. Grill (1999), "Confocal Scanning Acoustic Microscopy in Air at Normal Conditions at Frequencies Close to the Phonon Cut-off Regime", *Physica B*, Vol. 263-264, pp. 558-94.

Kim, S., X.Y. Fu, X. Wang, M. Ishii (2001), "Study on Interfacial Structures in Slug Flows Using a Miniaturized Four-sensor Conductivity Probe", *Nuclear Engng. Design*, Vol. 204, pp. 45-55.

Kimura, T., S. Wadaka, K. Misu, T. Nagatsuka, T. Tajime, M. Koike (1995), *IEEE Ultrasonic Symposium*, p. 737.

Kocamustafaogullari, G., Z. Wang (1991), "An Experimental Study on Local Interfacial Parameters in a Horizontal Bubbly Two-phase Flow", *Int. J. Multiphase Flow*, Vol. 17 (5), pp. 553-572.

Kollie, T.G., R.L. Anderson, J.L. Horton, M.J. Roberts (1977), "Large Thermocouple Thermometry Errors Caused by Magnetic Fields", *Rev. Science Instrum.*, Vol. 48 (5), pp. 501-511.

Knebel, J-U., L. Krebs (1994), "Calibration of a Miniature Permanent Magnetic Flow Meter Probe and its Application to Velocity Measurements in Liquid Sodium", *Experimental Thermal and Fluid Science*, Vol. 8, pp. 135-148.

Knebel, J-U., L. Krebs, U. Müller, B.P. Axcell (1998), "A Confined Sodium Jet in a Co-flow", *J. Fluid Mech.*, Vol. 368, pp. 51-80.

Knebel, J-U., *et al*. (2001), *Thermalhydraulic and Material Specific Investigations into the Realization of an Accelerator Driven System (ADS) to Transmute Minor Actinides*, Wissenschaftliche Berichte, FZKA 6618, September 2001.

Krebs, L., K. Bremhorst, (1983), "Verification of the Extended Gradient Diffusion Model by Measurement of the Mean and Fluctuating Temperature Fields in Sodium Flow Downstream of a Multi-bore Jet Block", *Proc. 4th Symp. Turbulent Shear Flows*, 17.1-17.5.1983, Karlsruhe, FR Germany.

Lefhalm, C-H. (2004), "Qualifikation von Meßtechniken in schweren Flüssigmetallströmungen", Dissertation Universität Karlsruhe (in German).

Lefhalm, C-H., N-I. Tak, H. Piecha, R. Stieglitz (2004), "Turbulent Heavy Liquid Metal Heat Transfer Along a Heated Rod in an Annular Cavity", *Journal of Nuclear Materials*, Vol. 335, pp. 280-285.

Lefhalm, C-H., M. Daubner, R. Stieglitz (2005), "Development and Assessment of Flow Rate Measurement Techniques for Lead Bismuth", *11th International Topical Meeting on Nuclear Reactor Thermal-Hydraulics (NURETH-11)*, Paper: 394, 2-6 October 2005, Popes' Palace Conference Center, Avignon, France.

Lehde, H., W. Lang (1948), *AC Electromagnetic Induction Flow Meter*, US Patent 1948, Patent No. 2.435.045.

Leopold, J., H. Günther, R. Leopold (2003), New Developments in Fast 3D-surface Quality Control. *Measurement*, 33, pp. 179-187.

Lescure, M., T. Bosch, A. Dziadowiec (1991), "An Electro-optical Frequency Doubling Method to Remove Electrical Noise in Laser Range Finder", *IEEE Trans. Instrum. Meas*., 40, pp. 1046-1047.

Li, X., G. Tao, Y. Yang (2001), "Continual Deformation Analysis with Scanning Phase Method and Time Sequence Phase Method in Temporal Speckle Pattern Interferometry", *Opt. Laser Technol*., 33, pp. 53-59.

Lighthill, M.J. (1957), "Contributions to the Theory of the Pitot Tube Displacement Effect", *J. Fluid Mech*., 1, pp. 493-512.

Ligrani, P.M., J.L. Harrison, G.I. Mahmomod, M.L. Hill (2001), "Flow Structure Due to Dimple Depressions on a Channel Surface", *Phys. Fluids*, 13, pp. 3442-3451.

Lillicrap D.C, D.J. Moore (1982), "Electromagnetic Stirring in Core Induction Furnaces", *Proc. Electroheat and Metals Conf.*, Univ. Cambridge.

Lillicrap D.C (1982), "A Technique for Velocity Measurements in Coreless Induction Furnaces", *Proc. of the Symp. Int. Union of Theoretical and Applied Mechanics*, H.K. Moffat, M.R.E. Proctor (Eds.), pp. 46-56.

Lim, H., W. Xu, X. Huang (1995), "Two New Practical Methods for Phase Unwrapping", *Proceedings 1995 International Geoscience and Remote Sensing Symposium*, Tokyo, Japan, IEEE, Piscataway, pp. 196-198.

Liu, Y., L.C. Lynnworth, M.A. Zimmermann (1998), "Buffer Waveguides for Flow Measurement in Hot Fluids", *Ultrasonics*, 36, pp. 305-315.

Livesey, H.J.L. (1956), "The Behaviour of Transverse Cylindrical and Forward Facing Total Pressure Tubes in Transverse Total Pressure Gradient", *J. Basic. Eng*., 23, pp. 949-955.

Livesey, J.L., J.D. Jackson, C.J. Southern (1962), "The Static Hole Error Problem: An Experimental Investigation of Error for Holes of Varying Diameter and Depth", *Aircr. Eng*., 34, p. 43ff.

Lykoudis, P.S., P.F. Dunn (1973), "Magneto Fluid Mechanic Heat Transfer from Hot Film Probes", *Int. Journal Heat and Mass Transfer*, 16, p. 1439ff.

Määttä, K., J. Kostamovaara, R. Myllylä (1993), "Profiling of Hot Surfaces by Pulsed Time-of-flight Laser Range Finder Techniques", *Appl. Opt*., 32 (27), pp. 5334-5347.

MacMillan, F.A. (1954), "Viscous Effects on Pitot Tubes at Low Speeds", *J. R. Aero. Soc*., 58, pp. 837-839.

MacMillan, F.A. (1956), *Experiments on Pitot Tubes in Shear Flow*, Ministry of Supply, Aero. Res. Council, R&M 3028.

Macovski, A. (1983), "Noise Considerations in Radiography and Fluoroscopy", Medical Imaging Systems, Prentice-Hall.

Maier, M., P. Sperr (1970), "On the Construction of a Fast Constant Fraction Trigger with Integrated Circuits and Application to Various Phototubes", *Nucl. Instrum. Methods*, 87, pp.13-18.

Malcolm, D.J. (1969), *J. Fluid Mech*, 37, pp. 701-714.

Malcolm, D.G., V. Verma (1981), "Dynamic Response of Forced Convective Heat Transfer from Hot-film Sensors to Mercury. Part 2: Experiment", *J. Fluid Mech*., 112, pp. 475-485.

McKeon, B.J., A.J. Smits (2002), "Static Pressure Correction in High Reynolds Number Fully Developed Pipe Flow", *Meas. Sci. Techn*., 13, pp. 1608-1614.

McKeon, B.J., J. Li, W. Jiang, J.F. Morrison, A.J. Smits (2003), "Pitot Probe Correction in Fully Developed Turbulent Pipe Flow", *Meas. Science and Instrumentation*, 14, pp. 1449-1458.

Marioli, D. (1992), *IEEE Trans. Instrum. Meas*., 41, p. 93ff.

Mishima, K., T. Hibiki, Y. Saito, H. Nishihara, Y. Tobita, K. Konishi, M. Matsubayashi (1999), "Visualization and Measurement of Gas-liquid Metal Two-phase Flow with Large Density Difference Using Thermal Neutrons as Microscopic Probes", *Nuc. Instr. Meth. in Phys. Res*., A 424, pp. 229-234.

Matsubayashi, M., *et al*. (2001), *Nucl. Instr. and Meth*., A 463, p. 324 ff.

Matsubayashi, M., *et al*. (2003), *Nucl. Instr. and Meth*., A 510, p. 325ff.

Matsubayashi, M., T. Hibiki, K. Mishima, K. Yoshii, K. Okamoto (2004), "An Improved Fast Neutron Radiography Quantitative Measurement Method", *Nuclear Instruments and Methods in Physics Research A*, 533, pp. 481-490.

Mishima, K., S. Fujine, K. Yoneda, K. Yonebayashi, K. Kanda, H. Nishihara (1992), in *A Study of Air-water Flow in a Narrow Rectangular Duct Using an Image Processing Technique, Dynamics of Two-phase Flow*, O.C. Jones, I. Michiyoshi (Eds.), CRC Press, Boca Raton, FL, pp. 141-160.

Mishima, K., T. Hibiki, H. Nishihara (1993), "Some Characteristics of Gas-liquid Flow in Narrow Rectangular Ducts", *Int. J. Multiphase Flow*, 19, pp. 115-124.

Mishima, K., T. Hibiki, H. Nishihara (1997), "Visualization and Measurement of Two-phase Flow by Using Neutron Radiography", *Nuclear Engineering and Design*, 175, pp. 25-35.

ISO 3966-1977, *Measurement of Fluid Flow in Closed Conduits – Velocity Area Method Using Pitot Static Tubes*, Edition 1999.

Moore, D.J. (1982), "Magnetohydrodynamics of the Coreless Induction Furnace", PhD dissertation, University of Cambridge.

Moore, D.J., J.C.R. Hunt (1983), *Prog. in Astronautics and Aeronautics*, 83, pp. 359-373.

Moros, A., J.C.R. Hunt, D.C. Lillicrap (1985), *Prog. in Astronautics and Aeronautics*, 100, pp. 706-705.

Müller, R., H. Wölfelschneider, M. Kublin, H. Anderer (1997), "Application Limits of Optical Distance Measuring Based on the Phase Detection Technique", *Proc. EOS Topical Meeting on Optoelectronic Distance/Displacement Measurements and Applications*.

Müller, U., R. Stieglitz, S. Horanyi (2005), "Complementary Experiments at the Karlsruhe Dynamo Test Facility", forthcoming in *J. Fluid Mechanics*.

Munshi, P., M.S. Vaidya (1993), "A Sensitivity Study of Poisson's Corruption in Tomographic Measurements for Air-water Flows", *Trans. American Nuclear Society*, 68, pp.234-236.

Murakami, M., M. Maruo, T. Yoshiki (1990), "Development of an Electromagnetic Flowmeter for Studying Gas-liquid Two-phase Flow", *International Chemical Engineering*, 30 (4), pp. 699-702.

Murthy, A., J. Szekeli (1983), *Met. Trans.*, 14B, pp. 499-502.

Nakamura, H., M. Kondo, Y. Kukita (1998), "Simultaneous Measurement of Liquid Velocity and Interface Profiles of Horizontal Duct Wavy Flow by Ultrasonic Velocity Profile Meter", *Nuclear Engineering and Design*,184, pp. 339-348.

Natec Schultheiß GmbH (1999), *FT Series Turbine Flowmeter – Installation, Operation and Maintenance Manual*, Flow Technology, Inc., Phoenix, Arizona.

Neal, L.G., S.G. Bankoff (1963), "A High Resolution Resistivity Probe for Determination of Local Void Properties in Gas-liquid Flow", *AIChE J.*, 9 (4), pp. 490-494.

Nowak, M. (2002), "Wall Shear Stress Measurement in a Turbulent Pipe Flow Using Ultrasound Doppler Velocimetry", *Experiments in Fluids*, 33, pp. 249-255.

Ochiai, M., T. Kuroyanagi, K. Kobayashi, K. Furukawa (1971), "Void Fraction and Heat Transfer Coefficient of Sodium-argon Two-phase Flow in Vertical Channel", *J. Atomic Energy Society of Japan*, 13, pp. 566-573.

Ogino, F., M. Kamata, K. Mishima, S. Fujine, K. Yoneda, K. Kanda (1994), "Application of Neutron Radiography to the Study of Liquid-solid Two-phase Flow", *Exp. Therm. Fluid Sci*., 12, p. 339ff.

Oyedele, J., T. Akintola (1991), "Void Fluctuation Effects in Radiation Interrogation of Voided Liquids", *Applied Radiation and Isotopes*, 42, pp. 341-346.

Ozarapoglu, V. (1972), PhD Thesis Laval Univ., Quebec, Canada.

Panametrics (1998), *Handbuch Ultraschalldurchflußmessgerät XMT868 mit IDM-Software*, Version 10/98 (in German).

Parrilla, M., J.J. Anaya, C. Fritsch (1991), *IEEE Trans. Instrum. Meas*., 40, p. 759ff.

Payne, J., D. Parker, R. Bradley (1992), "Rangefinder with Fast Multiple Range Capability", *Rev. Sci. Instrum*., 63 (6), pp. 3311-3316.

Patel, V.C. (1965), "Calibration of the Preston Tube and Limitations on its Use in Pressure Gradients", *J. Fluid Mech*., 23, pp. 185-208.

Patorski, A., G.S. Bauer, I. Platnieks, Y. Takeda (2000), *Experimental Estimation of Optimum Bypass-jet-flow Conditions for the Cooling of the Window of the SINQ Liquid Metal Target*, PSI Report, ISSN 1423-7350, Vol. VI, pp. 42-44, PSI, CH-5232 Villigen, Switzerland.

Patorski, J., G.S. Bauer, S. Dementjev (2001), "Two-dimensional and Dynamic Method of Visualization of the Flow Characteristics in a Convection Boundary Layer Using Infrared Thermography", *Journal of Theoretical and Applied Mechanics* (ISSN 1429-2955), Vol. 39, 2.

Pawlowski, M.E., M. Kujawinska, M.G. Wegiel (2002), "Shape and Motion Measurement of Time-varying Three-dimensional Objects Based on Spatiotemporal Fringe-pattern Analysis", *Opt. Eng*., 41 (2), pp. 450-459.

Perchet, G., M. Lescure, Th. Bosch (1997), "Errors Analysis of Phase Shift Laser Range Finder with High Level Signal", *Sens. Actuators A*, 62 (1-3), pp. 534-538.

Perry, A.E., S. Hafez, M.S. Chong (2001), "A Possible Reinterpretation of the Princeton Superpipe Data", *J. Fluid Mech*., 439, pp. 395-401.

Petrick, M., B.S. Swanson (1958), *Rev. Sci. Instr*., 29, p. 1079ff.

Petrick, M., K.Y. Lee (1964), *Performance Characteristics of a Liquid Metal Generator*, Argonne National Lab., ANL-6870.

Platnieks, I. (1971), *Magnetohydrodynamics*, 7, pp. 140-142.

Platnieks, I., G. Ulmann (1984), "Hot Wire Sensor for Liquid Sodium", *J. Phys. E., Sci. Intrum*., 17, pp. 862-863.

Platnieks, I., G. Bauer, O. Lielausis, Y. Takeda (1998), "Measurements of Heat Transfer at the Beam Window in a Mockup Target for SINQ Using Mercury", *14th Meeting of the Intern. Collaboration on Adv. Neutron Sources*, Starved Rock Lodge, Utica, Ill., USA, 14-19 June.

Platnieks, I. (2000), "Heat Transfer Experiments Using HETSS", *4th MEGAPIE Co-ordination Meeting (WP X4/5/6)*, 5 Oct. 2000, ENEA Centro di Ricerche Brasimone, Italy.

Powell, R.L., W.I. Hall, C.H. Hyink, L.L. Sparks, G.W. Burns, M.G. Scroger, H.H. Plumb (1974) *Thermocouple Reference Tables*, IPTS-68, US Department of Commerce.

Pozrikidis, C. (1994), "Shear Flow over a Plane Wall with an Axis-symmetric Cavity or a Circular Orifice of Finite Thickness", *Phys. Fluids*, 6, pp .68-79.

Quan, C., X.Y. He, C.J. Tay, H.M. Shang (2001), "3D Surface Profile Measurement Using LCD Fringe Projection", *Proc SPIE 2001*,4317, pp. 511-516.

Quiroga, J.A., A. Gonzalez-Cano, E. Bernabeu (1995), "Phase Unwrapping Algorithm Based on an Adaptive Criterion", *Appl. Opt*., 34, pp. 2560-2563.

Räisänen-Ruotsalainen, E., T. Rahkonen, J. Kostamovaara (1998), "Integrated Time-to-digital Converters Based on Interpolation", *J. Analog Integr. Circ. Signal Process*, 15 (1), pp. 49-57.

Ray, A.K. (1956), "On the Effect of Orifice Size on Static Pressure Reading at Different Reynolds Numbers", *Img.-Arch*., 24, p. 3ff.

Rayle, R.J., Jr. (1959), "An Investigation of the Influence of Orifice Geometry on Static Pressure Measurements", MS thesis, Massachusetts Institute for Technology (MIT-1959).

Reed, C.B., B.F. Picologlou (1986), "Techniques for Measurements of Velocity in Liquid Metal MHD-Flows", *7th Top. Meeting on Fusion Technology*, Nevada.

Reed, C.B., B.F. Picologlou, J.S. Walker (1987), *ALEX Results – A Comparison of Measurements from a Round and a Rectangular Duct with 3D-code Predictions*, IEEE No. 87CH2507-2, Vol. 2, 1267-1270.

Reed, C.B., B.F. Picologlou (1989), "Side Wall Flow Instabilities in a Liquid Metal MHD-flow Under Blanket Relevant Conditions", *Fusion Technology*, 15, 705-715.

Reichardt, V.H. (1951), "Vollständige Darstellung der turbulenten Geschwindigkeitsverteilung in glatten Leitungen", *Zeitschrift für Angewandte Mathematik und Mechanik,* 31 (7) (in German).

Richards W.J., M.R. Gibbons, K.C. Shields (2004), "Neutron Tomography Developments and Applications", *Applied Radiation and Isotopes*, 61, pp. 551-559.

Ricoud, R., Ch. Vives, "Local Velocity and Mass Transfer Measurements in Molten Metals Using an Incorporated Magnet Probe", *Int. J. Heat and Mass Transfer*, 25 (10), pp. 1579-1588.

Rioux, M., G. Bechthold, D. Taylor, M. Duggan (1987), "Design of a Large Depth of View Three-dimensional Camera for Robot Vision", *Opt. Eng*., 26 (12), pp. 1245-1250.

Rioux, M., F. Blais, J-A. Beraldin, P. Boulanger (1989), "Range Imaging Sensors Development at NRC Laboratories", *Proc. IEEE Workshop on Interpretation of 3D Scenes*, Austin, TX, pp. 154-160.

Rohrbacher, H.A., R. Bartholomay (1975), *Ultraschallmesstechnik in Natrium-Systemen*, Gesellschaft für Kernforschung mbH, KFK 2116, Karlsruhe (in German).

Ruotsalainen, T., P. Palojärvi, J. Kostamovaara (1999), "A Current-mode Gain-control Scheme with Constant Bandwidth and Propagation Delay for Transimpedance Preamplifier", *IEEE J. Solid State Circuits*, 34 (2), pp. 253-258.

Saito, Y., K. Mishima, Y. Tobita, T. Suzuki, M. Matsubayashi (2004), "Velocity Field Measurement in Gas-liquid Metal Two-phase Flow with Use of PIV and Neutron Radiography Techniques", *Applied Radiation and Isotopes*, 61, pp. 683-691.

Saito, Y., K. Mishima, Y. Tobita, T. Suzuki, M. Matsubayashi, I.C. Lim, J.E. Cha (2005), "Application of High Frame-rate Neutron Radiography to Liquid-metal Two-phase Flow Research", *Nuclear Instruments and Methods in Physics Research A*, 542, pp. 168-174.

Sanaullah, K., S.H. Zaidi, J.H. Hills (2001), "A Study of Bubbly Flow Using Resistivity Probes in a Novel Configuration", *Chemical Engineering Journal*, 83, pp. 45-53.

Satyamurthy, P., T.K. Thiyagarajan, N. Venkatramani (1994), "Void Fraction Profile Measurement in Two-phase Liquid Metal Flows Correction for Finite Beam Size of the Gamma-rays", *2nd International Conference on Energy Transfer in Magnetohydrodynamic Flows*, France.

Satyamurthy, P., N.S. Dixit, T.K. Thiyagarajan, N. Venkatramani, A.M. Quraishi, A. Mushtaqb (1998), "Two-fluid Model Studies for High Density Two-phase Liquid Metal Vertical Flows", *Int. J. Multiphase Flows*, 24, pp. 721-737.

Schlichting, H. (1979), "Boundary Layer Theory", 7th edition, MacGraw-Hill.

Scholze, H. (1965), Glas-Natur, Struktur und Eigenschaft, F. Viehweg Verlag (in German).

Shoenwald, J.S., C.V. Smith, Jr. (1984), *Proc. of the IEEE Ultrasonic Symposium*, p. 469ff.

Serizawa, A., I. Kataoka, I. Michiyoshi (1975), "Turbulence Structure of Air-water Bubbly Flow. Part 1. Measuring Techniques", *Int. J. Multiphase Flow*, 2, pp. 221-223.

Seta, K., T. Ohishi (1987), "Distance Measurement Using a Pulse Train Emitted from a Laser Diode", *Jpn. J. Appl. Phys.*, Part 2 (26), pp. 1690-1692.

Shaw, R. (1960), "The Influence of Hole Dimensions on Static Pressure Measurements", *J. Fluid Mech.*, 7, pp. 550-564.

Shen, X., Y. Saito, K. Mishima, H. Nakamura (2005), "Methodological Improvement of an Intrusive Four-sensor Probe for the Multi-dimensional Two-phase Flow Measurement", *International Journal of Multiphase Flow*, 31, pp. 593-617.

Shercliff, J.A. (1962), "The Theory of Electromagnetic Flow Measurement", Cambridge University Press.

Shercliff, J.A. (1987), "The Theory of Electro-magnetic Flow Measurement – Induction Devices", Cambridge University Press ISBN 0521 335 54X.

Siemens (1969), "Formel und Tabellenhandbuch für Starkstromingenieure", 4th edition (in German).

Simoni, A., L. Gonzo, M. Gottardi (2002), "Integrated Optical Sensors for 3-D Vision", *Trans. IEEE*, 78, pp. 745-748.

Sleicher, C.A., G.B. Lim (1975), "Dynamic Behaviour of Hot Film Anemometers in Liquid Metals", *Proc. Symp. on Turbulence in Liquids*, Univ. Missouri-Rolla, pp. 563-570.

Slotwinski, A., F. Goodwin, D. Simonson (1989), "Utilizing AlGaAs Laser Diodes as a Source for Frequency Modulated Continuous Wave (FMCW) Coherent Laser Radars", *Proc. SPIE*, 1043, pp. 245-251.

Stieglitz, R., U. Müller (1996), *Der Geodynamo, eine Versuchsanlage zum Nachweis des homogenen Dynamoeffektes*, FZKA5716 (in German).

Suzuki Y., M. Aritomi H. Kikura (2000), "Measurement of the Flow Around Bubbles Using the Ultrasonic Velocity Profile Monitor", *Bull. Res. Lab. Nucl. Reactors* (Tokyo Inst. Technol.), 3, pp. 93-99.

Strand, J., T. Taxt (1999), "Performance Evaluation of Two-dimensional Phase Unwrapping Algorithms", *Appl. Opt*., 38, pp. 4333-4343.

Suzuki, Y., M. Nakagawa, M. Aritomi, H. Murakawa, H. Kikura, M. Mori (2002), "Microstructure of the Flow Field Around a Bubble in Counter-current Bubbly Flow", *Experimental Thermal and Fluid Science*, 26, pp. 221-227.

Strzelecki, E., D. Cohen, L. Coldren (1988), "Investigation of Tunable Single Frequency Diode Lasers for Sensor Applications", *J. Lightwave Technol*., LT-6, pp. 1610-1680.

Swindell, W., E. Morton, P. Evans, D. Lewis (1991), "The Design of Megavoltage Projection Imaging Systems: Some Theoretical Aspects", *Med. Phys*., 18, pp. 855-866.

Szekely, J. (1964), *ISI Journal*, 202, pp. 505-508.

Szekely, J., C.W. Chang, R.E. Ryan (1977), *Met. Trans. 8B*, pp. 333-338.

Szekely, J., C.W. Chang (1977a), *Ironmaking and Steelmaking*, 3, pp. 196-204.

Szekely, J., C.W. Chang (1977b), *Ironmaking and Steelmaking*, 3, pp. 190-195.

Szekely, J, J.H. Grevet, N. El-Kaddah (1984), *Int. J. Heat and Mass Transfer*, 27, pp. 1116-1121.

Szekeli, J., J.W. Evans, J.K. Brimacombe (1988), "The Mathematical and Physical Modelling of Primary Metals Processing Operation", John Wiley& Sons, pp. 117-120.

Taberaux, A.T., R.B. Hester (1984), *Light Metals*, 11, pp. 519-539.

Takeda, Y., W.E. Fischer, J. Sakakibara (1994), "Decomposition of the Modulated Waves in a Rotating Couette System", *Science*, 263, pp. 502-505.

Takeda, Y. (1995), "Velocity Profile Measurement by Ultrasonic Doppler Method", *Exp. Therm. Fluid Sci*., 10, pp. 444-453.

Takeda, Y., H. Kikura (1997), *Measurement of Liquid Metal Flow in a SINQ Target Geometry*, in PSI Annual Report, Annex IIIA, pp. 20-21.

Takenada, N., T. Fujii, A. Ono, K. Sonada, S. Tazawa, N. Nakanii (1994), *Nondestr. Test. Eval*., 11, pp. 107ff.

Takenaka, N., T. Fujii, A. Ono, K. Sonoda, S. Tazawa, T. Nakanii (1994), "Visualization of Streak Lines in Liquid Metal by Neutron Radiography", *Exp. Therm. Fluid Sci*., 12, p. 355.

Takenada, N., H. Asonao, T. Fujii, Y. Motomura, A. Ono, M. Matsubayashi, A. Tsuruno (1996), "Liquid Metal Flow Measurement by Neutron Tomography", Nuc. *Inst. And Methods in Phys. Res*., A377, pp. 156-160.

Tardajos, G., G.G. Gaitano, F.R.M. de Espinosa (1994), *Rev. Sci. Instrum*., 65, p. 2933ff.

Tavoularis, S., M. Szymczak (1989), "Displacement Effects of Square Ended Pitot Tubes in Shear Flows", *Exp. Fluids*, 7, pp. 33-37.

Tay, C.J., C. Quan, H.M. Shang, T. Wu, S.H. Wang (2003), "New Method for Measuring Dynamic Response of Small Components by Fringe Projection", *Opt. Eng*., 42 (6), pp. 1715-1720.

Tay, C.J., C. Quan, Y. Fu, L.J. Chen, H.M. Shang (2004), "Surface Profile Measurement of Low-frequency Vibrating Objects Using Temporal Analysis of Fringe Pattern", *Optics & Laser Technology*, 36, pp. 471-476.

Theofanus T., W. Yuen, S. Angelini, X. Chen, W. Amarasooriya, S. Medhekar (1994), *Steam Explosions: Fundamentals and Energetic Behaviour*, NUREG/CR-5960.

Thiyagarajan, T.K., N.S. Dixit, P. Satyamurthy, N. Venkatramani, V.K. Rohatgi (1991), "Gamma-ray Attenuation Method for Void Fraction Measurement in Fluctuating Two-phase Liquid Metal Flows", *Measurement Science and Technology*, 2, pp. 69-74.

Thom, A., C.J. Appelt (1957), "The Pressure in a Two-dimensional Static Hole at Low Reynolds Numbers", *Aero. Res. Counc. R&M 3090*.

Toh, S.L., C. Quan, K.C. Woo, C.J. Tay, H.M. Shang (2001), "Whole Field Surface Roughness Measurement by Laser Speckle Correlation Technique", *Optics Laser Technology*, 33, pp. 427-434.

Tsubayashi, M., M. Sobajima, S. Ohtomo (1994a), *Proceedings 4th World Conference Neutron Radiography*, San Francisco, CA, 10-16 May, Neutron Radiography, 4th ed., J.P. Barton Gordon and Breach, Yverdon, Switzerland, p. 317ff.

VDI-Wissensforum (2001), "Durchfluss und Mengenmessungen in Rohrleitungen", VDI-Seminar 361624, Universität Stuttgart (in German).

von der Hardt, P., H. Röttger (Eds.) (1981), "Neutron Radiography Handbook", D. Reidel (Ed.), Dordrecht, Holland.

Velt, I.D., V.I. Petrushaitis, B.S. Sprjgin, I.V. Krasilnikov, Yu.V. Mikhailov, V.R. Tuleninov (1982), *Correlation Technique for Flow Rate Measurement of Electro-conductive Fluids and Two-phase Media and a Device for its Implementation*, Int. Patent No. 30.01.82.

Webster, D. (1994), *IEEE Trans. Instrum. Meas*., 43, p. 578.

Weissenfluh, Th. (1985), "Probes for Local Velocity and Temperature Measurements in Liquid Metal Flow", *Int. J. Heat and Mass Transfer*, 28 (8), pp. 1563-1574.

Weissenfluh, Th., B. Sigg (1988), "Experience with Permanent Magnetic Probes for the Measurement of Local Velocities in Liquid Metals", *Prog. in Astronautics and Aeronautics*, 111, pp. 61-81.

White, F.M. (1986), *Fluid Mechanics*, 2nd edition, McGraw-Hill, New York.

Wu, Q., M. Ishii (1999), "Sensitivity Study on Double-sensor Conductivity Probe for the Measurement of Interfacial Area Concentration in Bubbly Flow", *Int. J. Multiphase Flow*, 25 (1), pp. 155-173.

Wunderlich, Th., P.O. Brunn (2000), "A Wall Layer Correction for Ultrasound Measurement in Tube Flow: Comparison Between Theory and Experiment", *Flow Measurement and Instrumentation*, 11, pp. 63-69.

Xu, L., Han, Y., X, L.A., J. Yang (1997), "Application of Ultra-sonic Tomography to Monitoring of Two-phase Flow, *Chem. Engng. Science*, 52 (13), pp. 2171-2183.

Yang, M., S.L. Hill, J.O. Gray (1994), *IEEE Trans. Instrum. Meas*., 43, p. 861ff.

Young, M.S., Y.C. Li (1992), *Rev. Sci. Instrum*., 63, p. 5435ff.

Zagarola, M.V. (1996), "Mean Flow Scaling in Turbulent Pipe Flow", PhD thesis, Princeton University.

Zagarola, M.V., A.J. Smits (1998), "Mean Flow Scaling of Turbulent Pipe Flow", *J. Fluid Mech*., 373, pp. 33-79.

Zhilin, V.G., K.V. Zvyagin, Y.P. Ivochkin (1987), *Dynamic Response and Spectral Resolution in Fibre-optics Liquid Metal Velocity Sensors*, Plenum publishing paper 0018-151X/86/2405-0729, p. 729-736.

Zhilin, V.G., K.V. Zvyagin, Y.P. Ivochkin, A.A. Oksmann (1989), "Liquid Metal Magnetohydrodynamics, Diagnostics of Liquid Metal Flows Using Fibre-optic Velocity Sensor", J. Lielpetris, R. Moreau (Eds.), Kluwer Academic Publishers, pp. 373-379.

Zhmylev, A., L. Lisitsinskii, A. Topunov (2003), "Testing the New VZLET UR Ultrasonic Level Meter", *Measurement Techniques*, 46 (2), pp. 212-215.